I. EXPERIMENTAL OBSERVATIONS OF THE MICROLAYER IN VAPOR BUBBLE GROWTH ON A HEATED SOLID

II. AN INVESTIGATION OF THE THEORY OF EVAPORATION AND CONDENSATION

Thesis by

Larry Douglas Koffman

In Partial Fulfillment of the Requirements

for the Degree of

Doctor of Philosophy

California Institute of Technology

Pasadena, California

1980

(Submitted September 27, 1979)

ACKNOWLEDGMENTS

My years at Caltech have been very enjoyable and rewarding, and I thank Professor Milton Plesset for bringing me to Caltech and for sharing with me some of his vast knowledge of science and engineering. Professor Plesset's guidance and encouragement have been deeply appreciated throughout my stay. I sincerely thank Professor Theodore Wu for the many ways in which he has helped me; his knowledge and enthusiasm have been a constant delight to witness. Professor Lester Lees has very kindly given much of his time to discuss the investigation of the theory of evaporation and condensation; his guidance and advice are greatly appreciated. Professors Rolf Sabersky and Christopher Brennen have offered encouragement and many valuable suggestions during the course of this work. A special thanks is extended to Professor W. Fiszdon for several interesting discussions and also for supplying a manuscript of his forthcoming publication. The success of the experimental investigation is largely due to the discussions with and suggestions of Dr. George Yates.

The completion of this thesis has been greatly expedited by the skill and experience of Miss Helen Burrus in typing the manuscript. I especially thank Helen for kindly working on several nights and on the weekend so that I could meet a deadline. The fine graphics work on the figures is due to Miss Cecilia Lin.

The support of the National Science Foundation and of the California Institute of Technology is gratefully acknowledged.

Finally, I cannot imagine that I could have completed this work without the encouragement, patience, and love of my wife Lee.

ABSTRACT

Two fundamental problems related to the evaporation of the microlayer formed beneath growing vapor bubbles on a solid surface are investigated. First, experimental measurements of microlayer formation and evaporation have been obtained for nucleate boiling of water and ethanol using laser interferometry combined with high speed photography. For pool boiling of water at atmospheric pressure with low subcooling, the initial microlayer profile is wedge-like with a thickness of 1.85 μm at a radius of 0.25 mm; the thickness for ethanol is approximately 1.6 times that for water. The measured evaporation rates from the microlayer correspond to local heat fluxes of the order of 1000 kW/m^2 over the bubble lifetime. The measurement technique of laser interferometry is discussed in detail with emphasis on the difficulties encountered in interpretation of the fringe patterns. In the second investigation, the theory of evaporation and condensation is considered from a kinetic theory approach. The moment method of Lees is used to solve the problem of the flow of vapor between a hot liquid surface and a cold liquid surface. A result of the theory is that the temperature profile in the vapor for the continuum problem is inverted from what would seem physically reasonable. Because of this behavior, the theory is questioned on physical grounds leading to the conclusion that the usually assumed boundary conditions for emission of molecules from a liquid surface are probably incorrect.

TABLE OF CONTENTS

PART PAGE

I EXPERIMENTAL OBSERVATIONS OF THE MICROLAYER IN VAPOR BUBBLE GROWTH ON A HEATED SOLID

LIST OF FIGURES

PART I

LIST OF FIGURES (cont'd)

PART I

LIST OF FIGURES (cont'd)

PART I Page

Figure

PART II

PART I

EXPERIMENTAL OBSERVATIONS OF THE MICROLAYER IN VAPOR BUBBLE GROWTH ON A HEATED SOLID

LIST OF SYMBOLS

C = constant of proportionality in equation (5.3)

d = distance between two interfaces

E = electric field of a plane wave

h = height of spherical surface above a plane

I = intensity

J = net mass flux

k = wavenumber $= 2\pi/\lambda$

m = fringe order number

n = index of refraction

p^e = equilibrium vapor pressure

p_i = internal pressure of vapor bubble

p_∞ = pressure in liquid far away

R = radius of bubble

T_b = temperature of microlayer surface

t = time

t_g = time for growth of bubble base to a specific radius

u = radial velocity

x = radial distance

z = coordinate normal to surface

δ = microlayer thickness

λ = wavelength of light

ν = kinematic viscosity

σ = surface tension

ω = frequency of light

I. INTRODUCTION

When boiling of a liquid in contact with a solid surface occurs a dramatic increase in the heat transfer rate at the solid surface is observed. The immediate question which comes to mind is why does the presence of vapor bubbles at the solid surface affect the heat transfer rate so strongly. To understand the mechanism by which the heat transfer rate is increased by nucleate boiling is a fundamental problem. In addition, the engineering applications of nucleate boiling heat transfer are of great practical importance. For example, current problems in nuclear reactor safety analysis require the consideration of nucleate boiling heat transfer. For such engineering problems, we would like to be able to predict the heat transfer rates for nucleate boiling occurring under different conditions. Presumably, understanding of the mechanism of heat transfer in nucleate boiling will further our ability to predict heat transfer rates for systems with different boiling conditions.

Research in nucleate boiling has followed two lines of approach. In the single bubble approach, a single vapor bubble at a solid surface is studied. The goal of this approach is to understand the mechanism of heat transfer due to a single bubble. The overall heat transfer is presumed to be due to the cumulative effect of all the single bubbles in addition to the convective heat transfer over the part of the surface where bubbles do not occur. The other approach, which has been used successfully in convective heat transfer, is to attempt to correlate experimental heat transfer measurements with the physical parameters of the system. Due to the large number of physical parameters of importance in boiling, this latter approach has not been as successful in boiling heat transfer as in convective heat transfer. Future success of this approach would appear to rely on a better understanding of the fundamental mechanism of heat transfer in nucleate boiling. The present investigation follows the elementary single bubble approach in an attempt to improve our understanding of the fundamental mechanism of heat transfer in nucleate boiling.

When a liquid cools a heated solid surface by convection the heat transfer rate is limited by the presence of a thermal boundary layer in the liquid at the solid surface. Boiling in some way overcomes this thermal resistance. Two mechanisms have been proposed to explain how a single vapor bubble can increase the heat transfer rate at the solid surface. The mechanism first proposed is that the bubble simply disrupts the thermal boundary layer [14]. The bubble is thought to act as a small "pump" which pushes hot liquid away from the surface during growth allowing cooler liquid to return to the surface during bubble collapse or during bubble lift off. In this manner, additional mixing of the liquid is achieved near the surface to yield a turbulence-like convective effect. This mechanism has been called microconvection, bubble agitation, and vapor-liquid displacement; in the present investigation, the term microconvection is used. In the early boiling research from 1940-1960, microconvection was thought to be the dominant mechanism of heat transfer in nucleate boiling. However, microconvection alone did not seem to be an entirely satisfactory explanation for the high heat transfer rates. In the late 1950's, another mechanism was proposed to explain the observed high heat transfer rates in nucleate boiling. Snyder and Edwards [27] postulated that when a vapor bubble grows on a solid surface, a thin liquid viscous layer must be formed beneath the bubble in order to satisfy the no slip boundary condition at the solid surface. This thin liquid layer, called the microlayer, is supposed to be superheated since it is in direct contact with the hot solid surface. Furthermore, the top of the bubble quickly grows beyond the thermal layer into the cool liquid. Net evaporation can then occur at the microlayer surface with net condensation occurring at the top of the bubble. Using Plesset's [22] theory to describe the flow of vapor between liquid surfaces at different temperatures, Snyder and Edwards estimated that an extremely large energy flux at the solid surface could result in order to satisfy the latent heat of vaporization requirement necessary for evaporation from the microlayer. This mechanism of heat transfer in nucleate boiling is called latent heat transport or microlayer evaporation.

The postulated existence of the microlayer and the proposed latent heat transport mechanism stimulated a strong research effort to explore these possibilities. Experimental research has verified the existence of the microlayer. A few experimental estimates of the microlayer thickness have been obtained although some discrepancies exist for the important case of water. Recently, Plesset and Prosperetti [23] have analyzed the role of microlayer evaporation in the heat transfer process. They have found that the analytical results are very sensitive to the unknown microlayer thickness. Analytical efforts to solve the problem of microlayer formation have been generally unsuccessful. Hence, further progress in evaluating the latent heat transport mechanism requires experimental measurement of the microlayer thickness. In particular, experimental results for water are desirable. The goal of the present experimental investigation has been to develop a technique to measure the microlayer thickness, especially for water.

The microlayer thickness can be estimated to be of the order of micrometers for typical bubbles which grow to a size of approximately 1mm with lifetimes of a few milliseconds. For measurement of such thicknesses, two techniques have been used. The first technique uses a high response thermocouple at the solid surface to measure the time history of the surface temperature as the microlayer grows across the thermocouple. The microlayer thickness can then be estimated from a heat balance by assuming that all of the energy goes into the latent heat of vaporization to evaporate the microlayer. This technique does not give a direct measurement and can only give an order of magnitude estimate of microlayer thickness. Also, it is difficult to obtain measurements at more than one point so that detail of the microlayer profile is not available. A more promising technique is the use of interferometry in which there is the potential to obtain detailed microlayer profiles. The reflections of collimated, coherent, monochromatic light from the bounding surfaces of the microlayer (the upper liquid-vapor interface and the lower liquid-solid interface) interfere to give fringe patterns which can be recorded on film. These fringe patterns can be interpreted as the thickness changes over the microlayer profile. The major difficulty with this technique is the interpretation of the fringe patterns. Because of the detail potentially available, we have chosen to use interferometry to measure the microlayer thickness.

In the present experimental investigation, an interferometric system capable of measuring microlayer thickness for water vapor bubbles has been developed. The system includes a laser which serves as a collimated, coherent, monochromatic light source, a microscope optical system to magnify the vapor bubbles, and a high speed movie camera to record the fringe patterns on film. Using this system, we have obtained microlayer fringe patterns for ethanol and water boiling on a glass plate at atmospheric pressure with low subcooling of the bulk fluid. The major effort of the present investigation has been the interpretation of these fringe patterns so as to give microlayer thicknesses. Discussion of the problems involved in such interpretation of the microlayer fringe patterns is lacking in the literature. We have here clarified these difficulties and have sought to resolve them. The problems considered are fringe contrast and optical background noise, spurious interference patterns such as from the top of the bubble, spatial resolution of the fringes, and the need of a zero reference for determination of the correct fringe order. For the interferometric system reported here, these problems have been satisfactorily resolved.

The results of the experimental measurements are given by graphs of the time histories of the microlayer profiles. The initial microlayer profile for water is wedge-like with a thickness of 1.85 μm at a radius of 0.25 mm; the thickness for ethanol is approximately 1.6 times that for water. The evaporation rates of the microlayer obtained from the time histories require heat fluxes of the order of 1000 kW/m^2

for both water and ethanol. From the measured microlayer thickness for water, it can be inferred that in the case of highly subcooled nucleate boiling, microconvection is the dominant heat transfer mechanism. For low subcoolings, the microlayer evaporation may contribute more significantly to the overall heat flux.

II. HISTORICAL REVIEW

In this chapter, a brief historical review is presented of the experimental efforts to detect and measure the microlayer. No attempt is made to review the numerous analytical investigations which in some way involve microlayer evaporation. However, the recent analytical model of Plesset and Prosperetti [23] is briefly reviewed since that work and the present experimental investigation are complementary.

2.1 Measurements of the microlayer with thermocouples

The first experimental detection of the microlayer is usually credited to Moore and Mesler [20]. In their experiments, boiling of saturated water at atmospheric pressure was obtained with heat fluxes of 426-638 kW/m^2. Measurements of surface temperature were obtained with a flush-mounted thermocouple of 0.127 mm diameter designed to have a 1 μsec response time. They observed periodic temperature drops of 20° - 30°F occurring over a 2 msec interval. A typical temperature drop is characterized by a sharp drop followed a short time later by a sharp cut off, and then a slow recovery to a higher temperature. They argued that the sharp drop could only be explained by microlayer evaporation. The sharp cut off is assumed to result after complete evaporation of the microlayer ("dryout"). An estimate of the order of magnitude of the microlayer thickness can be obtained from a heat balance assuming that dryout has occurred; Moore and Mesler estimated a microlayer thickness of 2 μm for water boiling at the above conditions. Mesler has obtained further measurements of this kind and has found similar results [7, 13, 19, 25]. Also, Hospeti and Mesler [12] have measured the amount of radioactive calcium sulfate scale deposit left at a nucleation site due to dryout of the microlayer; from these measurements, they estimate the microlayer thickness to be 1 - 3 μm for boiling of saturated water at atmospheric pressure.

Hendricks and Sharp [11] obtained surface temperature measurements similar to those of Moore and Mesler while simultaneously taking high speed movies of the bubble growth in order to correlate the temperature data with the presence of the bubble. Boiling of water on a thin metal strip at pressures reduced below atmospheric pressure was obtained with heat fluxes of 79 - 104 kW/m^2; the reduced pressures correspond to a subcooling of 3° - $11^\circ C$. They observed a very rapid temperature drop as the perimeter of the bubble base passed over the thermocouple. Twenty times the average heat flux was measured directly beneath the bubble during growth, and an appreciable decrease in heat flux was observed during lift off. They concluded that microlayer evaporation was the principal heat transfer mechanism in their experiments, while microconvection had a relatively small effect. We note that, in their experiments, the vapor bubbles grew to diameters of 20 - 40 mm and lifted off the surface after 30 - 70 msec. The measured heat fluxes were sufficient to evaporate a liquid thickness of 0.8 μm. They noted that the microlayer is probably thicker than this because dryout did not occur due to the small heat capacity of the heater.

Cooper and Lloyd [4, 5] formed micro-thermometers on a glass surface using the well developed technology of vacuum deposition of semiconductor material. The micro-thermometers exhibited a rapid response time and were precisely located so that a bubble grew out over four such thermometers. From high speed movie films, the bubble growth was correlated with the surface temperature time history. A single bubble was initiated by a small heat pulse in either toluene or isopropyl alcohol at a pressure of 6.9 or 13.8 kN/m^2, a subcooling of 1° - $2^\circ C$, and a heat flux of 22.7 or 47.3 kW/m^2. The bubbles grew to large diameters (20 - 40 mm) and had long lifetimes (30 - 60 msec). Cooper and Lloyd observed rapid temperature drops as the bubble base reached a micro-thermometer, followed a short time later by a sharp cut off. Microlayer thicknesses were calculated from a heat balance at each micro-thermometer location. Wedge-like microlayer profiles are indicated by the measurements at the four locations. From the thermometer nearest the center at a radius of 0.4 mm, the calculated microlayer thicknesses were in the range 4.6 - 8.9 μm; the largest microlayer thickness was calculated to be 56 μm at a radius of 6.1 mm.

Cooper and Lloyd [5] used a simple approximate boundary layer analysis to find an analytical expression for microlayer thickness. From dimensional analysis, we expect their resulting expression to be order of magnitude:

$$\delta(r) = \sqrt{\nu t_g} \quad , \tag{2.1}$$

where δ is microlayer thickness, ν is kinematic viscosity of the liquid, and t_g is the growth time for the bubble base to reach a radius r. Cooper and Lloyd found that the measured microlayer thickness agreed fairly well with that calculated from the above expression. The ratio of the measured value to the calculated value was in the range 0.5 - 1.0 with an average value of 0.8.

Results of the technique of measuring surface temperatures beneath a bubble confirm the existence of the microlayer and indicate that microlayer evaporation is a significant heat transfer mechanism for boiling at low subcooling. The microlayer thickness for water at atmospheric pressure has been estimated to be of the order of 1 - 3 μm. We note that this technique has been most successful for large bubbles with long lifetimes. For small bubbles with short lifetimes this technique may not be as successful. In particular, placement of more than one thermal sensor beneath a bubble would be difficult so that no detail of the microlayer profile could be obtained. The major advantage of this technique is that surface temperature is recorded directly so that interpretation of the data into surface heat flux and microlayer thickness is straightforward.

2.2 Measurements of the microlayer with interferometry

The first direct observation of the microlayer and the dryout was performed by Sharp [26] with an optical technique which made use of the properties of polarized light. Having verified the existence of the microlayer, Sharp attempted to measure the microlayer thickness using interferometry. The basic idea is that reflections from the top and bottom of the microlayer interfere to give fringe patterns which can be interpreted as thickness. Sharp's light source for interferometry was a mercury arc lamp with a collimating lens and spectral line filters. A plastic window was placed above the boiling surface at such a distance that the top of the bubble spread across the window. The reflections from the microlayer could then be imaged through the bubble and window into a high speed camera. The initial microlayer thickness for water was calculated from the fringe patterns to be wedge-like with a thickness of 0.4 μm at a radius of 0.94 mm. The microlayer evaporation rate was obtained from the time history of the fringe patterns.

Jawurek [15] followed Sharp's idea of measuring microlayer thickness with interferometry but made an important modification. Boiling was obtained by resistance heating of a thin transparent SnO_2 film deposited on a glass surface. The reflections from the microlayer could then be imaged through the glass from the bottom of the bubble so that the bubble growth was not constrained by an upper plate as in Sharp's experiment. Jawurek noted that boiling of water was not possible since the SnO_2 film and the contacts were destroyed, apparently by electrolytic action. Data were obtained for methanol and ethanol at system pressures of 20 - 50 kN/m^2, heat fluxes of 30 - 100 kW/m^2, and subcoolings of 0^o - 20^oC. The microlayer profiles are reported to be wedge-like with thicknesses of 0.2 - 0.8 μm at the outer edge (apparently at a radius of several millimeters although this is not stated explicitly).

The interferometric approach was also used by Voutsinos and Judd [29] with the modification of using a He-Ne laser to provide collimated, coherent, monochromatic light. More fringes were observed with the laser light than in an earlier system in which Judd had used a mercury light source. Voutsinos and Judd suggest that Sharp and Jawurek may have had similar difficulty obtaining the correct fringe order. Boiling was obtained on a glass plate by the method of Jawurek. Results were reported for methylene chloride at a pressure of 48 kN/m^2, a subcooling of 5.6°C, and a heat flux of 60.9 kW/m^2 with a wall superheat of 20.5°C. The microlayer profile is wedge-like with a thickness of 5 μm at a radius of 0.75 mm. From the time history of the microlayer profile, the microlayer evaporation can be determined. Voutsinos and Judd estimate that microlayer evaporation accounts for 25% of the total heat transfer rate. Judd has subsequently obtained more data [6, 16] although he only gives overall heat transfer results rather than detailed microlayer profiles.

The advantage of the interferometric approach is that detailed microlayer profiles can be obtained and the microlayer evaporation can be computed from the time histories available from the high speed photography. Such detailed information is necessary to further understand microlayer formation and evaporation. The disadvantage is that interpretation of the fringe patterns is not a trivial matter. Possible errors in interpretation of the fringe patterns have not been properly discussed in the literature and, in fact, several points appear to have been overlooked by previous investigators. The microlayer thickness results obtained by Sharp for water differ by an order of magnitude from the results obtained by the thermocouple technique. The results of Jawurek and those of Voutsinos and Judd for organic liquids at reduced pressures also differ by an order of magnitude. The discrepancies in these results are probably due to incorrect determination of the fringe order. Care must be taken to correctly interpret the fringe patterns. Finally, we remark that interferometry is the most promising approach for measurement of the microlayer beneath small, short-lived bubbles such as those occurring in highly subcooled nucleate boiling.

2.3 The Plesset-Prosperetti model of microlayer evaporation

The very high heat transfer rates of highly subcooled nucleate boiling are of the greatest engineering importance. However, most experimental and analytical studies treat near saturated conditions. The mechanism of heat transfer may be quite different for these two cases. Recently, Plesset and Prosperetti [23] have evaluated the role of microlayer evaporation in highly subcooled nucleate boiling. They have used the experimental data of Gunther [8] and of Gunther and Kreith [9] for highly subcooled water. Gunther and Kreith give accurate bubble growth and collapse measurements as a function of time for the vapor bubbles which maintain a hemispherical shape on the surface. The bubbles grow to a typical maximum radius of 0.5 mm with typical lifetimes of 0.5 msec. If it is assumed that viscous effects are negligible in the bubble growth, aside from the viscous microlayer, then the bubble radius is related to the internal pressure of the bubble by the Rayleigh-Plesset equation,

$$R \frac{d^2R}{dt^2} + \frac{3}{2} \left(\frac{dR}{dt}\right)^2 = \frac{1}{\rho} \left[p_i(t) - p_\infty - \frac{2\sigma}{R}\right] . \qquad (2.2)$$

From the R(t) data of Gunther and Kreith, the internal pressure $p_i(t)$ can be calculated. With $p_i(t)$ known, the evaporation rate at the surface of the microlayer can be related to the surface temperature. This relation for net mass flux J is given by kinetic theory (this relation is discussed in detail in Part II of this thesis),

$$J = \frac{p^e(T_b) - p_i(t)}{\sqrt{2\pi \mathcal{R} T_b}} , \qquad (2.3)$$

where $T_b(t)$ is the surface temperature and $p^e(T)$ is the equilibrium vapor pressure at temperature T. The unsteady heat conduction equation can then be solved in the liquid microlayer given an initial condition. To simplify to a one-dimensional problem, Plesset and Prosperetti assumed a microlayer of uniform thickness. The results of these calculations indicate that the total microlayer evaporation over the bubble lifetime is very sensitive to the microlayer thickness. Representative plots from their paper are shown in Figure 1. Plesset and Prosperetti estimated the microlayer thickness to be 6 - 9 μm based on the relation

$$\delta = \sqrt{\nu t_g} \quad . \qquad (2.4)$$

They thus concluded (see Fig. 1) that microlayer evaporation contributes only a small percentage of the overall heat flux for highly subcooled nucleate boiling of water. However, if the microlayer thickness were 2 - 4 μm, then their conclusion might be different. Hence, the theory requires detailed knowledge of the microlayer. For this reason, the present experimental investigation was undertaken to develop a technique to measure the microlayer for the small, short-lived vapor bubbles which occur in highly subcooled nucleate boiling.

III. EXPERIMENTAL APPARATUS AND PROCEDURE

3.1 The elements of interferometric measurements

We first consider the basic idea of the interferometric method for measurement of the microlayer. In Figure 2(a), a monochromatic plane wave is incident upon a layer of thickness d and index of refraction n_2. The reflected plane waves, taken to be of unit amplitude, differ in phase by the optical path length (o. p. l.),

$$\begin{aligned} \text{o.p.l.} &= 2n_2d \quad , \\ E_1 &= e^{i(kx-\omega t)} \quad , \\ E_2 &= e^{i[k(x+2n_2d)-\omega t]} \quad . \end{aligned} \tag{3.1}$$

The total reflected field E is the sum of the two reflected plane waves,

$$E = E_1 + E_2 \quad .$$

Photographic film (or the eye) is sensitive to intensity I,

$$I = EE^* = E_1E_1^* + E_2E_2^* + E_1E_2^* + E_1^*E_2 = 2 + 2\cos(2kdn_2) \quad . \tag{3.2}$$

If the layer thickness d varies with distance r as in Figure 2(b), then the intensity varies with r thus giving rise to a fringe pattern. The maximum intensity occurs at the points $d = \frac{\lambda}{2n_2}(m)$ and the minimum intensity occurs at the points $d = \frac{\lambda}{2n_2}(m + \frac{1}{2})$, where the integer m is the fringe order which must be determined from the zero reference $d = 0$. If the fringe order, the fringe spacing, and the index of refraction are known, then the thickness profile can be determined. We note that the changes in the index of refraction due to temperature variation introduce an error of only a few per cent when the thickness d is of the order of a few wavelengths of light. The experimental apparatus must be designed to implement this idea for the case of the microlayer formed beneath a vapor bubble on a heated solid.

3.2 The boiling cell

For imaging of the light reflected from the bounding surfaces of the microlayer, it is not only convenient but probably necessary to image from the bottom of the bubble through a transparent solid. We adopted Jawurek's method of boiling on glass by DC resistance heating of a thin SnO_2 film on the surface. Jawurek was not able to boil water with this arrangement, apparently because electrolytic action destroyed the film and contacts. We experienced similar difficulty, but by suitable modifications we were able to obtain boiling of water at atmospheric pressure with low heat flux.

Commercially available Pyrex Infrared Reflecting (IRR) Glass No. 7740 has a thin SnO_2 film coating. Being industrial glass, the optical quality is not high; however, this glass is suitable for design and testing of the boiling cell, especially so because of the moderate cost. On plates of dimension 1/8" x 2" x 2 1/2", the SnO_2 film was chemically removed [28] except for a rectangular (sometimes H-shaped) area in the center. This is done by melting master sheet wax onto the rectangular area, sprinkling powdered zinc over the rest of the surface, and dripping hydrochloric acid onto the zinc. The wax could then be removed by cutting, melting, and washing with acetone. Two clean copper strips were bonded to the edges of the rectangular area as shown in Figure 3. Several conducting adhesives were tested and the best results were obtained using the circuit board conducting paint "Silver Print". An attempt to use indium soldering was futile. The thickness of the SnO_2 film varies from plate to plate, but typically the resistance of the film is 50 - 70 $\Omega/\square$. With these film resistances, the boiling area dimensions were varied but were typically 1/2" x 1 1/2", which resulted in a resistance between the copper strips of 10 - 30 Ω. Fourteen gauge copper electrical cord was soldered to the copper strips and connected to a 40 VDC power supply which was connected to a Variac. The glass plate formed the bottom of the boiling cell. The four glass walls of the cell were joined with RTV silicon adhesive, and a gasket was formed around the bottom edge of the walls with RTV. The glass plate could be clamped against the gasket, which gave easy interchange of the boiling plates.

The fluids used in the present investigation were water and ethanol. Water ordinarily contains a significant amount of dissolved gases and is usually degassed for boiling experiments in which vapor bubble growth is to be studied. If the water is not degassed, then large gas bubbles form on the boiling surface at the nucleation sites and inhibit boiling. Distilled water was degassed by applying a vacuum on a bell jar filled with the water. An ordinary volume displacement vacuum pump was used with a cold trap to catch the water vapor. A heavy duty magnetic stirrer could stir the water through the thick glass bottom of the bell jar. With this arrangement, a liter of water could be degassed in 15 minutes. After degassing, the water was siphoned into a stainless steel pan and boiled on a hot plate. The heated water was then siphoned into the boiling cell. With this handling procedure, only a small amount of air is expected to diffuse back into the water. There was no need to degas the ethanol.

Boiling of water and ethanol could be attained using the cell described above. However, three problems were encountered. First, as Jawurek noted, the SnO_2 film is destroyed when water is used, apparently by electrolytic action. Secondly, although the "Silver Print" makes very good electrical contact between the copper strips and the SnO_2 film, the adhesive strength is not great. The copper strips would easily come loose from the surface, possibly as a result of thermal expansion. Both of these problems were satisfactorily resolved by applying a coating of RTV silicon adhesive to the copper strips as shown in Figure 3. The RTV provided the necessary adhesive strength to keep the copper strips in place and also inhibited the electrolysis. Water could then be boiled for sufficiently long periods of time although the cell would eventually fail due to film breakdown. The third problem is that only low heat fluxes are possible with this boiling cell. At higher heat fluxes, the SnO_2 film is destroyed. Apparently, the surface temperature becomes high enough in places that the thin film is evaporated. Usually, this evaporation propagates along a crack-like line near one of the copper strips. This problem could not be overcome with the present arrangement so that the boiling was limited to low heat flux. We note that ethanol could be boiled easily, but again there is an upper limit on the possible heat flux with the present boiling cell. Our experiments were conducted at atmospheric pressure; this boiling arrangement should perform very well at reduced pressures.

As noted earlier, the Pyrex IRR glass is not of high optical quality. In a batch of 20 plates, roughly half would be of acceptable optical flatness. However, on all of the plates, there are many pits in the surface ranging in diameter up to 100 μm with the majority in the 30 - 60 μm range. While being a nuisance optically, these pits facilitated boiling by serving as nucleation sites. In fact, when glass with a surface free from such pits was used, boiling could not be obtained before the SnO_2 film was destroyed. Apparently, without the pits the required surface superheat for boiling is so large that the SnO_2 film is evaporated in places. The Pyrex IRR glass was used and satisfactory fringe data could be obtained.

The heat flux was determined by measuring the dissipated power. The current was determined by measuring the voltage across a 1.07 Ω/8W shunt resistor, and the voltage was measured across the cell. The DC power dissipated was then computed from $P = VI$ and the heat flux was obtained by dividing by the heating area. Calibration of the power measurement indicated that an accuracy within a few per cent could be expected. The major source of error in determining the heat flux is the measurement of heating area. The assumption was made that the power is dissipated uniformly over the film area between the copper strips. Hence the reported heat flux calculated from this area is a mean value, and possible variations in heat flux over the heating area are not determined. We note that more boiling vapor bubbles were observed near the copper strips at the edge of the RTV than in the center region of the boiling area. The temperature of the bulk fluid was measured with a mercury-in-glass thermometer. No attempt was made to measure the wall superheat.

3.3 The laser interferometric-high speed camera system

Figure 4 shows a diagram of the experimental apparatus used to record the interference fringe patterns from the microlayer on movie film. Laser light is ideal for interferometry since it is plane polarized, highly collimated, coherent, monochromatic light. Furthermore, the power density of a laser beam can be very high. In high speed photography, exposure times are very small so that a high intensity at the film plane is required. Also, due to the low percentage reflection from the microlayer and the presence of several beamsplitters, losses in the optical system were expected to decrease the intensity from the source by a factor of a thousand. From these design requirements, a 2W Coherent Radiation Laboratories 52G argon ion laser was chosen as a suitable light source. The full beam from the argon ion laser is separated into the constituent wavelengths by an Oriel flint dispersing prism, and the green 514.5 nm wavelength is selected by an iris. From the specifications for the argon laser, the maximum power available for the 514.5 nm wavelength is 700 mW with a beam diameter of approximately 2 mm. However, in the course of these experiments, the power output fell below half of this value. Such power losses are usually due to a powdery film forming on the outside of the Brewster windows, and cleaning of the windows should correct the problem. Cleaning the outside of the windows did not correct the power loss; the film appeared to be on the inside of the windows. Because of the power loss, contraction of the beam was necessary in order to obtain sufficient intensity at the film plane.

Three 1" diameter dielectric mirrors mounted on Newport Research Corporation MM-2 mirror mounts were used to direct the beam onto a beamsplitter positioned between the objective and the boiling cell, as shown in Figures 3 and 4. The beam is reflected from the beamsplitter onto the bottom of the bubble with near normal incidence. The beams reflected from the microlayer pass through the beamsplitter and into the microscope assembly. A Cooke inverted microscope was adapted to accept Nikon attachments. The objective used was a Nikon Strain Free Achromat PM 5X (n. a. 0. 10, working distance 15. 0 mm). Strain free objectives are convenient with laser light since spurious interference often observed with lenses is reduced. The long working distance is necessary in order to allow space for the beamsplitter to be placed between the objective and the glass surface. A Nikon eye tube with a 5X eyepiece completes the microscope assembly. The eye tube is coupled to a Nikon CFM with a 1/4X projection lens which is designed to be used for cine photography through microscopes. A small portion of the light is reflected to an eyepiece on the CFM by a 15/85 beamsplitter while the majority of the light passes through to the film plane. The camera can thus be aligned and loaded, and visual observation can be continuously maintained even during filming. In the present system, the eyepiece of the CFM was not parfocal with the film plane. This slight inconvenience was remedied by measuring the position of the microscope stage with a machinist's dial indicator. The focus at the film plane could then be set by the dial indicator (the camera cannot be focused visually when loaded with film). The total magnification at the film plane was determined to be approximately 9X from photographs of a Nikon stage micrometer with 10 μm divisions. These photographs serve as a reference scale for measurements taken from the data films.

Movies were taken at a maximum framing rate of 15, 000 frames/sec with a 16 mm Fastax high speed movie camera with a half-frame prism. The half-frame prism reduces the height of a frame on the film to about one quarter of the frame width; for the system described above, the actual field of view is 0.27 mm x 1 mm. In order to image a bubble within this narrow field of view, the camera was aligned so that the center of the film plane precisely matched the center of the field of view of the CFM eyepiece which was marked with crosshairs. To establish an accurate time base, an LED timing light was designed and built which put timing marks on the edge of the film at 1 msec intervals. Light measurements necessary for correct film exposure were obtained with a United Detector Technology (UDT) 40X Optometer.

We note the following useful alignment considerations (refer to Figure 4). With the beam from mirror M3 brought in horizontally to the beamsplitter, the beamsplitter is adjusted to direct the beam normal to the glass bottom of the boiling cell; a visual determination of "normal" is sufficient. The mirror M3 can then be adjusted to give the maximum intensity at the film plane. The 1 mm thick beamsplitter produces fringe bands ("ghost images") due to interference of the reflections from each side. By rotating the beamsplitter with respect to the microscope (and realigning the incoming beam), these bands can be oriented along the width of the film plane. The mirror M3 can then be slightly adjusted to bring a bright band into the film plane. The bands are wide enough with respect to the height of the film plane that a fairly uniform intensity results over the film plane. The same consideration applies to orientation of the boiling cell. Interference bands result from the two surfaces of the glass plate. By rotating the boiling cell, a fairly uniform illumination can be obtained at the film plane.

3.4 Experimental procedure

The following procedure, being the end result of many improvements made in the course of this experiment, can be expected to result in a film with analyzable fringe patterns resulting from microlayer formation and evaporation. Distilled water is degassed and heated as described in Section 3.2. The laser beam is aligned with the beam-splitter and the microscope system as described in the last section. The Fastax camera is rotated out of alignment and the power density at the film plane is set using the UDT light meter. The optimum exposure is found by trial and error and depends on several variables; typically, a power density of 80 $\mu W/cm^2$ is used with a framing rate of 13,000 - 15,000 frames/sec (exposure time is approximately 1/5 of time between frames) and a film with exposure index of 400. With the laser power set, the laser beam is blocked and the camera is aligned with the center of the frame matching the crosshairs in the CFM eyepiece. The focus at the film plane is set by focusing on some surface pits of the actual cell to be used; the reading on the dial indicator is noted. The film can now be loaded into the camera. We remark that a Dolan-Jenner

Fiber-lite was found to be a very convenient white light source with which to illuminate from above.

The heated water is siphoned into the boiling cell and the DC voltage is increased until incipient boiling is attained. The most difficult part of the procedure is to locate an "appropriate" vapor bubble. An isolated natural nucleation site away from the edges of the boiling area is sought; the interaction with other bubbles is avoided for purposes of interpretation of the fringe patterns. Several types of bubble growth were noted. High frequency bubbles (100 bubbles/sec) are usually small (1 mm diameter) and form bubble streams above the nucleation site. Low frequency bubbles (10 bubbles/sec) grow to larger sizes and bubble streams are not evident. Other nucleation sites were intermittent, with some having an occasional burst of high frequency and otherwise no bubbles, and others with only an occasional single bubble. We note that the laser light shining through the bubbles creates a strobe effect so that both the frequency and size of the bubbles can be estimated visually. This same effect helps in locating a nucleation site; when viewed in the microscope under white light, the bubbles appear to be a blur, and locating and centering the nucleation site is difficult.

Once an appropriate bubble type is located, the nucleation site is judged with optical considerations by viewing under laser light. The nucleation site may be a pit which creates spurious interference patterns, or nearby pits may create troublesome interference patterns. The nucleation site may be at a null point of the background interference bands. In either case, another nucleation site must be sought.

Eventually, an isolated nucleation site with a fairly "clean" background interference can be located. The boiling cell is rotated to align the background interference bands as described in Section 3.3, and the nucleation site is centered. With the laser on and the timing light on, the film is taken. The temperature of the bulk fluid is read, the heat flux meters are read, and all necessary information is recorded on a data sheet identified with the film.

Facilities were available for manual processing of 100 ft. lengths of 16 mm movie film. Manual processing was convenient because test strips from the film could be used to determine the developing time for best results. Kodak D-19 developer was used to give a high contrast. Best results were obtained with Kodak 2498 RAR film, and Kodak 2479 RAR film also gave good results. Eastman 4X-N film was much grainier and was overly sensitive to the D-19 developer. The developed negative film could be printed frame by frame with a maximum enlargement of 17.3X. Most of the data were taken by viewing the fringes on a film reader with a magnification of 37.5X. Examples of the fringe patterns resulting from the above experimental procedure are shown in Figures 5 and 6.

IV. INTERPRETATION OF THE FRINGE PATTERNS

4.1 Optical background noise and fringe contrast

Using the experimental apparatus and procedure described in Chapter III, we can obtain films of the fringe patterns resulting from microlayer formation and evaporation. The fringe patterns, such as those shown in Figures 5 and 6, must be interpreted into microlayer thickness profiles. The interpretation at first appears to be straightforward but is in fact not a trivial matter, and several points appear to have been overlooked by previous investigators. As mentioned previously, laser light is convenient for interferometry because it is well-collimated, coherent, monochromatic light. The high degree of coherence is described by saying that laser light has a long coherence length (for the laser used, several centimeters); that is, in the present application, two reflected beams can interfere even when the difference in optical path length is several millimeters. For the present situation, described by Figure 7, the reflections from four surfaces must be considered. Reflections E_2 and E_3 interfere to give the microlayer fringe patterns. Reflections E_1 and E_2 interfere to give the broad bands, shown in Figure 5, due to the thickness variation of the glass. These bands can be considered to be optical background noise and do not present a serious problem, although they can be a nuisance. The reflection E_4 from the top of the bubble will be considered subsequently.

We note that the fringe contrast from E_2 and E_3 was expected to be poor, but fortunately, as is evident in Figures 5 and 6, the fringes are reasonably clear. From the Fresnel equations [10] for normal incidence, the reflected intensity at an interface as a percentage of the incident intensity is given in terms of the indices of refraction of the two sides of the interface,

$$\frac{I_r}{I_i} = \left(\frac{n_2 - n_1}{n_2 + n_1}\right)^2 \quad . \tag{4.1}$$

Hence E_1 should be 4%, E_2 should be 0.3% (without the SnO_2 film), and E_3 should be 2% of the incident beam; with the SnO_2 film, E_2 was measured to be 10 - 20% of the incident beam. Since E_3 is relatively small compared to E_1 and E_2, we would expect fringes with a small intensity variation to be superimposed on a large DC intensity, resulting in poor fringe contrast. However, photographic film is sensitive over a relatively narrow range of intensity compared to the DC level necessary for good exposure. Apparently, the fringe intensity variation is large enough compared to the film sensitivity range to record fringes of reasonable contrast.

4.2 Calibration

Some calibration tests were performed with the interferometric system to determine the spatial resolution of the system and to check the interpretation of fringe patterns resulting from known thickness profiles. In the first series of tests, wedges were formed with microscope cover slips on top of a glass plate. The cover slips are 20 mm square with a uniform thickness of 0.17 mm. With one cover slip under one edge of another, a wedge is formed with a slope of 0.0085 relative to the glass plate. The slope can be increased by the insertion of additional cover slips. The fringe pattern due to the interference of the reflections from the cover slip and the glass plate is a series of equally spaced straight fringes as shown in Figure 8(a). The height change h of the wedge from one fringe to the next is one fringe order,

$$h = \frac{\lambda}{2n_{air}} = \frac{0.5145\ \mu m}{2(1.0)} \quad . \tag{4.2}$$

The spacing between the fringes is measured with the Nikon stage micrometer as a reference length. The slope thus determined agrees within a few per cent with the slope calculated from direct measurement. The interferometry can be expected to be the more accurate measurement. As the wedge slope is increased, the fringes become spaced more closely. The slope can be increased until the fringes cannot be resolved. The maximum detectable slope measured in this way is 0.063 corresponding to a maximum detectable wedge angle of 3.6° and a minimum detectable fringe spacing of 4 μm. Thus, with the system under the best possible conditions (i.e. static fringes, good film grain, and low optical background noise), the spatial resolution of fringes is measured to be 4 μm.

The second series of tests was conducted with a 20.6 mm diameter steel ball sitting on a glass plate in order to check a thickness profile with curvature. The resulting concentric fringe pattern, shown in Figure 8(b), is commonly referred to as Newton's rings. From this fringe pattern, we can determine the diameter of the ball. The height h of the ball surface above the plate is

$$h = R\left[1 - \sqrt{1 - \left(\frac{x}{R}\right)^2}\right] \quad . \tag{4.3}$$

For fringes near the contact point, so that $\frac{x}{R} \ll 1$, we can make the approximation

$$h \approx \frac{x^2}{2R} \quad . \tag{4.4}$$

We can measure $h(x)$ from the fringe pattern and thus compute the diameter $2R$,

$$2R = \frac{x_m^2}{(\frac{\lambda}{2n})m} \quad , \tag{4.5}$$

where m is the fringe order. Imperfect optical contact of the ball with the glass plate can result from dust particles or grease films. The diameter is more accurately determined by measuring the change between two large fringe orders m and ℓ [21],

$$2R = \frac{x_m^2 - x_\ell^2}{\frac{\lambda}{2n}(m - \ell)} \quad . \tag{4.6}$$

Referring to Figure 8(b), we note that the position of the actual fringe differs by Δx from the point of reflection on the ball surface. However, the slope and the distance h are so small that the distance Δx is smaller than the resolution limit of the optical system. If the experimental procedure and measurements are performed carefully, then the diameter of the ball calculated from the fringe pattern agrees with the measured diameter within 2%; if not done so carefully, then the error in diameter may be 10%. However, the diameter is proportional to x^2, so the fringe position x is accurate to within 5%. Thus, a thickness profile with curvature can be measured accurately to within

5% with the interferometric system, and the accuracy may be much better.

With the ball and the glass plate arrangement, the effect of focus error could also be studied. Everyone who has used a microscope or a camera understands intuitively what is meant by being "in focus" at the film plane. With ordinary lighting, light is scattered from a point on an object. From a geometrical optics viewpoint, the object is in focus at the precise distance from the objective such that all rays of light leaving a point on the object meet at a single point on the film plane. Thus, focus is well defined and measurements from a picture in focus can be taken if a picture of a reference length in focus is available. With laser light, the same statement is true, but one must be careful that the focus is properly set. Because laser light is so well collimated, the reflection from a point on a smooth surface is actually a single ray of light. Furthermore, the fringe pattern at the film plane is the result of interference between several rays with only one coming from each point of each surface in the optical path. If the distance of the object from the objective is changed, then the fringe pattern at the film plane changes. However, the fringe pattern is only shifted in a geometrical way and we cannot perceive whether the optical system is "in focus"; fringe patterns always appear to be in focus. The focus must be set by viewing with white light; the dial indicator arrangement discussed in Chapter III is convenient for setting focus. Similar consideration must be given to the concept of depth of field. With ordinary light, as an object is moved out of focus, we perceive a blurred image. Depth of field is the distance beyond an object in focus at which another object still "appears" to be in focus as measured by some resolution limit. If an object is far beyond the depth of field, then the blurring can be so extensive that the object cannot be seen at all; hence we do not see the microscope slide beneath a transparent specimen. With laser light, the usual concept of depth of field has no meaning. Any two reflections with a difference in optical path length less than the coherence length of the laser can interfere to produce fringes. Thus, surfaces that are far away as measured by the depth of field of the optical system can still affect the image. Such spurious interference can be a disadvantage of laser light and must certainly be considered in any interferometric system.

4.3 The top of the bubble problem

Reflections from three of the four surfaces in Figure 7 have been considered. The fringe bands due to the glass plate are static, widely spaced, and straight and are thus easily distinguished from the dynamic, concentric, circular fringes from the microlayer. Since laser light has a long coherence length, the reflection from the top of the bubble must also be considered. The resulting fringes are also dynamic, concentric circles associated with the bubble growth. The existence of these fringes requires that several questions must be answered. First, how do we know that the fringes in Figures 5 and 6 are not totally due to the top of the bubble? Second, if both these fringes and the microlayer fringes are present, then how can we distinguish one from the other? Third, if we feel that the fringes in Figures 5 and 6 are totally due to the microlayer, then how can we dismiss the fringes from the top of the bubble?

In order to characterize the fringes from the top of the bubble, quasi-static CO_2 bubbles in soda water were studied. These bubbles grew very slowly due to diffusion into the bubble of the dissolved CO_2. For bubbles of the same size range as observed in the boiling, the fringes from the top of the bubbles were observed and 35 mm photographs were taken. From the typical photograph in Figure 9, we note that the fringe spacing decreases with increasing radial position; the opposite is true of the fringes in Figure 5 and 6. Also the fringes from the top of the bubble were observed only in a very small region near the center of the bubble, typically of diameter about 10 - 20% of the bubble diameter; the fringes in Figures 5 and 6 are observed to cover a much larger area. From these observations, we felt that the fringes in Figures 5 and 6 were due entirely to the microlayer. The reason that the fringes from the top of the bubble do not appear was understood when it was observed that considerable motion of these fringes occurred with the very slow diffusional growth of the CO_2 bubbles. The argument is similar to that used in the method of stationary phase. The difference in optical path length between E_4 and E_2 in Figure 7 is of the order of the bubble diameter 2a. The sinusoidal interference term in equation (3.2) thus varies with the bubble growth rate. If the interference term is rapidly varying with respect to the exposure time of the film, then the fringes will cancel one another, leaving a uniform intensity on the film instead of fringes. Even though the exposure time is only 13 μsec, the slowest bubble growth rates observed change the optical path length by 9 fringe orders in this time. Thus, the fringes from the top of the bubble will not appear in the films. However, we must be aware that these fringes could appear if, for example, the growth rate is extremely slow or if an extremely short exposure time is used.

4.4 The maximum detectable slope

The maximum slope detectable with the present interferometric system is limited in two ways. We have already noted in Section 4.1 that the maximum detectable slope is limited by the possible spatial resolution of the optical system. For the static case, we measure a fringe resolution of 4 μm; for the dynamic case, we estimate from the films that the fringe resolution is about 5 μm. This fringe resolution corresponds to a maximum slope of 0.0385 or a maximum wedge angle of 2.2°. The detectable slope is also limited by the light collection of the optics which is related to the numerical aperture of the objective. In Figure 7, the ray E_3 must hit the objective to be imaged. If the slope of the upper surface of the microlayer is too great, then the reflected ray will not be imaged. From simple geometrical considerations, this constraint can be estimated to correspond to a maximum wedge angle of 3.8° at the center of the bubble and of 2.9° at a radius of 0.5 mm. The constraints of light collection and fringe resolution are of the same order although the fringe resolution appears to be the limiting consideration.

The greatest limitation of the interferometric approach for microlayer measurement is that the resolution of the optical system limits the maximum detectable slope. Two points must be carefully considered. First, the outer edge of the fringe patterns in Figures 5 and 6 does not necessarily correspond to the edge of the bubble.

Referring to Figure 7, we can imagine that there could be a significant region of the microlayer near the edge of the bubble with slope greater than 0.0385. Thus, a portion of the microlayer may not be detected. Of more importance, the bubble growth rate cannot be computed from the growth rate of the fringe patterns unless it can be shown that the two rates are the same or that they can be related. We shall consider this point further in the discussion of the results.

The second point to consider carries the most serious consequences and is the most difficult problem to resolve. The contact angle of the microlayer with the glass is not necessarily less than 2.2°. If the contact angle is greater than 2.2°, then some fringes cannot be resolved so that the correct fringe order is not known. Our method of interferometry relies crucially on the determination of the correct fringe order. If the correct fringe order is not known, then the microlayer thickness and evaporation rate results are in error. A major effort of the present investigation was attempting to resolve this question of contact angle. If the contact angle is greater than 2.2°, then we should see the fringes becoming very closely spaced near the edge of the dry spot. In Figure 5 and especially in Figure 6, the fringes do not appear to become much closer near the dry spot; rather, the spacing appears to be fairly uniform. However, the fringe contrast combined with the optical background noise makes the determination of the first fringe difficult so that the above argument is not conclusive. In order to strengthen this argument, data films of ethanol were taken with a higher power objective in order to magnify the fringes near the dry spot. A Leitz 32/0.30 objective was used with the same system, resulting in an increased magnification by a factor of 4. Films of the dry spot growing across the frame were obtained and some representative frames are shown in Figure 10. The exposure was somewhat low because sufficient laser power was not available. However, no evidence of closer fringe spacing can be seen. We believe that the fringe order is correctly determined with the present system. Further efforts should be undertaken to confirm this belief. We note that one such effort that we attempted was to use the full beam of the argon laser. From the two primary wavelengths, we hoped to be able to uniquely determine the microlayer thickness. Unfortunately, the background noise was so great with the full beam that the fringes could not be clearly distinguished. This approach may be profitable in future efforts.

4.5 Reduction of data

The necessary considerations for interpretation of the microlayer fringe patterns have been discussed. From the calibration tests, we have confidence that the thickness profiles will be accurate if the correct fringe order can be determined. With the present interferometric system, we know that fringes from the top of the bubble are not recorded on the film, so that the dynamic, concentric, circular fringes are due entirely to the microlayer formation and evaporation. Finally, we have presented some evidence that all of the fringes are resolved near the contact point of the microlayer and the glass. Thus, we assume in the data reduction that we can determine the correct fringe order. The only step left is to measure the radial position of the fringes from the center of the bubble.

The fringes in Figures 5 and 6 are clear enough that the center of each fringe can be determined visually. When the data films are viewed on the film reader, the clarity is somewhat better than from a print. The circular symmetry of the fringes is evident, and measurements show that the deviation from a circle is less than 5%. Hence the simplest procedure is to measure the diameter of the fringes and spot check that the symmetry is maintained. The diameter is measured with a draftsman's rule to the nearest hundredth of an inch. The measurements taken by this procedure are reproducible for all fringes within 5% and for the majority of fringes within 2%. In the first several frames before the dry spot has grown much, the fringes near the center are obscured by the optical noise from the pit on the surface. It is difficult to determine the correct fringe order in these frames. We used the following procedure to determine the fringe order. The fringe order can be clearly determined in a frame with a large dry spot. The fringes can then be tracked in a reasonable way to the preceding frame and so on to the first frame. The number of fringes obscured by the pit can thus be determined by this procedure. With the fringe order and radial position of each fringe determined, we can plot the microlayer profile for each frame. Typical results are shown in Figures 11-14.

V. RESULTS AND DISCUSSION

5.1 General discussion

Data films of fringe patterns due to microlayer formation and evaporation have been obtained with the experimental apparatus and procedure described in Chapter III; representative frames from these films are shown in Figures 5 and 6. The interpretation of these fringe patterns into microlayer thickness profiles has been discussed in Chapter IV. The microlayer thickness profiles corresponding to the data of Figures 5 and 6 are given in Figures 11-14. In each of Figures 11-14, a series of microlayer profiles are shown. Each profile corresponds to a different instant of time as designated by the frame number which is counted from the first frame in which bubble growth is observed. The actual time from one frame to the next can be computed from the framing rate given in each figure heading; the framing rate varies by only 1/2% over the bubble lifetime. The thickness is given in terms of the measured fringe order, and the corresponding actual distance scale is also shown. The thickness is plotted as a function of the radius from the center of the bubble. We note that the contact angles shown are close to 1°.

For the conditions of a fluid at low subcooling and atmospheric pressure boiling at low heat flux, the typical bubble growth sequence is as follows. A very rapid initial growth occurs after a waiting period following the previous bubble. The waiting period is the inverse of bubble nucleation frequency and can vary depending on the nucleation site and the boiling conditions. As mentioned previously, the nucleation frequency may be regular or intermittent. The rapid initial growth lasts for just a small fraction of a millisecond and a much slower growth continues. The microlayer is formed beneath the bubble during the bubble growth, and evaporation of the microlayer continues throughout the bubble lifetime as evidenced by the growth of the dry spot. The dry spot grows all the way to the visible edge of the microlayer in a typical time of a few milliseconds. The dry spot then contracts (rewetting) as the bubble lifts off the surface, typically in a time of a couple of milliseconds. We note that the last profile shown in Figures 11-14 is not at the end of the bubble lifetime. Only a sufficient number of profiles have been plotted to indicate the magnitude of the microlayer evaporation. The dry spot does grow all the way to the visible edge of the microlayer indicated in the figures. The contraction of the dry spot could be seen in motion pictures but the contrast is too low for measurement in single frames.

We have noted that the microlayer profiles change with time due to evaporation of the microlayer, but the profiles could also change as a result of radial fluid motion in the microlayer. It is generally accepted that any motion in the microlayer is rapidly damped due to viscous forces. The following argument due to Cooper and Lloyd [5] is convincing. We will consider the case of a water vapor bubble which grows to a radius of 1 mm in 1 msec. A typical microlayer thickness is 2 μm. The Reynolds number is then on the order of 7 so that the convective terms can be neglected. The microlayer is nearly plane so that the pressure on the liquid-vapor interface can be taken to be uniform. If surface tension gradients are assumed to be small, then the boundary condition at the liquid-vapor interface is zero shear. The no slip boundary condition is assumed to hold at the solid surface. An initial velocity profile is assumed to be related to the bubble growth rate. The situation is typical of lubrication problems so that the governing equation is

$$\frac{\partial u}{\partial t} = \nu \frac{\partial^2 u}{\partial z^2} \quad , \tag{5.1}$$

where u is the radial velocity, z is the coordinate normal to the surface, and ν is the kinematic viscosity. The solution to this equation with the above boundary conditions can be obtained by separation of variables and is of the form

$$u = \sum_{m=1}^{\infty} \{u_m \sin(2m+1)\frac{\pi}{2} z \quad \exp[-(2m+1)^2 \frac{\pi^2}{4} \frac{\nu t}{\delta^2}]\} \ . \tag{5.2}$$

The radial velocity in the microlayer decays rapidly in a time of the order $\frac{\delta^2}{\nu}$ which is of the order of microseconds. Thus, we assume that all movement of the fringe patterns is due solely to microlayer evaporation. We note that there is also some experimental evidence to support this assumption [17]. With this assumption, we see that a great deal of information is available in Figures 11-14. These results give detailed microlayer thickness profiles as well as the rate of evaporation from the microlayer over the bubble lifetime.

Finally, we note that the data in Figures 11-14 are obtained from two data films, one for ethanol and one for water. These data are considered to be typical for a single nucleation site with the given conditions. The bubbles chosen for data reduction are considered to be the best data available based on fringe contrast, optical background noise, and symmetry of the fringes. Other films with poorer fringe contrast or with too much optical background noise for interpretation showed bubbles with similar characteristics as in the data films used. Asymmetry of the fringes occurred in some films, resulting from either surface irregularities, such as scratches or pits, or from interaction with bubbles from nearby nucleation sites. The data films used are actually quite clear and we have confidence in our resulting interpretation of the fringe patterns.

5.2 Results of experiments with ethanol

The ethanol data presented in Figures 11-13 are taken from the same data film which contains a total of 11 bubbles originating from the same nucleation site. The pool boiling occurred at atmospheric pressure with a measured mean heat flux of 26.5 kW/m^2 and a bulk fluid temperature of 72.8°C (a subcooling of 5.7°C). The bubble growth observed on this film is very regular with bubble nucleation frequencies of 16.6 bubbles/sec (or a period of 60.4 msec) which vary only ± 10% and maximum bubble diameters (based on the edge of the fringe pattern) between 0.7 mm and 1.16 mm with an average maximum diameter of 0.89 mm. The bubble lifetimes at the surface consist of 2.5 - 5.5 msec of microlayer evaporation with another 2 - 4 msec in which the dry spot contracts as the bubble lifts off the surface. The waiting period between departure of a bubble and nucleation of the next bubble is thus typically 50 - 60 msec.

The microlayer formation and evaporation shown in Figures 11-13 is very reproducible from figure to figure as would be expected from the bubble growth behavior. The initial microlayer profile is wedge-like with a thickness of 3 μm at a radius of 0.25 mm. We note that Jawurek's [15] measurements for ethanol were an order of magnitude less than the present measurement. Although the conditions were different in the two experiments, this order of magnitude difference is an indication that Jawurek may not have determined the correct fringe order. Our thickness measurements are similar to those of Voutsinos and Judd [29] and Cooper and Lloyd [4, 5], although the fluids and conditions are different. A very striking feature of the results in Figures 11-13 is that the evaporation rate from the microlayer appears to be fairly uniform over the microlayer surface, giving similar profiles as evaporation proceeds. Actually the evaporation rate is greater near the contact point, being 15 - 30% greater than the evaporation rate near the outer edge of the microlayer. The approximate thickness evaporation rate over the microlayer surface is initially 2.2 μm/msec and decreases to 1.25 μm/msec after about 1.4 msec. These evaporation rates correspond to heat fluxes of 1385 kW/m^2 and 787 kW/m^2 respectively, where the conversion is made by multiplying by density and the latent heat of vaporization (see Appendix). Although extremely large, these heat fluxes occur only over short periods of time and over a small area, and the overall effect of the microlayer evaporation on the heat transfer rate may or may not be significant depending on the bubble nucleation frequency and the nucleation site number density.

We shall consider the overall effect of microlayer evaporation on the heat transfer rate in Section 5.4.

In Section 4.4, we expressed concern that the fringe order may not be correctly determined if the contact angle of the microlayer with the glass plate is greater than approximately 2.2°. Our concern was amplified when it was found that the fringe patterns represented in Figures 11-13 did not change position very much from frame to frame. The problem is that if the microlayer thickness were constant in time (little or no evaporation), then the fringe spacing should remain the same from frame to frame. Could this nearly identical spacing be a coincidence or could we be determining the wrong fringe order when, in fact, the microlayer thickness is nearly constant in time? In Section 4.4, we have briefly described the experimental attempts to determine if the fringe order is correctly determined. Our belief that the fringe order is correctly determined is best supported by the experiments with ethanol in which higher magnification films were obtained of the dry spot growth, as shown in Figure 10. The corresponding profiles of the contact angle are shown in Figure 15. The distance measurements were taken with respect to a fixed reference point on the right edge of the film frame and are presented accordingly. We note that the fringes do change position from frame to frame in Figure 15. Furthermore, the contact angle and the evaporation rate are in close agreement with the data of Figures 11-13. Hence, the data of Figures 11-13 appear to be correct and we have no reason to doubt that the fringe order is correctly determined.

5.3 Results of experiments with water

The data for water presented in Figure 14 are taken from a data film which contains a total of 9 bubbles originating from the same nucleation site. The pool boiling occurred at atmospheric pressure with a measured mean heat flux of 204 kW/m^2 and a bulk fluid temperature of 78.3°C (a subcooling of 21.7°C). The bubble nucleation is intermittent with times between bubbles as short as 34 msec and as long as 200 msec; the data presented are for a bubble which occurred 72 msec after the preceding bubble. The bubble fringe patterns grew beyond the field of view of the camera frame and the edge of the film frame is noted in Figure 14. The microlayer evaporation lasted for 3.8 msec and the dry spot contracted in another few milliseconds. The bubble nucleates from within a rather large pit as can be seen in Figure 6.

From Figure 14, we see that the initial microlayer profile for water is wedge-like with a thickness of 1.85 μm at a radius of 0.25 mm. We have noted previously that a discrepancy exists in the literature regarding the order of magnitude of the microlayer thickness for water. Our data resolve this discrepancy and indicate that the data obtained by the thermocouple approach are correct. The data of Sharp [26] are probably in error, possibly due to incorrect determination of fringe order. The characteristics of the microlayer evaporation are the same for water as for ethanol. The approximate thickness evaporation rate for water is initially 1.04 μm/msec and decreases to 0.35 μm/msec after about 2 msec. These thickness evaporation rates are lower than those for ethanol, but the corresponding heat fluxes, 2256 kW/m^2

and 757 kW/m^2 respectively, are of the same magnitude and greater than those for ethanol due to the much larger latent heat of vaporization of water and also to the greater density of water.

We have noted in Section 4.4 that the growth rate of the edge of the fringe pattern may not be the same as the growth rate of the bubble radius. We were not able to obtain simultaneous movies of the fringe patterns and the bubble growth for comparison, but we tried the only alternative available. Immediately after the interference data film was taken, the camera was reloaded and a movie of the same nucleation site was taken with white light. The edge of the bubble reflects the light from above away from the objective so that a silhouette of the bubble edge is obtained. The growth is very rapid so that the edge appears in only two or three frames. The bubble growth rate can be measured approximately. The results indicate that the growth rate of the edge of the fringe pattern is lower than the bubble growth rate by 15 - 35%. With some idea of the bubble growth rates, we can check our initial microlayer thickness measurements against Cooper and Lloyd's expression,

$$\delta = C\sqrt{\nu t_g} \quad , \tag{5.3}$$

where Cooper and Lloyd found $C = 0.8$. Based on the growth rate of the edge of the fringe pattern, we estimate from Figures 11-14 that C is in the range 0.3 - 0.4. If these growth rates are corrected by 15 - 35%, then the C is in the range 0.33 - 0.5. Our estimate of C is significantly lower than the value of 0.8 suggested by Cooper and Lloyd. We note that the proportionality in equation (5.3) is not definitely established as the correct form for microlayer formation. Cooper and Lloyd's results agree well with this form and our results also appear to follow this form. However, there is some experimental evidence that the microlayer thickness increases with increasing bubble growth rate [7, 17]. A recent analytical estimate of the microlayer thickness has been obtained by Plesset and Sadhal [24] based on the exact solution of the boundary layer equations for a point sink on a wall. They also find that the microlayer thickness is proportional to $\sqrt{\nu t_g}$. Of particular interest is their finding that an exact solution of the boundary layer equations for a point source on a wall does not exist. They presume that the difficulty is that regions of reverse flow may exist in the potential flow field during bubble growth. Thus, the microlayer formation problem is very complicated and may require an exact solution of the Navier-Stokes equations.

5.4 Implications regarding microlayer evaporation as a heat transfer mechanism in nucleate boiling

The detailed measurements of microlayer formation and evaporation available from the interferometric approach can be used in several ways to determine the importance of microlayer evaporation as a heat transfer mechanism in nucleate boiling. The direct approach is to use the measurements to calculate the percentage of the total heat flux due to microlayer evaporation. As an example, we shall use the direct approach for the ethanol data. We first assume that the measurements in Figures 11-13 are typical of all active nucleation sites. The typical bubble diameter is 0.89 mm, and from the figures we estimate that the total volume of liquid evaporated beneath a single bubble of this diameter is 2.15×10^{-12} m^3. The energy required to evaporate this volume is 1.35×10^{-3} joules. The bubble frequency is 1 bubble/60 msec, and we estimate by visual observation that the active nucleation site density is $6.2 \times 10^4 \; \frac{\text{sites}}{\text{m}^2}$. The heat flux due to microlayer evaporation is thus 1.4 kW/m^2. We can compare this to the measured heat flux of 26.5 kW/m^2. Because the boiling is occurring just at the onset of nucleate boiling, the dominant heat transfer mechanism is still natural convection. The natural convection heat transfer must be subtracted in order to determine the effect of the boiling. For the small difference here, we can not expect to obtain an accurate estimate of the effect of the bubbles. However, for larger boiling heat fluxes, this approach can be used to obtain a good estimate of the contribution of microlayer evaporation to the enhanced heat transfer due to boiling. We might expect that as the heat flux is increased, the energy per bubble required for microlayer evaporation will remain about the same. The bubble nucleation frequency and the nucleation site number density both increase with increasing heat flux so that the overall contribution of microlayer evaporation will also increase.

The measurements of microlayer thickness can also be used as an input to analytical models which attempt to assess the contribution of microlayer evaporation heat transfer. The model of Plesset and Prosperetti described in Section 2.3 is of particular interest because the important case of highly subcooled nucleate boiling is considered. Their results for the total energy extracted from the microlayer per bubble as a function of the unknown microlayer thickness (assumed uniform) are shown in Figure 1. Their conclusion that the contribution of microlayer evaporation is small is based on the relation $\delta = \sqrt{\nu t_g}$. The present measurements indicate that the microlayer thickness is very close to the values which give the peaks shown in Figure 1. Therefore, it appears that microlayer evaporation may account for a significant part of the total heat transfer per bubble. We note that the growth times for microlayer formation in the Gunther and Kreith data used by Plesset and Prosperetti are close to the growth times in our experiments; hence the microlayer profiles can be assumed to be comparable.

The measurements of microlayer thickness can also be used to obtain an upper bound on the energy which can be extracted from the microlayer per bubble. For the data of Gunther and Kreith, the experimental value of the total energy transferred due to a single bubble is shown in Figure 1. We can estimate the microlayer profile for these bubbles from our data if we assume that the proportionality $\delta \propto \sqrt{\nu t_g}$ correctly describes microlayer formation; since the viscosity and growth times are almost the same, the microlayer profiles are assumed to be the same. The latent heat required to evaporate the total mass of the microlayer represents an upper bound on the energy which can be extracted from the microlayer. For the case of highly subcooled nucleate boiling represented by the data of Figure 1, microlayer evaporation can account for a maximum of about 50% of the total heat transfer. Thus, microlayer evaporation alone cannot account for the increased heat transfer observed in highly subcooled nucleate boiling.

Assuming that microlayer evaporation and microconvection are the only competing mechanisms to describe the increased heat transfer in nucleate boiling, we can now draw some conclusions regarding the relative contribution of each. Previous experiments have shown that microlayer evaporation may be the dominant mechanism at low subcooling. We have seen how this is possible since a relatively large amount of energy is extracted by the complete evaporation of the microlayer in our experiments. For high subcooling, however, we have determined that microlayer evaporation can account for a maximum of 50% of the total heat transfer. Thus, microconvection must be the dominant mechanism for high subcooling, although microlayer evaporation may be significant.

5.5 Conclusions and future work

In the present investigation, we are concerned with the fundamental problem of understanding the mechanism by which the heat transfer rate from a solid to a liquid is significantly increased by the occurrence of nucleate boiling. The mechanism must be associated with the presence of the bubbles on the solid surface, and presumably the study of a single bubble is sufficient for the understanding of the mechanism. Two proposed mechanisms related to the behavior of a single bubble are microconvection, in which the bubble motion creates mixing between the hot thermal layer and the cooler bulk liquid, and microlayer evaporation, in which the evaporation from a thin liquid layer beneath the bubble extracts energy from the solid surface. Progress in understanding the microlayer evaporation phenomenon has been impeded by the unavailability of a solution to the fluid mechanical problem of microlayer formation. Specifically, the microlayer thickness profile is needed, and experimental measurement is required. In this investigation, an experimental measurement of the microlayer thickness profile has been made.

We have chosen to use interferometry for the measurement of the microlayer because of the detail potentially available with this measurement technique. A laser interferometric-high speed camera system has been developed with which microlayer profiles can be obtained for small, short-lived bubbles such as those which occur in highly subcooled nucleate boiling. Previous investigations have dealt only with large, long lifetime bubbles. Furthermore, previous investigators have not carefully discussed the interpretation of the fringe patterns. A significant contribution of the present investigation is a discussion of the problems of interpretation of the fringe patterns and the subsequent limitations on the measurement technique. Of primary importance is the fringe resolution limit of the interferometric system. All of the fringes near the contact point of the microlayer with the glass surface must be resolved in order to determine the correct fringe order. Previous investigators apparently have not considered this point carefully but have merely assumed that all the fringes were resolved (i. e. assumed that the contact angle is small enough). We have carefully analyzed our interferometric system and have confidence that the fringe order has been correctly determined.

The interferometric system has been used to obtain time histories of the microlayer profile for the cases of ethanol and water boiling at atmospheric pressure and low subcooling with low heat flux. The water data are significant in that these are the first data of detailed microlayer profiles for water. These data resolve a discrepancy in the literature regarding the order of magnitude of the microlayer thickness for water; we have found that the microlayer thickness for water boiling at atmospheric pressure is of the order of a few micrometers. Not only is the initial microlayer profile available from these data, but also the evaporation rates from the microlayer have been determined. It is interesting that evaporation over that surface of the microlayer is fairly uniform. The measured evaporation rates are very large and indicate that microlayer evaporation may be a significant heat transfer mechanism in some cases. However, from our measurements and the measurements of Gunther and Kreith, we have estimated that microlayer evaporation can account for a maximum of 50% of the total heat transfer rate in highly subcooled nucleate boiling. Thus, microconvection must be the dominant heat transfer mechanism in highly subcooled nucleate boiling, although microlayer evaporation may be significant.

The interferometric measurement technique used in the present investigation can be used to obtain further measurements to improve the understanding of microlayer formation and evaporation. The following investigations are suggested:

1. Microlayer formation is not well understood and experimental measurements of initial microlayer profiles for a range of conditions should provide a guide for analytical efforts and for empirical correlations. The only existing expression for microlayer formation is $\delta = C\sqrt{\nu t_g}$, which might be quite reasonable. This relation can be checked empirically and the important factor C can be determined.

2. The importance of microlayer evaporation as a heat transfer mechanism can be determined directly from the microlayer evaporation measurements for the case of higher heat fluxes if the nucleation site number densities are measured and if the measured bubble behavior can be assumed to be typical of every nucleation site.

3. A carefully controlled experiment in which measurements of microlayer formation and evaporation, bubble growth rates, and heat transfer data are obtained would provide a test case by which analytical models could be judged.

4. Measurements should be obtained for the important case of highly subcooled nucleate boiling in which steep temperature gradients exist in the liquid at the solid surface. This case is of particular practical interest such as in heat transfer in nuclear power plants. Very little recent work has been done for this case, and extensions of measurements such as those of Gunther and Kreith are needed.

REFERENCES

1. Bankoff, S. G., "A Note on Latent Heat Transport in Nucleate Boiling", AIChE J., 8, 63-65 (1962).
2. Bankoff, S. G. and Mason, J. P., "Heat Transfer from the Surface of a Steam Bubble in a Turbulent Subcooled Liquid Stream", AIChE J., 8, 30-33 (1962).
3. Bankoff, S. G. and Mikesell, R. D., "Bubble Growth Rates in Highly Subcooled Nucleate Boiling", Chem. Eng. Prog. Symp. Ser., 29, 95-102 (1959).
4. Cooper, M. G. and Lloyd, A. J. P., "Transient Local Heat Flux in Nucleate Boiling", Proc. Third International Heat Transfer Conference, III, 193-203 (1966).
5. Cooper, M. G. and Lloyd, A. J. P., "The Microlayer in Nucleate Pool Boiling", International J. of Heat and Mass Transfer, 12, 895-913 (1969).
6. Fath, H. S. and Judd, R. L., "Influence of System Pressure on Microlayer Evaporation Heat Transfer", J. Heat Transfer, 100, 49-55 (1978).
7. Foltz, G. E. and Mesler, R. B., "The Measurement of Surface Temperatures with Platinum Films During Nucleate Boiling of Water", AIChE J., 16, 44-48 (1970).
8. Gunther, F. C., "Photographic Study of Surface-Boiling Heat Transfer to Water with Forced Convection", Trans. ASME, 73, 115-123 (1951).

9. Gunther, F. C. and Kreith, F., "Photographic Study of Bubble Formation in Heat Transfer to Subcooled Water", Jet Propulsion Lab., Progress Report No. 4-120 (ORDCIT Project), March (1950).

10. Hecht, E. and Zajac, A., Optics, Addison-Wesley, Reading, Mass. (1974).

11. Hendricks, R. C. and Sharp, R. R., "Initiation of Cooling due to Bubble Growth on a Heating Surface", NASA TN D-2290 (1964).

12. Hospeti, N. B. and Mesler, R. B., "Deposits Formed Beneath Bubbles During Nucleate Boiling of Radioactive Calcium Sulfate Solutions", AIChE J., 11, 662-665 (1965).

13. Hospeti, N. B. and Mesler, R. B., "Vaporization at the Base of Bubbles of Different Shape During Nucleate Boiling of Water", AIChE J., 15, 214-219 (1969).

14. Jakob, M., Heat Transfer, Vol. 1, John Wiley and Sons, New York (1949).

15. Jawurek, H. H., "Simultaneous Determination of Microlayer Geometry and Bubble Growth in Nucleate Boiling", International J. of Heat and Mass Transfer, 12, 843-848 (1969).

16. Judd, R. L. and Hwang, K. S., "A Comprehensive Model for Nucleate Pool Boiling Heat Transfer Including Microlayer Evaporation", J. Heat Transfer, 98, 623-629 (1976).

17. Katto, Y. and Shoji, M., "Principal Mechanism of Micro-Liquid-Layer Formation on a Solid Surface with a Growing Bubble in Nucleate Boiling", International J. of Heat and Mass Transfer, 13, 1299-1311 (1970).

18. Katto, Y. and Yokoya, S., "Experimental Study of Nucleate Pool Boiling in Case of Making Interference Plate Approach to the Heating Surface", Proc. Third International Heat Transfer Conference, III, 219-227 (1966).

19. Mesler, R. B., "A Mechanism Supported by Extensive Experimental Evidence to Explain High Heat Fluxes Observed During Nucleate Boiling", AIChE J., 22, 246-252 (1976).

20. Moore, F. D. and Mesler, R. B., "The Measurement of Rapid Surface Temperature Fluctuations During Nucleate Boiling of Water", AIChE J., 7, 620-624 (1961).

21. Palmer, C. Harvey, Optics: Experiments and Demonstrations, The Johns Hopkins University Press (1962).

22. Plesset, M. S., "Note on the Flow of Vapor Between Liquid Surfaces", J. Chem. Phys., 20, 790-793 (1952).

23. Plesset, M. S. and Prosperetti, A., "The Contribution of Latent Heat Transport in Subcooled Nucleate Boiling", International J. of Heat and Mass Transfer, 21, 725-734 (1978).

24. Plesset, M. S. and Sadhal, S. S., "An Analytical Estimate of the Microlayer Thickness in Nucleate Boiling", J. Heat Transfer, 101, 180-182 (1979).

25. Rogers, T. F. and Mesler, R. B., "An Experimental Study of Surface Cooling by Bubbles During Nucleate Boiling of Water", Trans. AIChE, 10, 656-660 (1964).

26. Sharp, R. R., "The Nature of Liquid Film Evaporation During Nucleate Boiling", NASA TN D-1997 (1964).

27. Snyder, N. ~~R~~W. and Edwards, D. K., "Summary of Conference of Bubble Dynamics and Boiling Heat Transfer Held at the Jet Propulsion Laboratory", JPL Memo No. 20-137 (1956).

28. Tarnopol, M. S., "Treatment of Films with Liquid", U. S. Patent No. 2, 606, 566 (1952).

29. Voutsinos, C. M. and Judd, R. L., "Laser Interferometric Investigation of the Microlayer Evaporation Phenomenon", *J. Heat Transfer*, *97*, 88-92 (1975).

APPENDIX

Physical Property Values

The following physical property values for ethanol and water at saturation temperature at atmospheric pressure (liquid phase unless noted) are given for reference.

		Ethanol	Water
Saturation temperature	T_{sat}, ^{o}K	351.6	373.1
Density	ρ_L , kg/m^3	736.7	958.0
Vapor density	ρ_v , kg/m^3	1.593	0.598
Kinematic viscosity	ν , m^2/sec	0.6×10^{-6}	0.3×10^{-6}
Surface tension	σ , N/m	0.0175	0.0588
Thermal conductivity	k , $W/m\,^{o}K$	0.151	0.680
Thermal diffusivity	α , m^2/sec	6.83×10^{-8}	1.89×10^{-7}
Latent heat of vaporization	L , joules/kg	0.855×10^{6}	2.26×10^{6}
Index of refraction	n	1.336	1.318

The following physical property values for Pyrex Glass 7740 are given for reference.

Density	ρ , kg/m^3	2230
Thermal conductivity	k , $W/m\,^{o}K$	1.172 @ $351.6^{o}K$
		1.202 @ $373.1^{o}K$
Thermal diffusivity	α , m^2/sec	0.64×10^{-6} @ $351.6^{o}K$
		0.63×10^{-6} @ $373.1^{o}K$
Index of refraction	n	1.474

References for property values

International Critical Tables, ed. National Research Council, McGraw-Hill, New York (1926-1930).

Handbook of Chemistry and Physics, 47th ed., Chemical Rubber Co., Cleveland, Ohio (1966).

Thermophysical Properties of Matter, Thermophysical Properties Research Center (TPRC), Purdue Univ., IFI/Plenum, New York (1970).

American Institute of Physics Handbook (1972).

Handbook of Heat Transfer, ed. Rohsenow and Hartnett, McGraw-Hill, New York (1973).

Specification sheet from Pyrex Glass (1977).

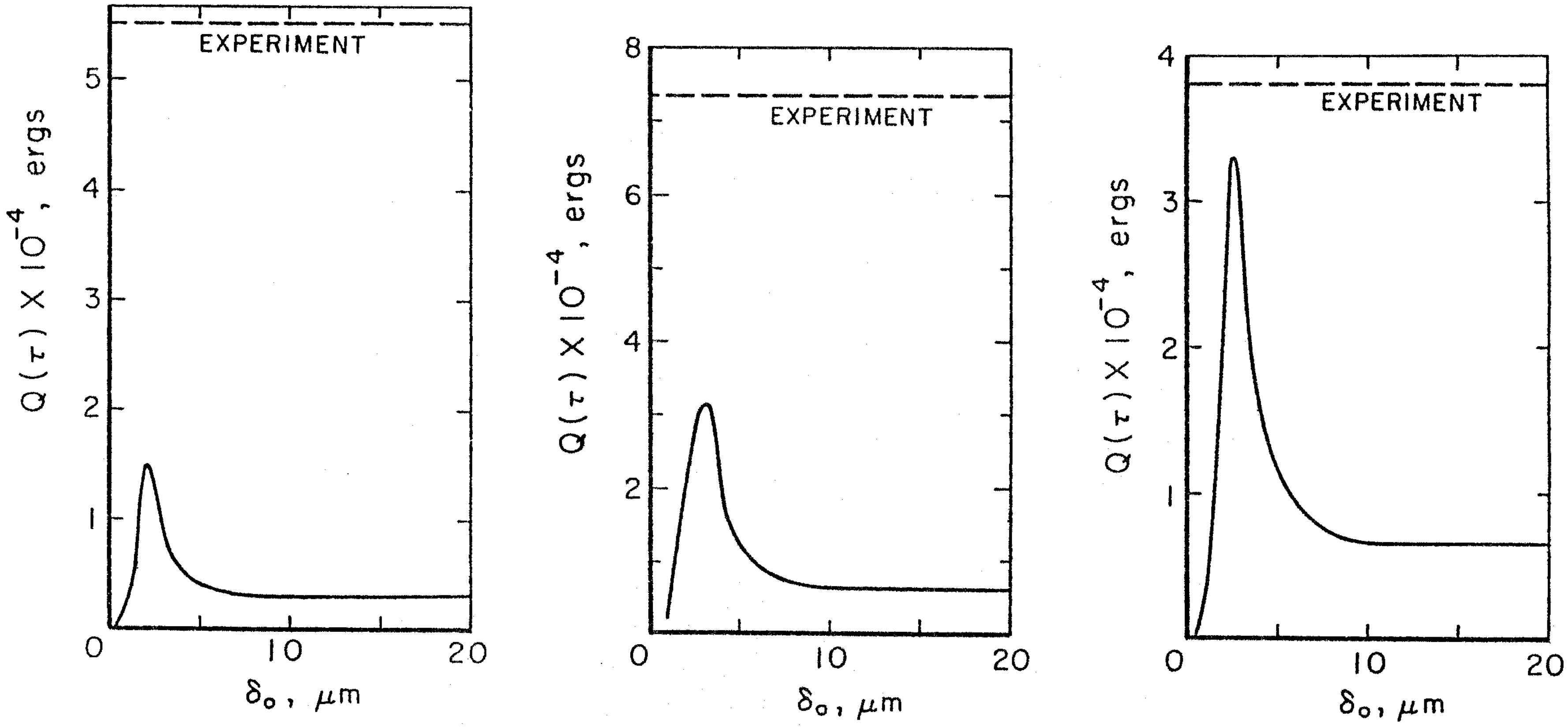

Figure 1. The calculated total heat, $Q(\tau)$, extracted from the microlayer is shown as a function of the mean initial thickness, δ_o, of the microlayer. The calculations are based on experimental data for highly subcooled nucleate boiling of water at atmospheric pressure in which bubbles grow to maximum diameters less than 1 mm with lifetimes less than 0.5 msec. The horizontal line is the experimental value of the heat transport per bubble. For details, see Plesset and Prosperetti [23].

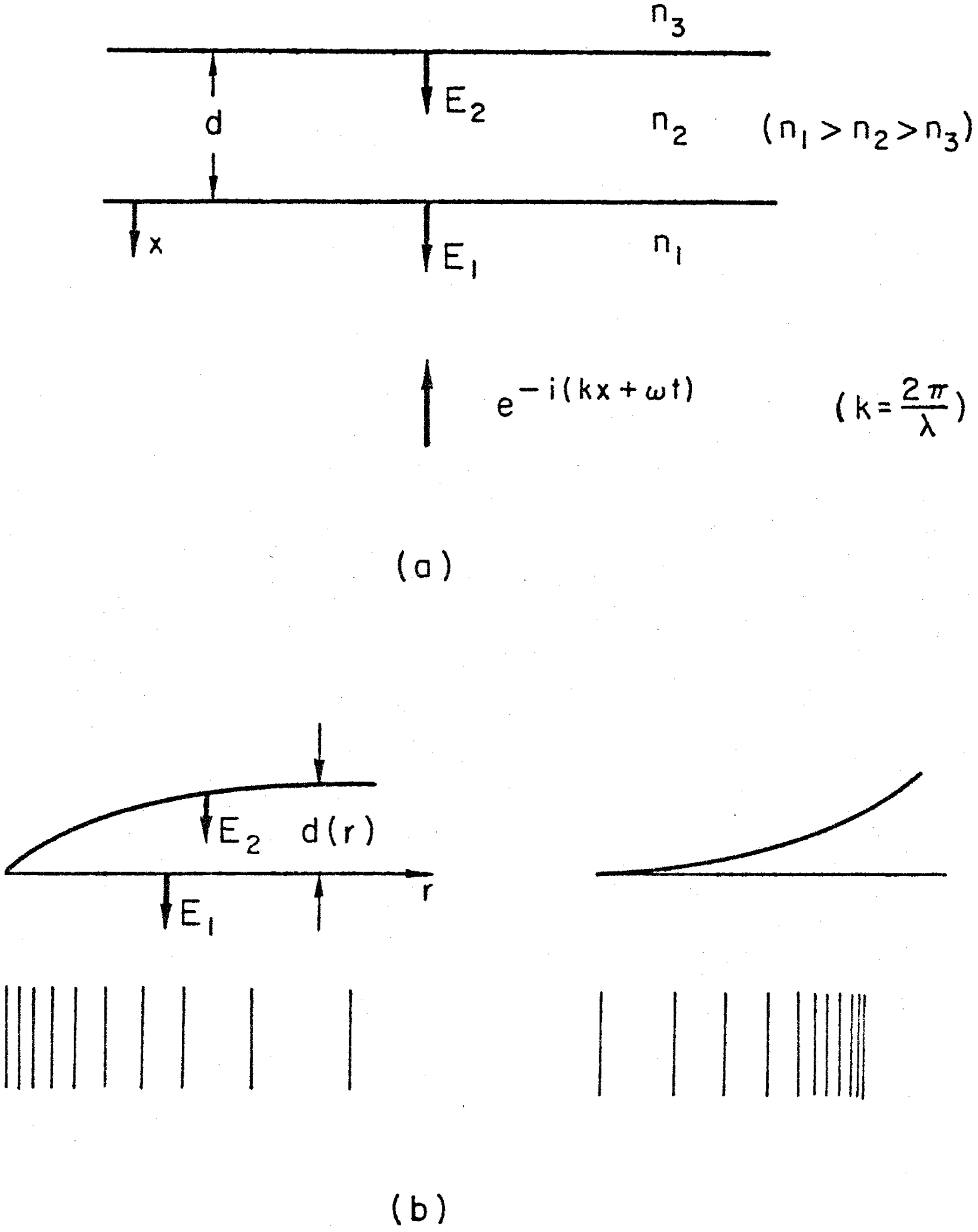

Figure 2. (a) Schematic of the reflections of an incident plane wave from the interfaces bounding a layer of thickness d and index of refraction n_2.
(b) Schematic of the fringe patterns which result when the thickness of the layer varies.

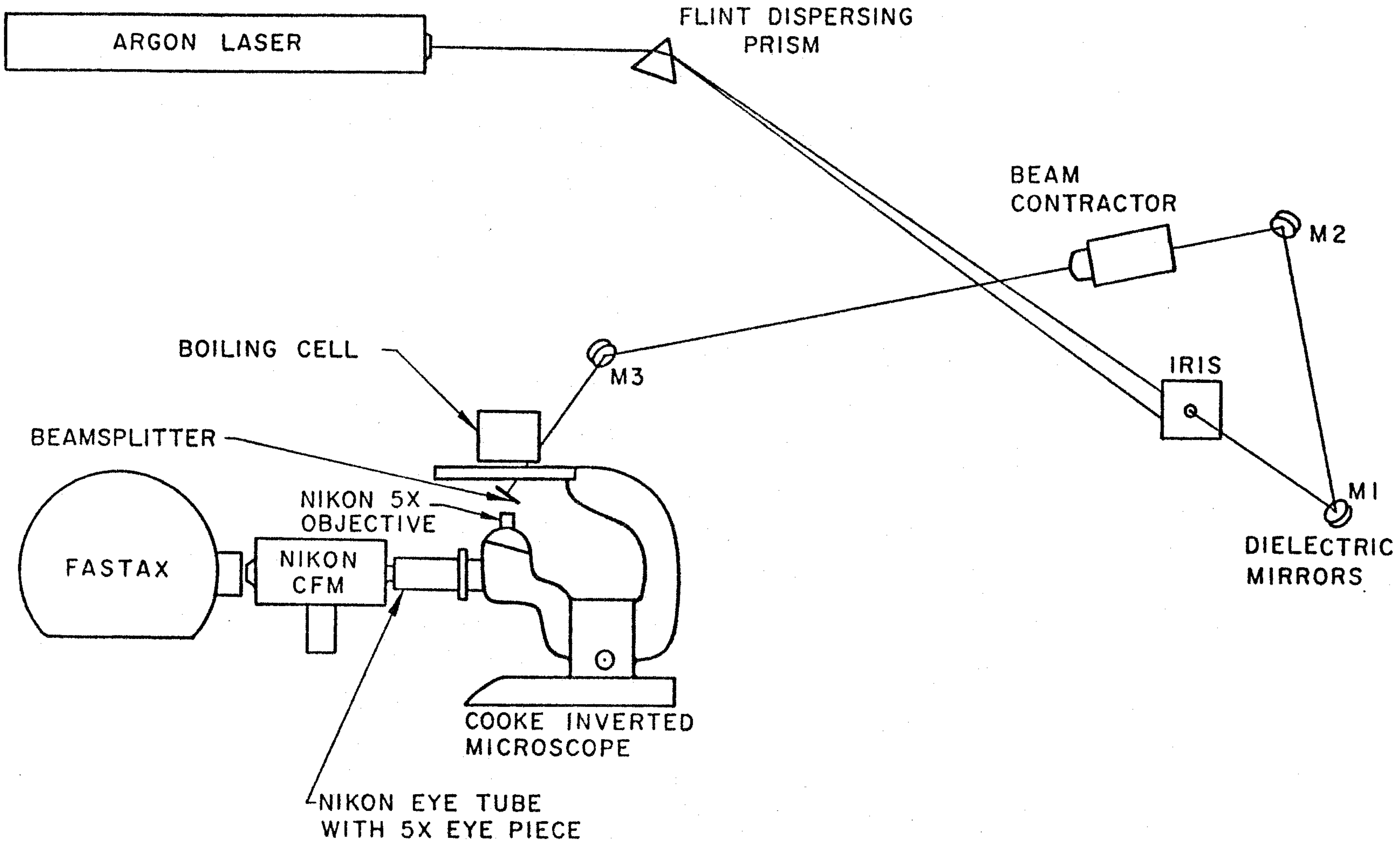

Figure 4. Schematic of the laser interferometric - high speed camera system

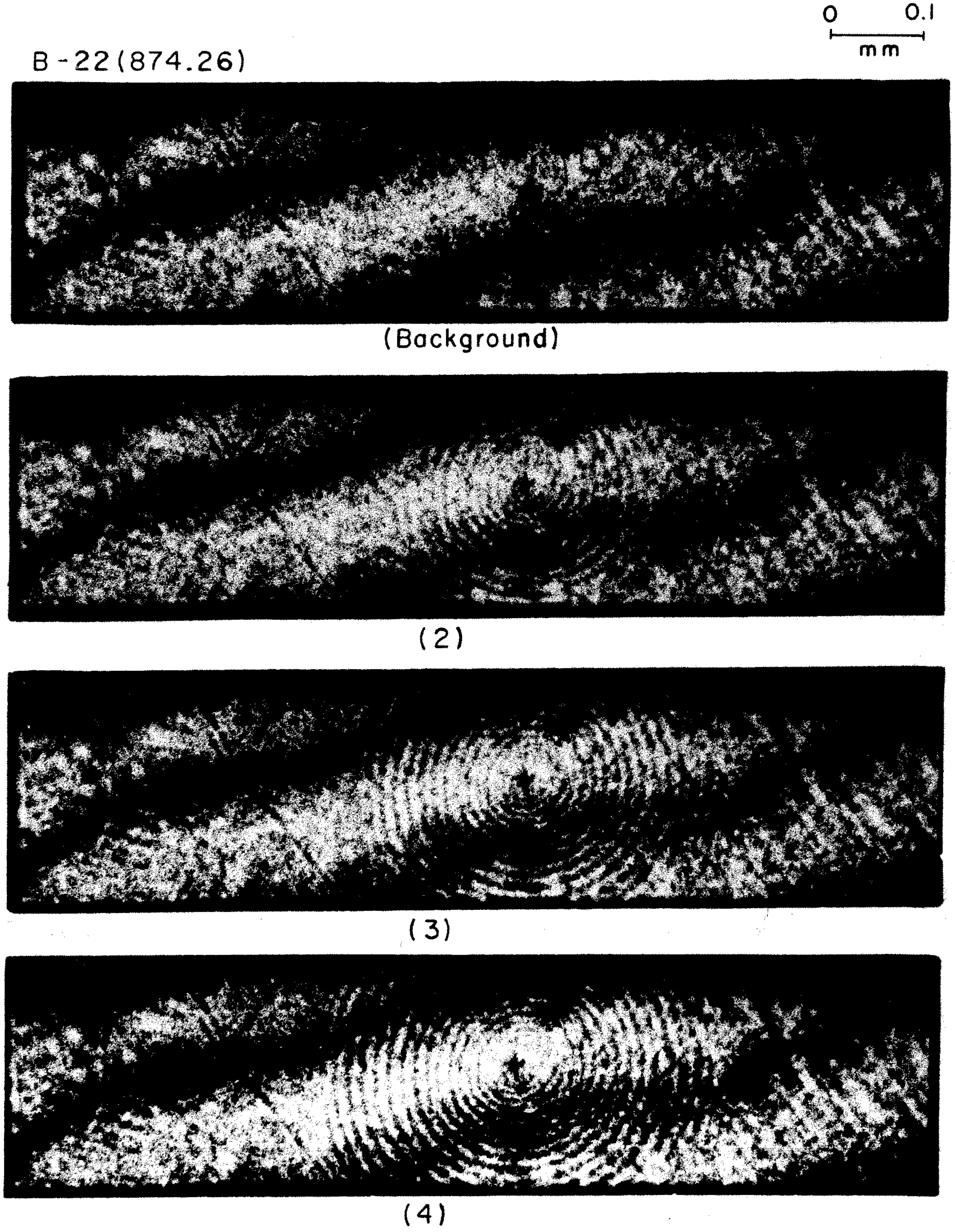

Figure 5. Fringe patterns for bubble growth sequence in ethanol at atmospheric pressure with a mean heat flux of 26.5 kW/m^2 and a subcooling of 5.7°C. The frames shown are numbered from the first frame in which the bubble appears; the framing rate is 14.87 frames/msec (0.0672 msec between frames).

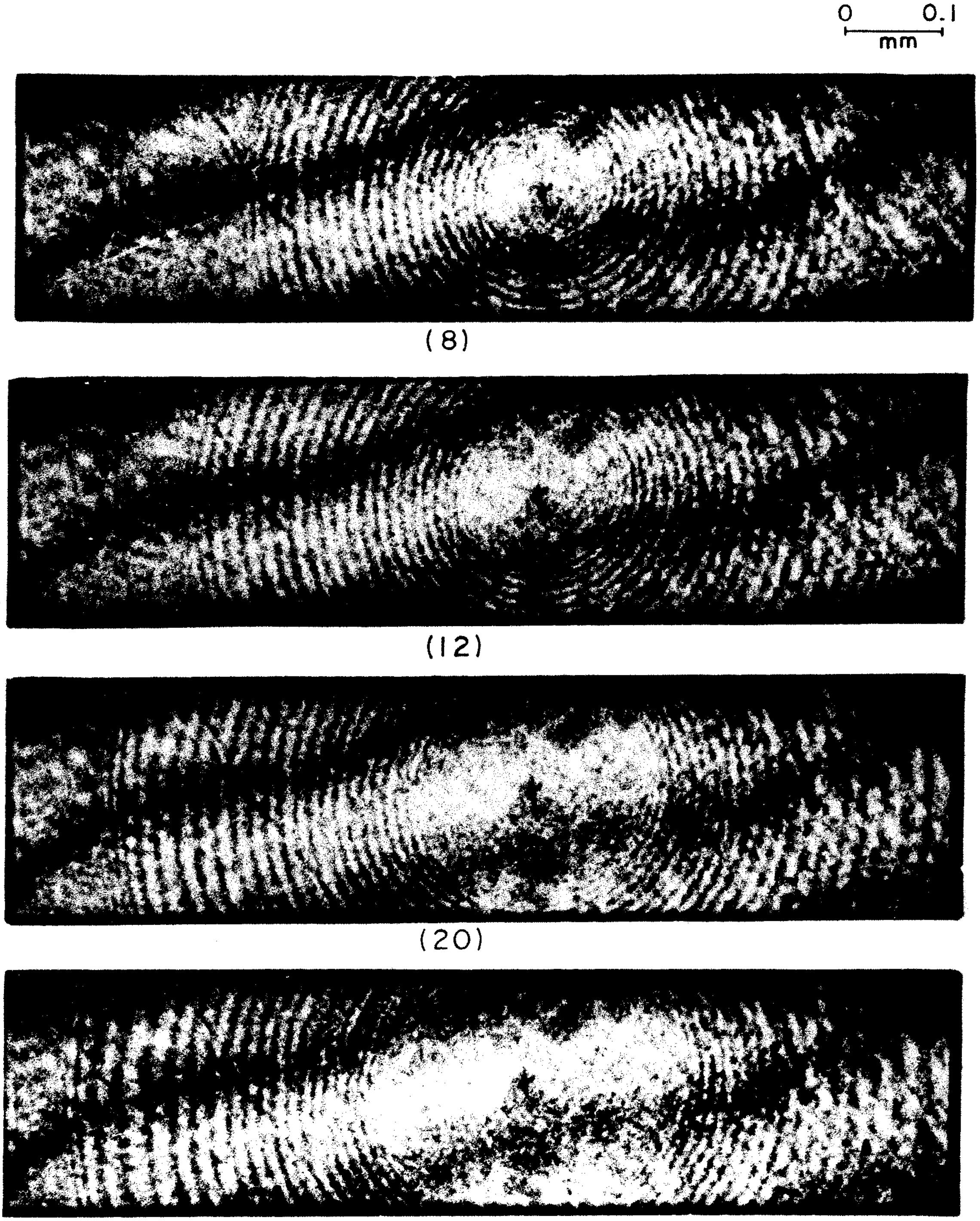

(8)

(12)

(20)

(28)

Figure 5. (Continued)

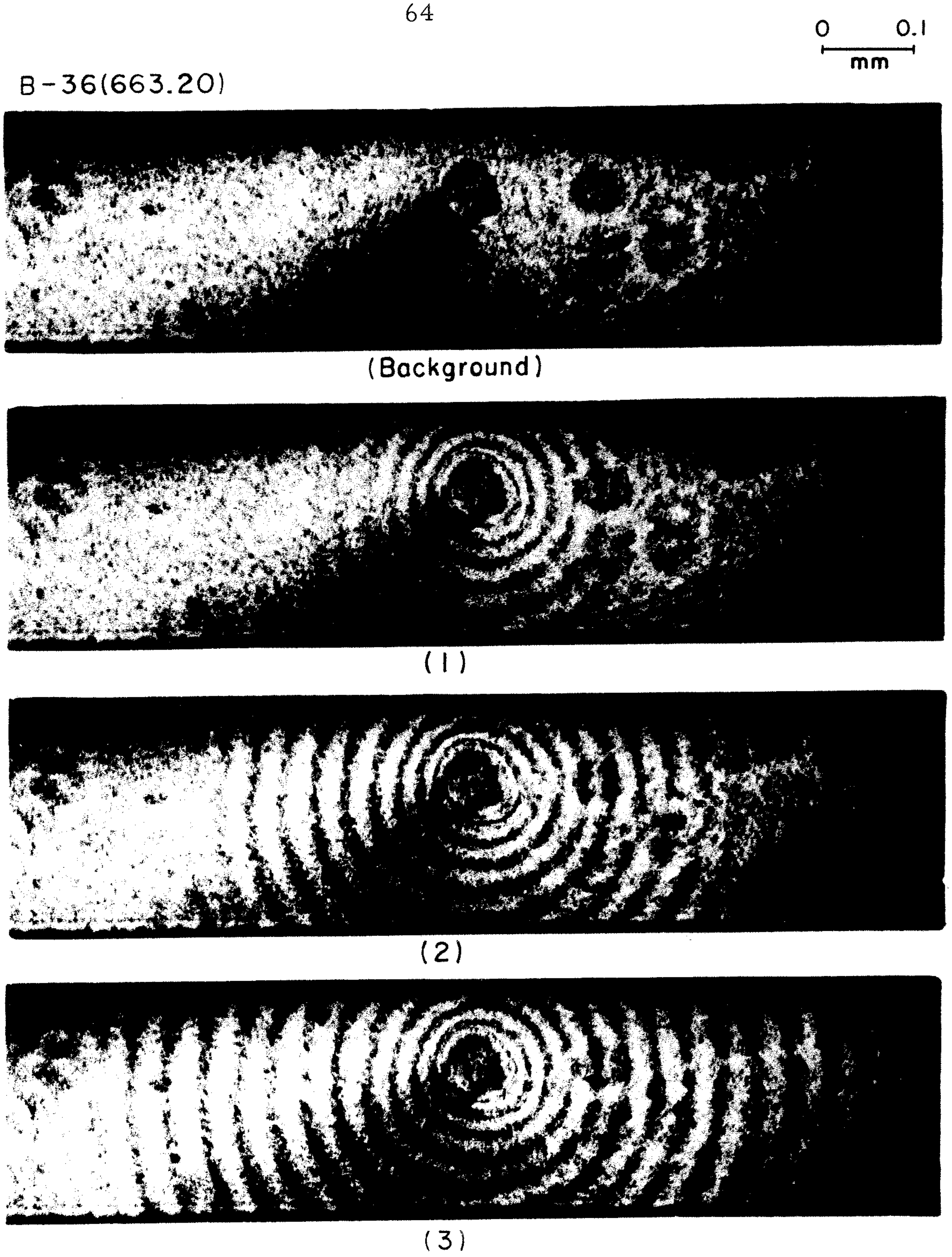

Figure 6. Fringe patterns for bubble growth sequence in water at atmospheric pressure with a mean flux of 204 kW/m^2 and a subcooling of 21.7°C. The frames shown are numbered from the first frame in which the bubble appears; the framing rate is 15.25 frames/msec (0.0656 msec between frames).

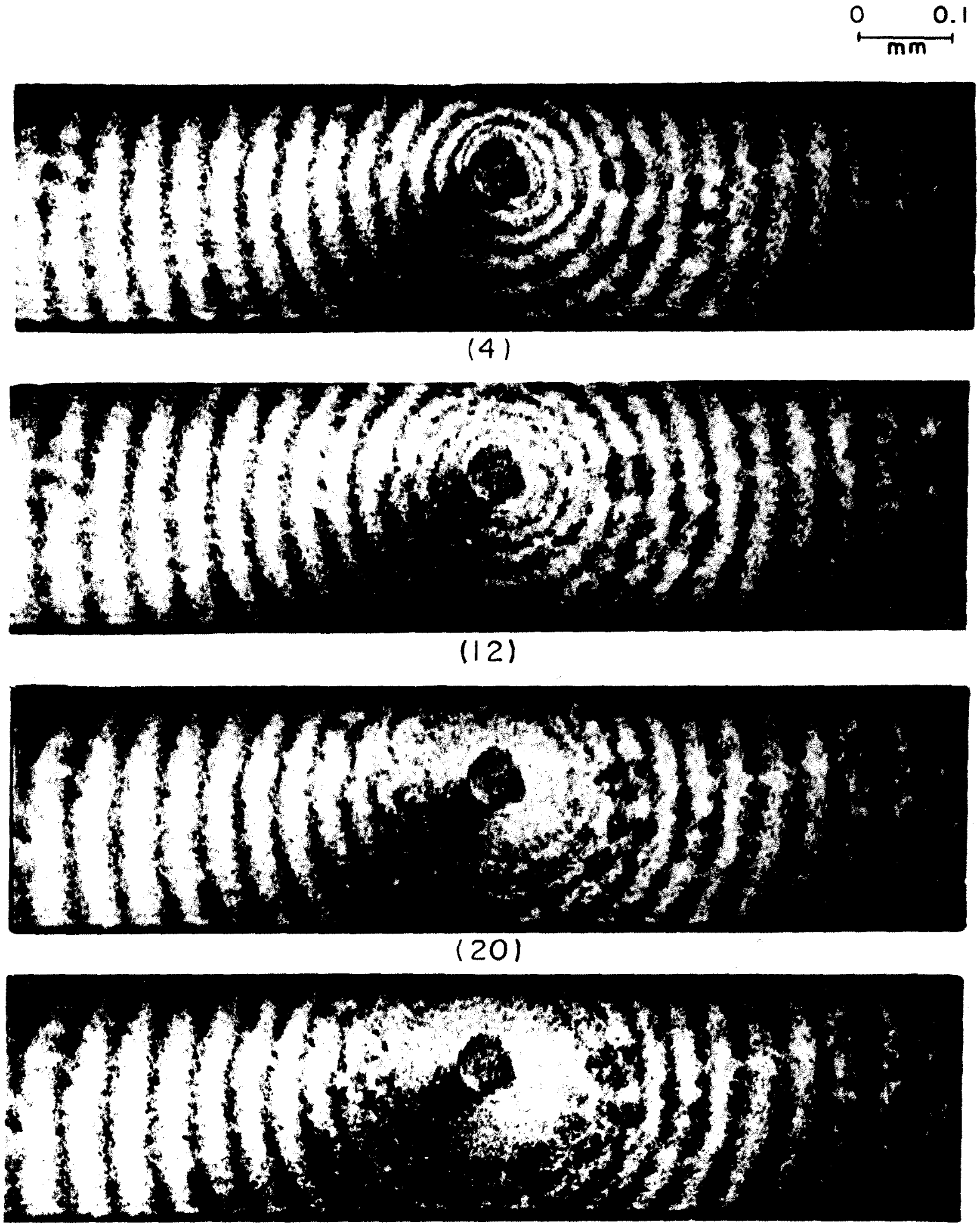

(4)

(12)

(20)

(28)

Figure 6. (Continued)

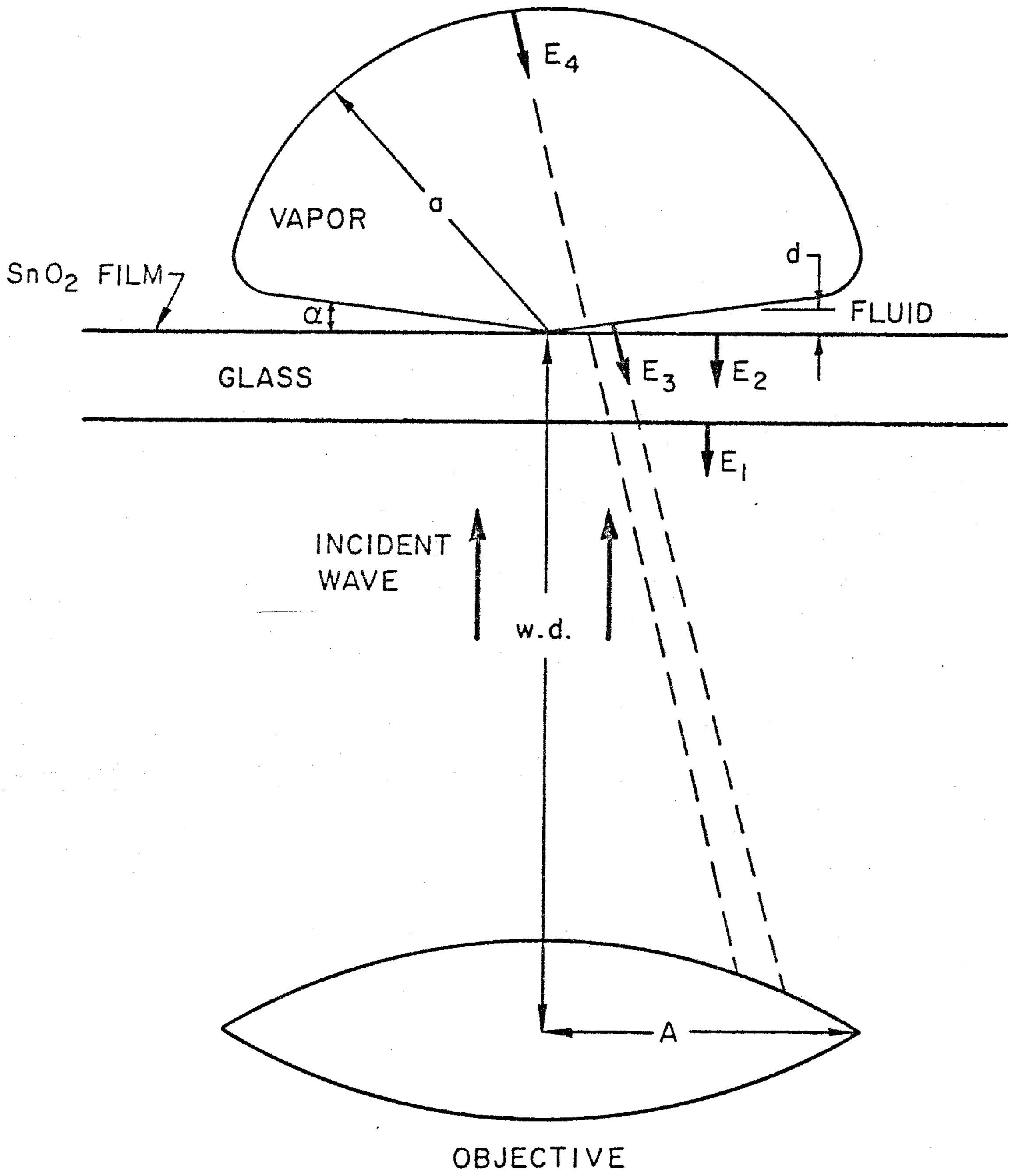

Figure 7. Idealized model of a vapor bubble on a glass plate.

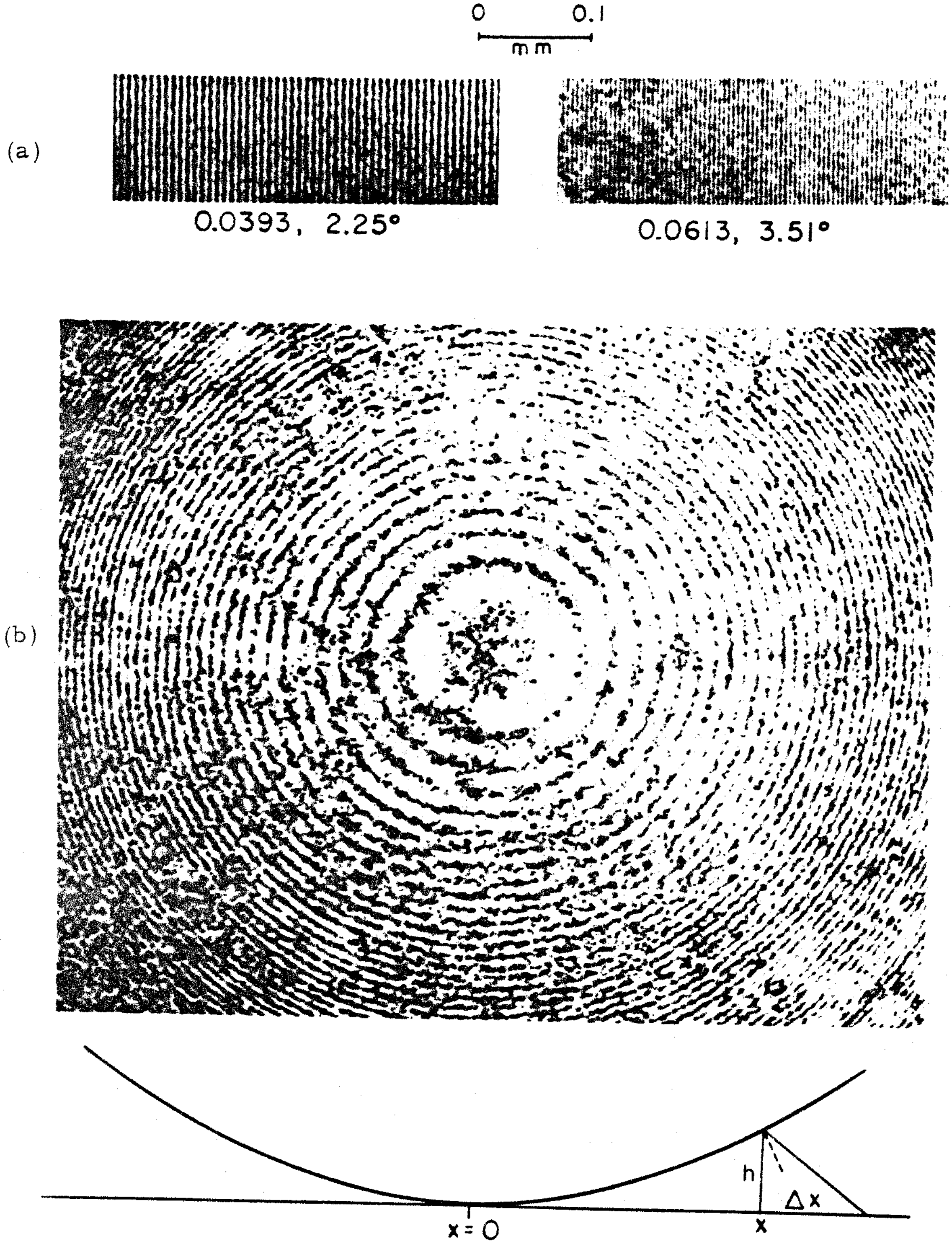

Figure 8. Examples of the fringe patterns in the calibration pictures for (a) wedges with slopes and wedge angles as shown and (b) a 20.6 mm diameter steel ball on a glass plate. Scale shown applies to all three pictures.

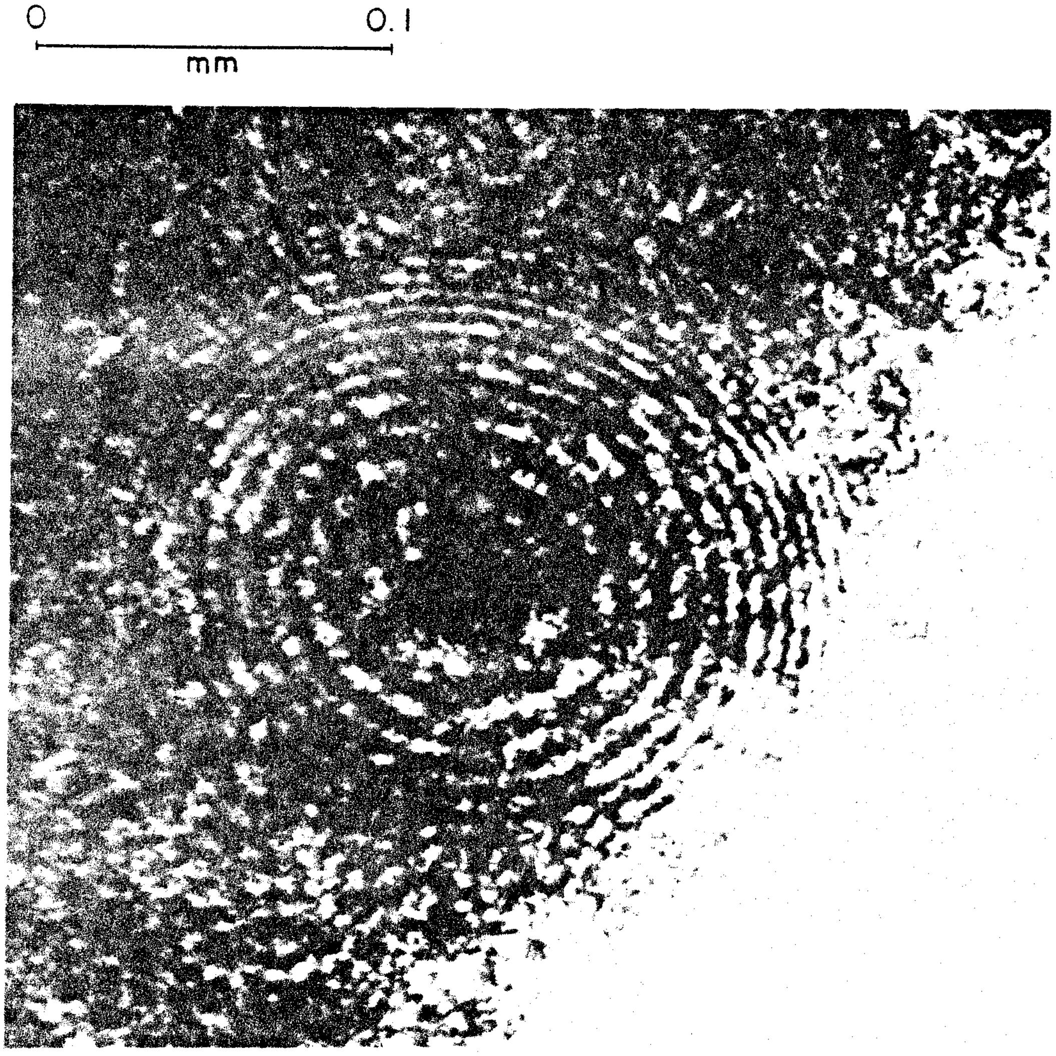

Figure 9. Fringe pattern resulting from the reflection from the top of a CO_2 bubble estimated to be about 3 mm in diameter.

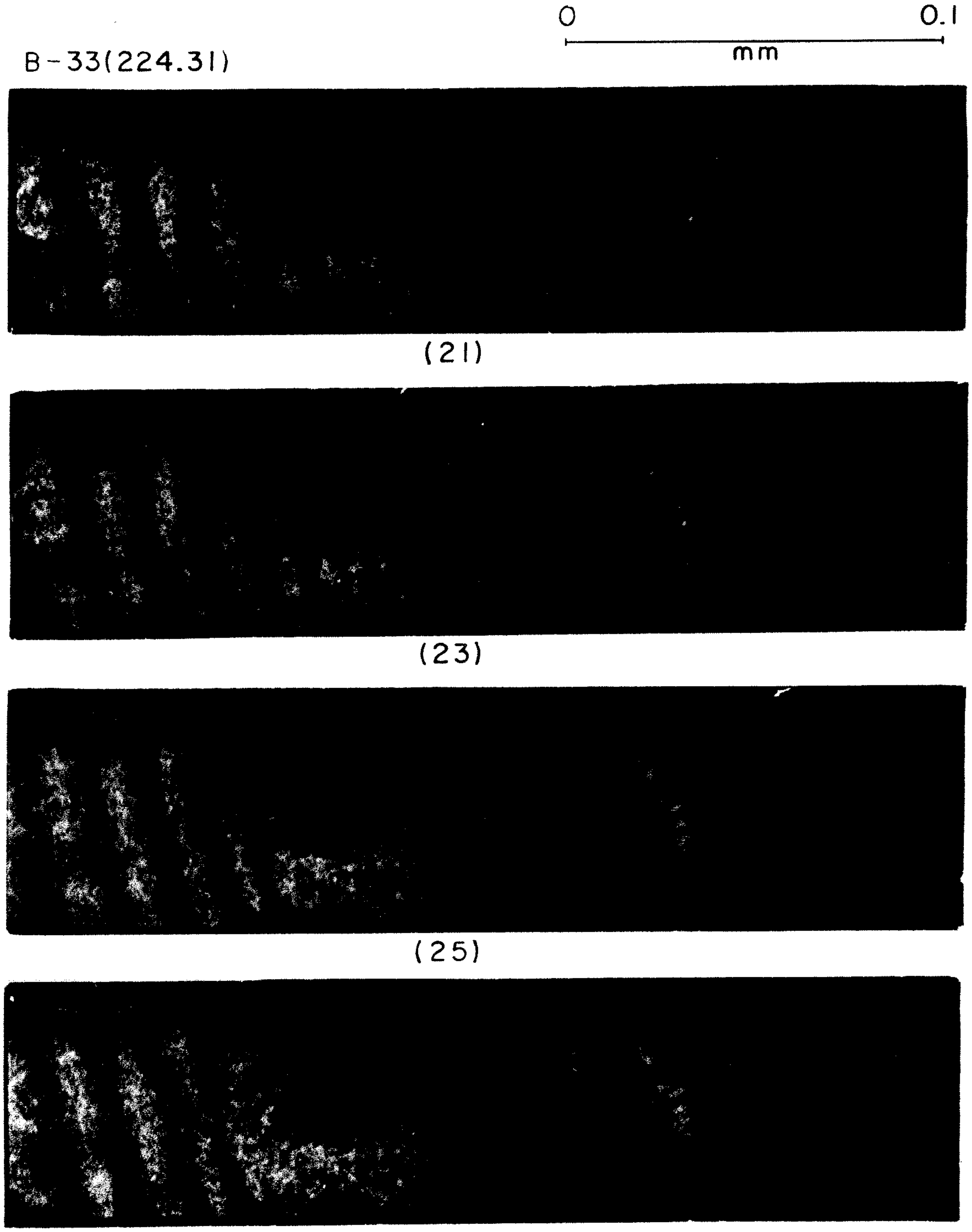

(21)

(23)

(25)

(27)

Figure 10. Fringe patterns from the microlayer contact region as the dry spot for an ethanol vapor bubble grows across the film frame. The frames shown are numbered from the first frame in which the bubble appears; the framing rate is 13.56 frames/msec (0.0737 msec between frames).

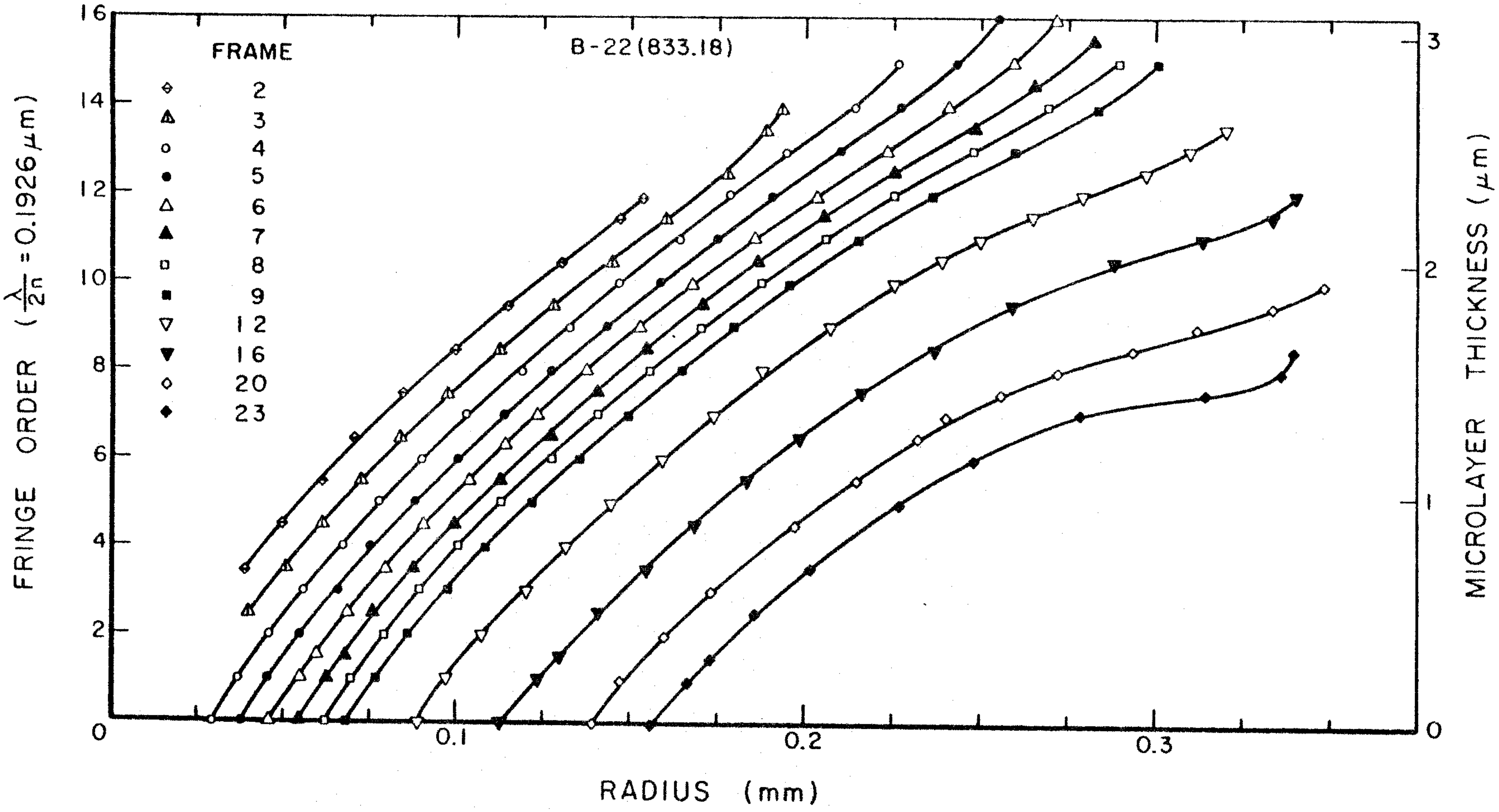

Figure 11. Microlayer profiles for an ethanol vapor bubble at atmospheric pressure with a mean heat flux of 26.5 kW/m^2 and a subcooling of 5.7°C. The frames shown are numbered from the first frame in which the bubble appears; the framing rate is 13.99 frames/msec (0.0715 msec between frames).

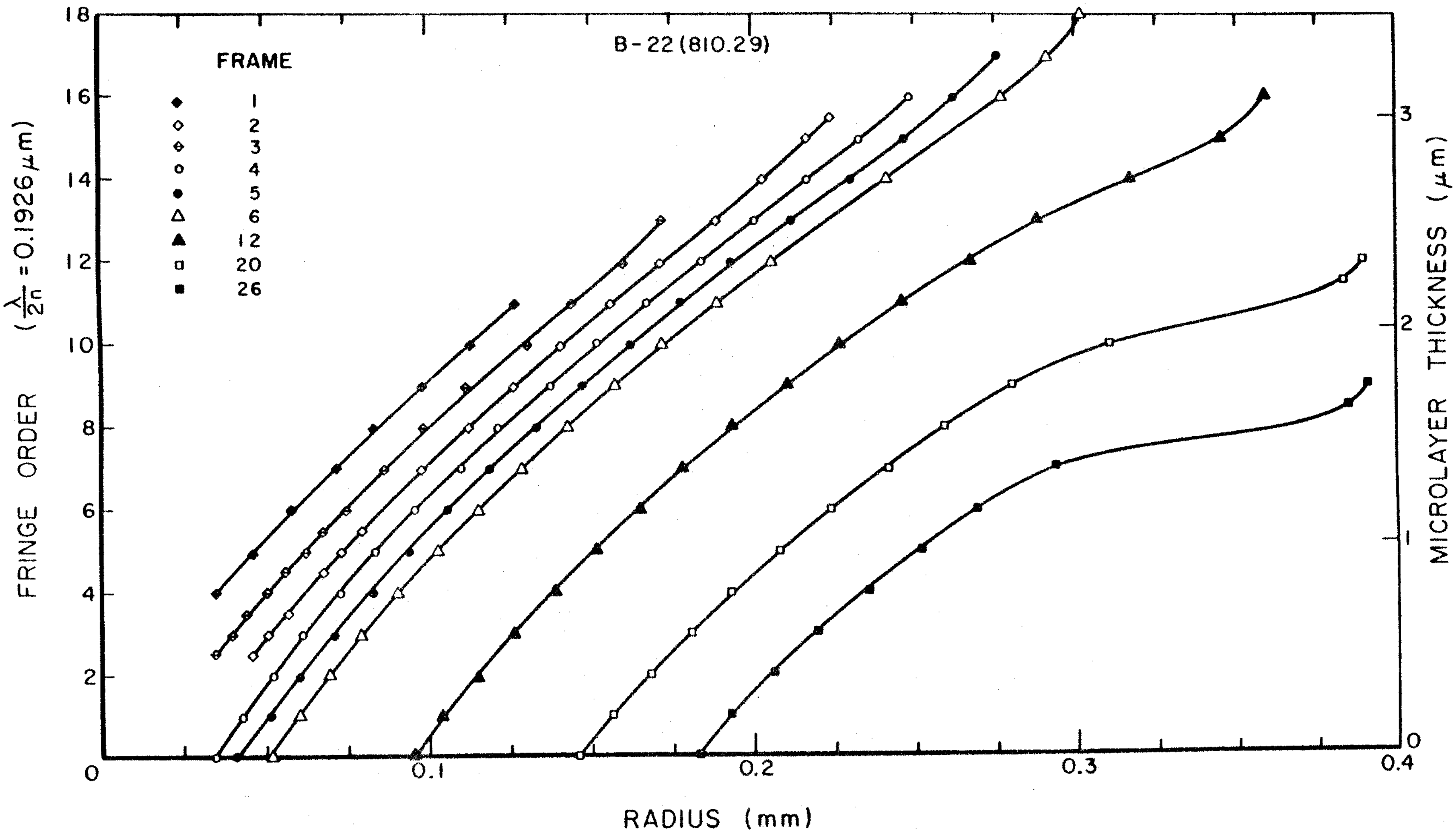

Figure 12. Microlayer profiles for an ethanol vapor bubble at atmospheric pressure with a mean heat flux of 26.5 kW/m^2 and a subcooling of 5.7°C. The frames shown are numbered from the first frame in which the bubble appears; the framing rate is 13.23 frames/msec (0.0756 msec between frames).

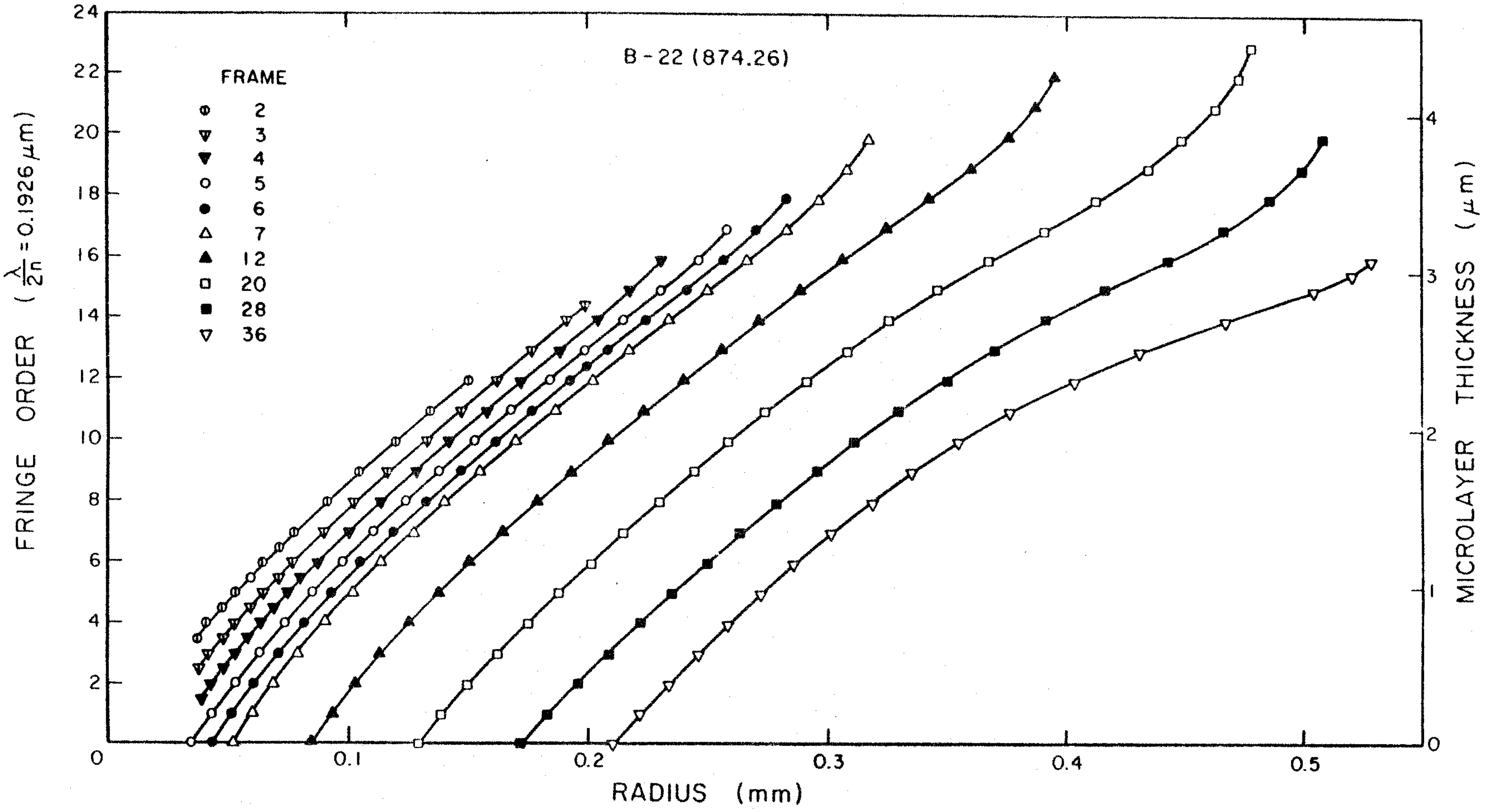

Figure 13. Microlayer profiles for an ethanol vapor bubble at atmospheric pressure with a mean heat flux of 26.5 kW/m^2 and a subcooling of 5.7°C. The frames shown are numbered from the first frame in which the bubble appears; the framing rate is 14.87 frames/msec (0.0672 msec between frames).

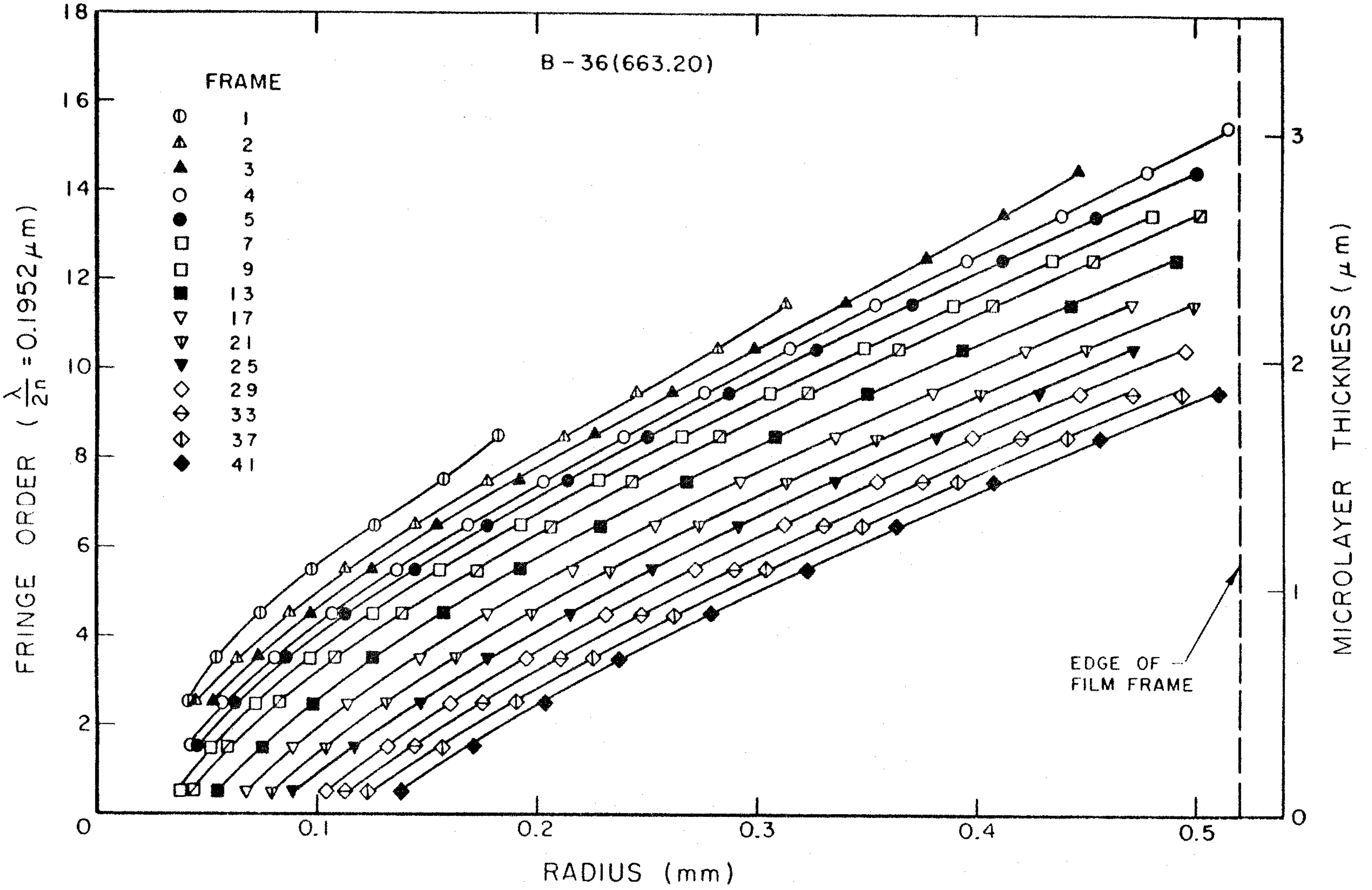

Figure 14. Microlayer profiles for a water vapor bubble at atmospheric pressure with a mean heat flux of 204 kW/m^2 and a subcooling of 21.7°C. The frames shown are numbered from the first frame in which the bubble appears; the framing rate is 15.25 frames/msec (0.0656 msec between frames).

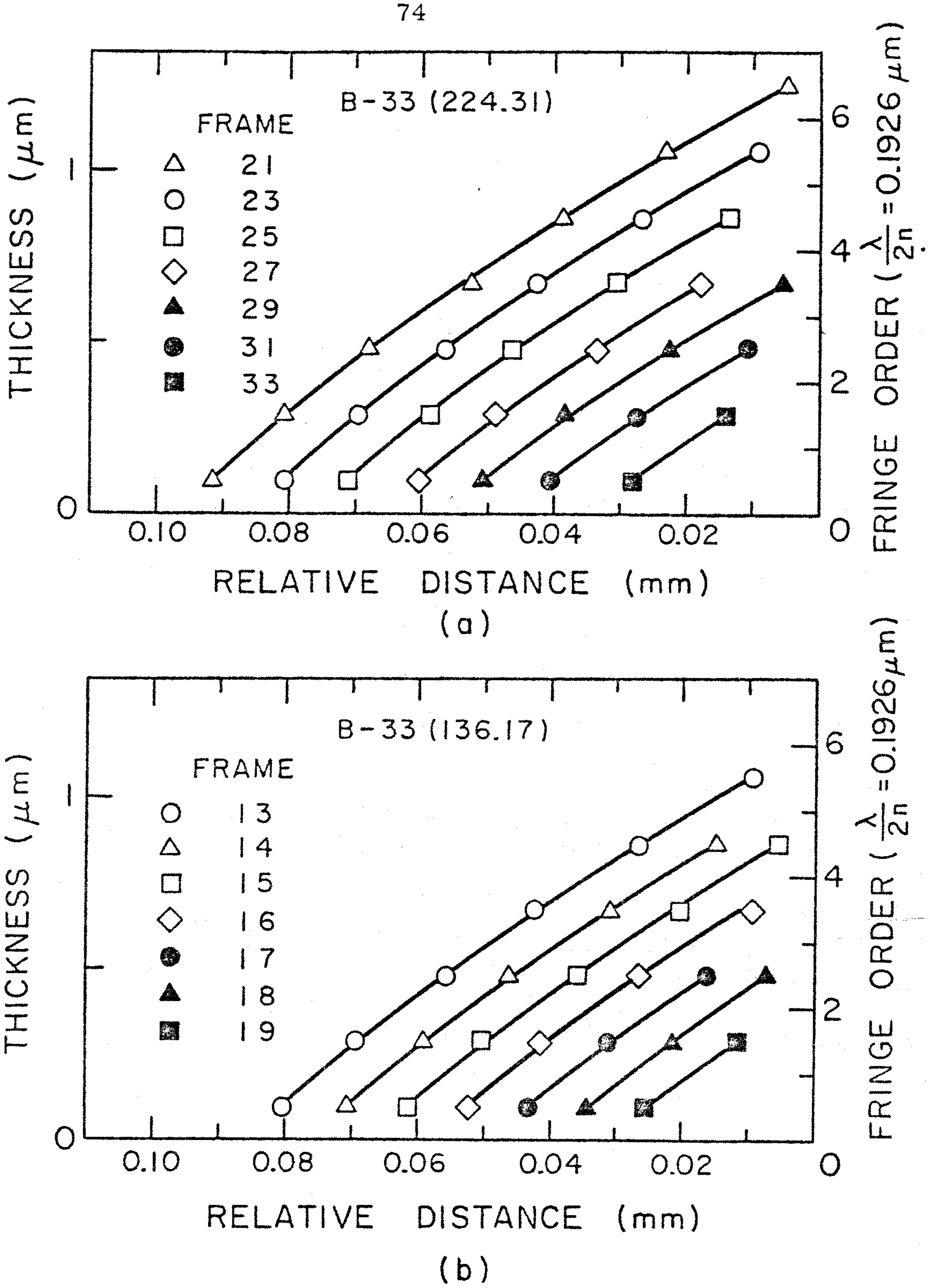

Figure 15. Microlayer profiles of the contact region as the dry spot for an ethanol vapor bubble grows across the film frame. The frames shown are numbered from the first frame in which the bubble appears; the framing rates are (a) 7.66 frames/msec (0.131 msec between frames) and (b) 13.56 frames/msec (0.0737 msec between frames).

PART II

AN INVESTIGATION OF THE THEORY OF EVAPORATION AND CONDENSATION

LIST OF SYMBOLS

C = $\sqrt{\frac{8RT}{\pi}}$ = mean molecular speed

c_p = specific heat at constant pressure

c_v = specific heat at constant volume

$f(\underset{\sim}{r}, \underset{\sim}{\xi}, t)$ = velocity distribution function

Kn = Knudsen number = $\frac{\lambda}{\ell}$

k = thermal conductivity

L = latent heat of vaporization

ℓ = length between the two liquid surfaces

M = Mach number = $\frac{u}{\sqrt{\gamma RT}}$

N_i = first order term of parametric "number density" function ($i = 1, 2$)

n = number density

n_i = parametric "number density" function ($i = 1, 2$)

$\underset{\sim}{P}$ = stress tensor

p = pressure

p^e = equilibrium vapor pressure

Q = arbitrary function of particle velocity

ΔQ = collision integral

$\underset{\sim}{q}$ = heat flux vector

R = gas constant of vapor

$\underset{\sim}{r}$ = position vector

T = absolute temperature of vapor

T_i = parametric "temperature" function ($i = 1, 2$)

T_L = absolute temperature of liquid

t = time

t_i = first order term of parametric "temperature" function ($i = 1, 2$)

$\underset{\sim}{U}$ = mean velocity

u = one-dimensional mean velocity

u_c = first order term of velocity

u_i = parametric "velocity" function ($i = 1, 2$)

v_i = first order term of parametric "velocity" function ($i = 1, 2$)

w = net mass flux

w_+ = maximum rate of evaporation

α = evaporation coefficient

β = $\frac{\Delta \nu}{\Delta \theta}$ = latent heat parameter

β_i = $2RT_i$ ($i = 1, 2$)

Γ = Schrage's correction factor (see p. 91)

δ = $\frac{k}{\rho u c_p}$

ϵ = small parameter

η = $\epsilon \bar{x}$ = outer variable

$\Delta\theta$ = $\frac{T_I - T_{II}}{\epsilon T_{II}}$

λ = mean free path

μ = viscosity

$\Delta\nu = \dfrac{n^e_I - n^e_{II}}{\epsilon n^e_{II}}$

$\underset{\sim}{\xi}$ = particle velocity

ρ = density of vapor

ρ^e = equilibrium vapor density

Superscripts

(1)	first order quantity

Subscripts

1, 2	refer to + and - velocity directions respectively
I, II	refer to cold and hot interfaces respectively
+, -	refer to sums and differences respectively (e.g. $t_{\pm} = t_1 \pm t_2$)
0	refers to reference values for nondimensionalization

I. INTRODUCTION

The problems of evaporation and condensation at a liquid-vapor interface are of fundamental interest in science and engineering. Despite the widespread occurrence of such phase change processes, a satisfactory physical description of evaporation and condensation is still not available. Considering the description of these processes as a fundamental problem in physics, we would like to have a continuum relation for the net mass flux at a liquid-vapor interface for given conditions. Such an expression would greatly aid analysis of many current problems involving liquid-vapor phase changes. Of particular interest in the present investigation is an analysis for determination of the role of microlayer evaporation in the heat transfer in nucleate boiling. Such analysis depends strongly on the continuum relation used to determine the net mass flux at an interface. Because of recent controversy regarding the correct expression for net mass flux, we have endeavored to evaluate the current theory of evaporation and condensation.

The traditional treatment of evaporation and condensation has been to use the approach of kinetic theory. Recent investigators have followed this approach, attempting a more refined solution by obtaining approximate solutions to the Maxwell-Boltzmann transport equation by different methods. Due to the complexities involved in obtaining such solutions, simplified problems are posed. Four such problems restricted to a pure vapor phase are treated in the literature:

1. The steady plane two-interface problem.

Net evaporation at a hot surface and net condensation at a cold surface result in a steady flow of vapor.

2. The steady plane single interface problem.

A uniform vapor flow at infinity occurs with either net evaporation from a hot surface or net condensation on a cold surface.

3. The unsteady plane single interface problem.

A liquid is initially in equilibrium with the semi-infinite vapor above it. At $t = 0$ the liquid temperature is given a step change and held fixed subsequently while the vapor field changes with time.

4. The steady spherical droplet in infinite vapor.

A steady vapor flow occurs between a droplet at a fixed temperature differing from that of a uniform vapor at infinity.

The purpose of this study is to take a critical look at the current theory with a particular viewpoint towards the continuum regime. The foundations of the current theory are briefly reviewed in Chapter II. We have chosen to use the Maxwell moment method as developed by Lees, and a description of the method is presented in Chapter III. We have concentrated on the steady plane two-interface problem. This problem is treated in Chapter IV using (i) the continuum equations with the generally used mass flux relations, (ii) the linearized moment equations and (iii) the nonlinear moment equations. In Chapter V we consider the work in the literature on the different problems stated above and try to relate these to one another and to our findings.

We have found both in our work and in the literature that Schrage's correction to the Hertz-Knudsen formula for mass flux as applied to continuum problems seems reasonable when the usual boundary conditions are assumed. The difference between recent results and Schrage's result is the adjustment of a numerical factor, which multiplies the vapor flux, from Schrage's value of 2 to a somewhat lower value. However, the detail in the behavior of the physical variables available from the more refined solutions has revealed some difficulties which become evident in the steady plane two-interface problem. For most liquids, the solution indicates that the temperature profile is inverted from what would seem physically reasonable. That is, the vapor just outside the cold liquid surface may be hotter than the temperature of the hot liquid, and the vapor just outside the hot liquid surface may be colder than the cold liquid. These temperatures at the boundaries constitute the boundary conditions for the continuum temperature field. Also, some investigators have found continuum mass fluxes greater than free molecular mass fluxes for the same boundary conditions. It would seem that the effect of collisions in the continuum regime would be to reduce the net mass flux from the free molecular value rather than increase it. We have taken the position that these effects are physically incorrect. Hence, we have sought to determine what is wrong with the theory.

We first considered whether the problem as posed has been solved correctly. We have considered the consistency of the linearized solutions, the effect of nonlinearities, and the validity of the methods in approaching the continuum limit. Our results indicate that the problems as posed have been solved correctly. We thus considered whether the problem is <u>physically</u> well posed since our objections are to the physical solution. In this regard, two likely questions are (i) whether the steady problem with fixed surface temperatures is well posed and (ii) whether the boundary conditions are correctly posed. The steady problem does seem to be well posed. Therefore, we conclude that the boundary conditions are probably incorrect. In this study, we have not attempted an extensive literature survey of the experimental support of the presently assumed boundary conditions. However, we are not aware of any strong support for these boundary conditions. Rather, because of the difficulties in performing critical experiments, it seems that a jump to the presently assumed boundary conditions was made on the basis of relatively few good experiments. These boundary conditions have been retained because there has been no explicit reason to question them. We believe that we present here a basis for questioning these boundary conditions. The implications of our conclusion are clear: if the questions we have raised cannot be satisfactorily resolved, then a return to a more fundamental level is necessary. Very probably, the difficulties can only be resolved by critical experiments.

II. THE USUAL TREATMENT OF EVAPORATION AND CONDENSATION

In this chapter, we first consider some fundamental concepts in kinetic theory. Only those fundamentals relevant to the problem at hand are reviewed. The boundary conditions at a liquid-vapor interface are then briefly discussed, and the boundary conditions presently used in all kinetic theory treatments of evaporation and condensation are established. The theories of Hertz-Knudsen and Schrage based on equilibrium kinetic theory are then developed.

2.1 Some concepts and definitions from kinetic theory

In kinetic theory a gas is treated as a system of point particles which obey the laws of classical mechanics. For particles of identical mass, the dynamical state of a single particle at an instant of time t is given by specifying the position $\underset{\sim}{r}$ and the velocity $\underset{\sim}{\xi}$ of the particle. Because of the large number of particles involved, a statistical formulation can be used to determine the mean quantities of interest. We thus introduce a probability density function or velocity distribution function to characterize the state of the system of particles. Within a volume element $d\underset{\sim}{r}$ around the position $\underset{\sim}{r}$ at an instant of time t there are a large number of particles each of which can have any velocity. Within this volume, the actual number of particles within a given element of velocity space $d\underset{\sim}{\xi}$ is given by the velocity distribution function $f(\underset{\sim}{r}, \underset{\sim}{\xi}, t)$ as $dn = f(\underset{\sim}{r}, \underset{\sim}{\xi}, t)d\underset{\sim}{r}\ d\underset{\sim}{\xi}$. Integration over all of velocity space gives the total number of particles in the volume which

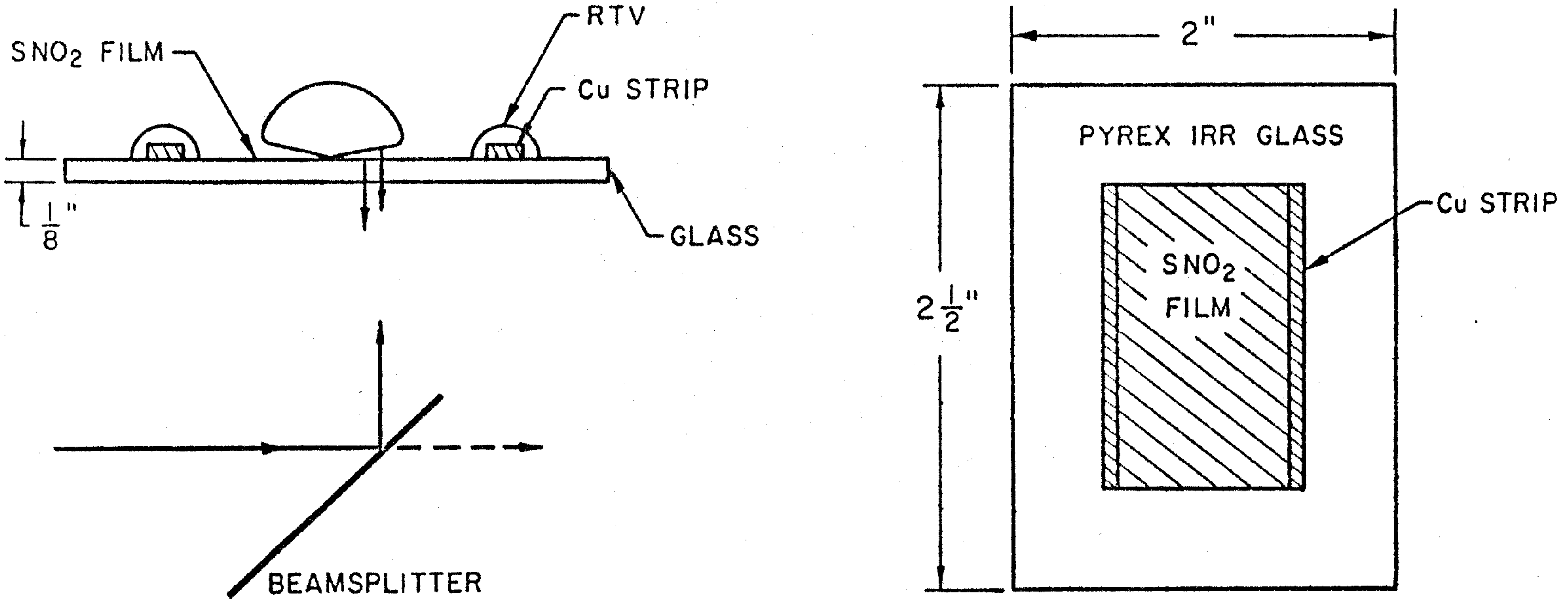

Figure 3. Schematic of the glass boiling surface.

is just the number density when divided by suitably small $d\underset{\sim}{r}$. Hence for particles of mass m, the density is by definition

$$\rho(\underset{\sim}{r}, t) = m \int f(\underset{\sim}{r}, \underset{\sim}{\xi}, t) d\underset{\sim}{\xi} = mn(\underset{\sim}{r}, t) \quad . \tag{2.1}$$

In a similar manner, other additive molecular properties can be defined as given in Appendix A. We note here that for the point particles considered, the definitions of pressure, density and temperature are related by the perfect gas law.

For a system in equilibrium, the velocity distribution function is known as the Maxwell distribution function or simply as a Maxwellian. In the general case, the equilibrium can be relative to a uniform velocity $\underset{\sim}{U}$ (the uniform gas) in which case the "Maxwellian translating with velocity $\underset{\sim}{U}$" is given by

$$f = \frac{n}{(2\pi RT)^{3/2}} e^{\frac{-(\underset{\sim}{\xi} - \underset{\sim}{U})^2}{2RT}} \quad . \tag{2.2}$$

Physical processes in which tranport of mass, momentum or energy occurs take place in systems which are not in overall equilibrium. In this case, the velocity distribution function is not described by a single Maxwellian. However in many continuum processes, the local departure from a Maxwellian is small. Much of the physical behavior can then be determined by supposing that the molecules are distributed locally (over a few mean free paths) according to a Maxwellian and then allowing the number density and temperature to vary on a continuum scale (many mean free paths). Thus, the system is treated as if there were a superimposed disturbance which is transmitted by molecules having the Maxwell distribution [27]. The local departure from a Maxwellian may not be negligible, however, in which case this method may be in appreciable error. Then the actual distribution function must be determined from the Maxwell-Boltzmann transport equation. This approach will be discussed further in Chapter III.

The approach of using a local Maxwellian involves carrying out integrations over velocity half-space or other fractions of velocity space in order to obtain mean physical quantities. Some commonly occurring integrals are given in Appendix B.

2.2 Boundary conditions at a liquid-vapor interface

On a molecular scale, a description of the conditions at a liquid-vapor interface is not presently available. In approaching the problem of evaporation and condensation, a recourse is to use what is known and appeal to physical reasoning to determine simple representations for the behavior at an interface which we hope approximate the real behavior. We can then deduce further results which must be consistent with that same physical reasoning. Of course, the true test of any physical theory is comparison with experiment. If the theory does not hold up, we must be prepared to reconsider the fundamental assumptions.

The boundary conditions presently assumed at an interface in kinetic theory were formulated in the late nineteenth century. The most comprehensive accounts of the foundations of these assumptions are given by Schrage [23] and Knacke and Stranski [5]. No attempt is made here to extend those accounts but a review of some major points is given.

The starting point is the situation about which the most is known: the equilibrium situation. On the molecular scale, equilibrium is viewed as a dynamic process in which molecules leave the liquid surface into the vapor while others return from the vapor to the liquid with a resulting net balance of mass, momentum and energy. The interface is assumed to be a sharp demarcation with any transitional layer from liquid to vapor of no more than a few molecules in thickness. Experiments which support this assumption are described by Schrage [23]. Because the vapor is in equilibrium, far from the interface the distribution function must be Maxwellian. The assumption is then made that at equilibrium the interface itself is not a disturbing influence on the distribution function. Hence the Maxwellian is assumed to exist right up to the interface. Because of the net balance at the interface, we then deduce that the molecules are emitted from the liquid according to a Maxwellian with the temperature of the liquid and the density equal to the equilibrium vapor density. It is further known from experiment and thermodynamics [23] that the equilibrium vapor density is relatively insensitive to the pressure acting on the liquid. It then seems reasonable that what is emitted from the liquid depends only on the state of the liquid. This idea is then extended to the case of nonequilibrium. We imagine that the mechanism of molecules leaving the surface depends only on the state of the liquid and is not affected either by the state of the vapor or by the net transfer of mass, momentum and energy. A combination of all of the above assumptions results in the usual boundary conditions which are assumed at a liquid-vapor interface whether the system is in equilibrium or not; that is, molecules are emitted with a Maxwell distribution function with the temperature of the liquid and the density equal to the equilibrium vapor density.

Given this boundary condition, we can immediately calculate the maximum rate of evaporation w_+ which occurs when no molecules return to the interface from the vapor. Integration of the mass flux moment of the Maxwellian over velocity half-space gives (refer to Appendix B)

$$w_+ = \int_{-\infty}^{\infty}\int_{-\infty}^{\infty}\int_{0}^{\infty} \xi_x \frac{\rho^e(T_L)}{(2\pi R T_L)^{3/2}} e^{\frac{-\xi^2}{2RT}} d\xi_x d\xi_y d\xi_z = \rho^e(T_L)\sqrt{\frac{RT_L}{2\pi}} \, . \tag{2.3}$$

Many experiments have attempted to verify this maximum evaporation rate. One of the earliest successful experiments, performed by Knudsen (see Schrage [23]), verified the maximum evaporation rate for mercury. Subsequent experiments [18] have verified this result for other liquids. These experiments would seem to support the concept that the molecules emitted from the surface are a function of the state of the liquid alone. However, a claim of support cannot be made from these experiments for the use of the above boundary conditions under nonequilibrium continuum conditions.

The usual boundary conditions should be viewed as plausible yet unsubstantiated for all conditions and all liquids. Other plausible conditions can be developed and we will consider some possibilities in Chapter VI. There already exist modifications in which various coefficients are postulated to account for deviations presumed due to the particular liquid substance. These coefficients arise from consideration of the reflections of molecules from the interface. The reflections can be diffuse, specular, a combination of both, or any other scheme which can be imagined. The usual assumption is diffuse reflection. With reflections allowed at equilibrium, an evaporation coefficient can be defined. The incoming flux from the vapor at equilibrium is w_+ and of these $(1 - \alpha)w_+$ are reflected. Hence αw_+ must be evaporated to maintain equilibrium, so that the evaporation coefficient α represents the evaporation mass flux as the fraction of the maximum possible. At equilibrium there must be a net balance, so that αw_+ are condensing, and the similarly defined condensation coefficient equals the evaporation coefficient.

These concepts can also be extended to the case of nonequilibrium. The evaporation coefficient is assumed to be a property of the substance alone. Hence we speak of the evaporation coefficient for water. In nonequilibrium we could suppose that the condensation coefficient differs from the evaporation coefficient. However, these are usually assumed to be equal, again based on the behavior for the equilibrium situation. In nonequilibrium, the question of thermal accommodation arises. That is, are the reflected molecules thermally accommodated to the liquid temperature or only partially so? A thermal accommodation coefficient can be defined, but for the case of a liquid, complete thermal accommodation is usually assumed. The majority of experiments have focused on measuring the evaporation coefficient by attempting to measure the evaporation rate into a vacuum [18]. The currently popular belief is that all of the coefficients are unity for a pure freshly formed surface of a pure substance [13].

We will assume in the sequel that all of these coefficients are unity. As long as they are unity for some liquids, our conclusions will not be altered. Our conclusions are related to a more fundamental assumption that the boundary condition at an interface is described by a Maxwellian under all conditions. We emphasize once again that this boundary condition has been assumed valid for lack of any evidence to the contrary.

2.3 The Hertz-Knudsen formula

Consider two plane interfaces at temperatures T_1, T_2 separated by pure vapor. Assuming the usual boundary conditions, we know the mass flux leaving each surface:

$$w_1 = \rho_1^e \sqrt{\frac{RT_1}{2\pi}} \ , \qquad w_2 = \rho_2^e \sqrt{\frac{RT_2}{2\pi}} \ . \tag{2.4}$$

If the vapor is in the free molecular regime, so that no collisions of molecules occur, then the net mass flux is given by the difference of the two fluxes,

$$w = w_1 - w_2 = \rho_1^e \sqrt{\frac{RT_1}{2\pi}} - \rho_2^e \sqrt{\frac{RT_2}{2\pi}} \ . \tag{2.5}$$

Now consider a single interface at temperature T_1 with the vapor outside the interface at temperature T_2 and density ρ_2. Using the simple approach to continuum flow mentioned previously in which local Maxwellians are retained in the vapor, we might expect the free molecular model above to hold approximately near the interface. In this case, the flux w_1 from the surface is the same as above, and the flux w_2 from the vapor is

$$w_2 = \rho_2 \sqrt{\frac{RT_2}{2\pi}} \ .$$

The resulting expression for net mass flux at a single interface is known as the Hertz-Knudsen formula:

$$w = \rho_1^e \sqrt{\frac{RT_1}{2\pi}} - \rho_2 \sqrt{\frac{RT_2}{2\pi}} \ . \tag{2.6}$$

The temperature of the vapor might also be expected to be close to that of the liquid, while the density of the vapor can differ appreciably from the equilibrium vapor density. In this case, the approximate continuum form of the Hertz-Knudsen formula becomes

$$w \approx \sqrt{\frac{RT_1}{2\pi}} \, (\rho_1^e - \rho_2) = \frac{p_1^e - p_2}{\sqrt{2\pi R T_1}} \ . \tag{2.7}$$

2.4 Schrage's simple correction to the Hertz-Knudsen formula

Schrage [23] proposed that if the simple approach to continuum flow is used as above, then the incoming vapor should actually be represented as a Maxwellian translating with a mean velocity U since a mean velocity exists due to the net mass flow. The incoming mass flow from the vapor will then have additional terms due to the mean velocity. The outgoing mass flow from the interface is assumed to be the same as before. We take the outgoing flow to be in the positive direction and consider the case of net evaporation, so the mean flow has magnitude U in the positive direction. The case of condensation can then be obtained by taking the mean velocity -U. The incoming mass flux from the vapor is

$$w_2 = \int_{-\infty}^{\infty}\int_{-\infty}^{\infty}\int_{-\infty}^{\infty} \frac{\rho_2}{(2\pi R T_2)^{3/2}} e^{\frac{-[(\xi_x - U)^2 + \xi_y^2 + \xi_z^2]}{2RT_2}} \xi_x d\xi_x d\xi_y d\xi_z$$

$$= \rho_2 \sqrt{\frac{RT_2}{2\pi}}\, \Gamma \qquad (2.8)$$

where

$$\Gamma = e^{\frac{-U^2}{2RT_2}} - \frac{U}{2}\sqrt{\frac{2\pi}{RT_2}}\left[1 - \mathrm{erf}\left(\frac{U}{\sqrt{2RT_2}}\right)\right] .$$

The net mass flux is then

$$w = w_1 - w_2 = \rho_1^e \sqrt{\frac{RT_1}{2\pi}} - \rho_2 \sqrt{\frac{RT_2}{2\pi}}\, \Gamma . \qquad (2.9)$$

For the continuum case we might again suppose that the temperature of the vapor is close to that of the liquid, $T_2 \approx T_1$. If we also assume that the flow Mach number is small, $M \ll 1$, then

$$\frac{U}{\sqrt{2RT_2}} \ll 1 \quad \text{and} \quad \mathrm{erf}\left(\frac{U}{\sqrt{2RT_2}}\right) \approx \frac{2}{\sqrt{\pi}} \frac{U}{\sqrt{2RT_2}} .$$

With these additional assumptions, the net mass flux is

$$w = (\rho_1^e - \rho_2[1 + 0(M^2)])\sqrt{\frac{RT_1}{2\pi}} + \frac{1}{2}\rho_2 U . \qquad (2.10)$$

But ρ_2 is the continuum vapor density and U is the mean velocity, so the product is the net mass flux,

$$w = \rho_2 U .$$

Hence Schrage's form of the approximate continuum expression for mass flux for small Mach number is

$$w \approx 2(\rho_1^e - \rho_2)\sqrt{\frac{RT_1}{2\pi}} . \tag{2.11}$$

This expression is of the same form as the Hertz-Knudsen formula but is double in magnitude.

The Hertz-Knudsen and Schrage formulas are now widely used. We note again that these formulas depend on assuming (i) that the usual boundary conditions are correct for nonequilibrium continuum conditions and (ii) that the simple approach to continuum flow is valid. In recent years, the second assumption has been attacked as too crude while the first assumption has been retained. The objection to the second assumption is based on the belief that deviations from a Maxwellian may be significant near the interface under nonequilibrium conditions. In the sequel, we consider the results of retaining the usual boundary conditions while more carefully accounting for the collisions near the interface.

III. THE MAXWELL MOMENT METHOD WITH LEES' TWO-STREAM DISTRIBUTION FUNCTION

In this chapter the essentials of the Maxwell moment method as developed by Lees [9] are presented. Maxwell's integral equations of transfer are presented in cartesian form, and their use in an approximate integral technique is indicated. This technique requires the choice of an approximate distribution function containing parametric weighting functions, and Lees' two-stream distribution function is presented. Using this distribution function, we can reduce the moment equations for steady flow to first order nonlinear ordinary differential equations in terms of the parametric weighting functions. The boundary conditions can be applied to close the problem.

3.1 Maxwell's integral equations of transfer

Fundamental treatment of a nonequilibrium flow problem in kinetic theory requires solution of the Maxwell-Boltzmann transport equation in order to determine the actual distribution function. The difficulties involved in this approach are formidable, so that various approximate techniques are used. Some of these are mentioned in Chapter V.

In fluid mechanics, we are not as interested in the actual distribution function as we are in certain lower moments of the distribution function such as temperature, velocity, etc. Recognizing this, Maxwell converted the Maxwell-Boltzmann transport equation into integral equations of transfer for any quantity Q that is a function of the particle velocity alone. An approximate distribution function can then be used to calculate transport of mean quantities so that the Maxwell-Boltzmann equation is satisfied in an average sense. The integral equations of transfer can be derived directly by the usual control volume method of fluid mechanics. For details of the general case, the reader is referred to Lees [9, 10]. For simplicity, we present only the cartesian form with no external forces:

$$\frac{\partial}{\partial t}\int Q(\underset{\sim}{\xi})f(\underset{\sim}{r},\underset{\sim}{\xi},t)d\underset{\sim}{\xi} + \frac{\partial}{\partial x_i}\int f\xi_i Q d\underset{\sim}{\xi} = \Delta Q \quad . \tag{3.1}$$

The first term is the rate of increase of Q per unit volume. The second term is the rate of change of Q per unit volume due to particle transport through the bounding surface of the volume. The third term represents the effect of collisions. We note that when Q is set equal to the collisional invariants $(\Delta Q = 0)$ of mass, momentum and energy, the gas dynamic conservation equations are obtained.

The inclusion of a tractable collision term is the usual difficulty in these problems. A binary collision model is usually used and is shown by Lees to be justified for most problems of interest [9]. This model is not expected to be valid near the critical point since the probability of tertiary collisions is then significant. Maxwell discovered that if an inverse fifth power law of repulsion is used for the molecules, then the collision integral takes on a simpler form. Lees [9] has followed this approach and gives details of the collision integral calculation using this law of repulsion. He notes that this model contains the important physical features of the particle interaction and in particular preserves the nonlinear character of the collision integral.

The approach of Lees is to use the Maxwell moment equations in an approximate integral technique in the spirit of the von Karman-Polhausen treatment of boundary layer flows. The basic idea is that integration is a smoothing operation so that mean features are accurately recovered from approximate distribution functions. An approximate form of the distribution function is chosen with N parametric weighting functions to be determined. Then N moment equations can be arbitrarily chosen, although the conservation equations and other lower moments are usually used. With these N equations and N unknowns, a sufficient number of boundary conditions must be specified to close the problem. Clearly, keeping N small is desirable for ease of solution, but the number of parametric functions should be large enough that the approximate distribution function is not overly constrained. It appears that 6 moments are usually sufficient and, depending on the problem, 4 moments may be adequate.

3.2 Lees' two-stream distribution function

The successful implementation of an approximate integral technique relies to some extent on a discriminating choice of the form of the approximate distribution function. One is guided by physical insight and the practical requirement that the resulting equations be solvable. Lees was interested in developing a method which could accurately describe the transition from free molecular flow to continuum flow. Hence, physical insight suggested that the approximate distribution function should have the two-sided nature of rarefied flows and yet should be able to become almost Maxwellian in the continuum regime. In addition, the form should allow the incorporation of the boundary conditions in a natural way and the reduction of the moment equations to the simplest set of differential equations possible. Lees chose to use Maxwellian forms but with a two-sided nature. A line of sight or cone of influence principle is used to recover the rarefied behavior. Referring to Figure 1(a), we see that at a point P, for particles coming from surface I to arrive at P their outward velocity vectors must lie within the cone of influence of surface I (Region I). For this region of velocity space, we take one side of the approximate distribution function to be

$$f_1(\underset{\sim}{r}, \underset{\sim}{\xi}, t) = \frac{n_1(\underset{\sim}{r}, t)}{[2\pi R T_1(\underset{\sim}{r}, t)]^{3/2}} e^{\frac{-[\underset{\sim}{\xi} - \underset{\sim}{u}_1(\underset{\sim}{r}, t)]^2}{2RT_1(\underset{\sim}{r}, t)}} \quad . \tag{3.2}$$

The other side of the distribution function is for all other velocities which lie in the cone of influence of surface II:

$$f_2(\underset{\sim}{r}, \underset{\sim}{\xi}, t) = \frac{n_2(\underset{\sim}{r}, t)}{[2\pi R T_2(\underset{\sim}{r}, t)]^{3/2}} e^{\frac{-[\underset{\sim}{\xi} - \underset{\sim}{u}_2(\underset{\sim}{r}, t)]^2}{2RT_2(\underset{\sim}{r}, t)}} \quad . \tag{3.3}$$

The ten functions n_1, T_1, $\underset{\sim}{u}_1$, n_2, T_2, $\underset{\sim}{u}_2$ are the undetermined weighting functions. Since they are weighting functions only, in the general case these functions cannot be interpreted directly as physical quantities. For example, T_1 and T_2 should not be thought of as physical temperatures. The physical temperature must be computed from the total distribution function according to the definition in Appendix A. For the plane one-dimensional case illustrated in Figure

1(b), we will use six weighting functions. The distribution function for this case is chosen as

$$f = \begin{cases} f_1(x,t) = \dfrac{n_1(x,t)}{[2\pi R T_1(x,t)]^{3/2}} e^{-\dfrac{[\xi_x - u_1(x,t)]^2 + \xi_y^2 + \xi_z^2}{2RT_1(x,t)}} & \text{for } \xi_x > 0 \\ f_2(x,t) = \dfrac{n_2(x,t)}{[2\pi R T_2(x,t)]^{3/2}} e^{-\dfrac{[\xi_x - u_2(x,t)]^2 + \xi_y^2 + \xi_z^2}{2RT_2(x,t)}} & \text{for } \xi_x < 0. \end{cases} \tag{3.4}$$

3.3 The moment equations for the steady plane one-dimensional case

By using Lees' two-stream distribution function in Maxwell's integral equations of transfer with different functions of particle velocity Q specified, we can convert the moment equations to differential equations in terms of the weighting functions. As pointed out before, for the number of undetermined functions used, an equal number of moment equations must be obtained. The choices of Q are arbitrary, but the usual choices are the three conserved quantities and then other lower moments which are not conserved. For the plane one-dimensional case of Figure 1(b), the conservation equations are obtained by taking mass $(Q = m)$, momentum $(Q = m\xi_x)$, and energy $(Q = \frac{1}{2} m\underset{\sim}{\xi}^2)$. For a 4 moment method, Lees [10] has chosen the fourth moment as heat flux $(Q = \frac{1}{2} m\xi_x \xi^2)$. For a 6 moment method, the additional moments usually used are either $m\xi_x^2$ or $m\xi_y^2$ and $m\xi_x^3$ [8, 15, 17, 24, 26].

Sloat [26] notes that for the plane one-dimensional case, only two of $m\underset{\sim}{\xi}^2$, $m\xi_x^2$ and $m\xi_y^2$ are linearly independent. In an 8 moment calculation, Labuntsov [8] uses the additional moments $m\xi_x^4$ and $m\xi_x^5$. The derivation of the moment equations including the collision integral is well documented for the case of steady plane one-dimensional flow [9, 10, 11, 24, 26]. Sloat [26] gives the moment equations in the full nonlinear form. We present these in Appendix C and refer the reader to the references given for details. The corresponding expressions for the physical variables defined in Appendix B are also given in Appendix C.

The general form of the moment equations in Appendix C is

$$\frac{d}{dx}[\quad] = \frac{p}{\mu}[\quad] \quad . \tag{3.5}$$

We can nondimensionalize the moment equations using reference values n_o, T_o as follows:

$$\begin{aligned} \bar{n}_i &= n_i/n_o \quad , \\ \bar{u}_i &= u_i/\sqrt{RT_o} \quad , \qquad (i = 1, 2) \\ \bar{\beta}_i &= \beta_i/RT_o \quad . \end{aligned} \tag{3.6}$$

If this is done, the form of the moment equations is

$$\frac{d}{dx}[\quad] = \frac{p}{\mu\sqrt{RT_o}}[\quad] \quad . \tag{3.7}$$

For spherical molecules with a Maxwellian distribution, the viscosity can be related to the mean molecular speed C and the mean free path λ as [4]

$$\mu = \frac{1}{2}\rho C\lambda = \rho\sqrt{\frac{2}{\pi}}\sqrt{RT}\,\lambda \quad . \tag{3.8}$$

Hence using $p = \rho RT$ we see that

$$\frac{p}{\mu\sqrt{RT_o}} = \sqrt{\frac{\pi}{2}}\sqrt{\frac{T}{T_o}}\,\frac{1}{\lambda} \quad . \tag{3.9}$$

The moment equations are thus naturally scaled by the mean free path,

$$\frac{d}{d(x/\lambda)}[\quad] = [\quad] \quad , \tag{3.10}$$

which is reasonable since these equations represent changes on the kinetic theory scale. If distance is scaled by a continuum length ℓ, then the Knudsen number $Kn = \frac{\lambda}{\ell}$ is introduced into the equations

$$\frac{d}{d(x/\ell)}[\quad] = \frac{1}{Kn}[\quad] \quad . \tag{3.11}$$

3.4 Application of boundary conditions

One of the requirements in choosing the form of a distribution function is that the boundary conditions can be incorporated in a natural way. Lees' two-stream distribution function satisfies this requirement in an elegant way. If in Figure 1(b) the surfaces are taken to be liquids with the usual boundary conditions, then the particles leave surface I with a Maxwellian with temperature T_I and the number density n_I, and similarly for surface II. In accordance with Lees' two-stream distribution function given by equation (3.4), the boundary condition at surface I is

$$n_1(0) = n_I \ , \qquad T_1(0) = T_I \ , \qquad u_1(0) = 0$$

and at surface II is

$$n_2(\ell) = n_{II} \ , \qquad T_2(\ell) = T_{II} \ , \qquad u_2(\ell) = 0 \ .$$

Hence in the vapor just outside the surface, we specify what comes off the surface but leave free what comes in from the vapor which is to be determined from the solution of the problem.

With the boundary conditions incorporated, the problem is closed. In principle, a solution can be obtained to the set of coupled first order nonlinear ordinary differential equations. In practice, the full nonlinear equations require numerical solution. Analytical solutions can be obtained for the linearized problem.

IV. THE STEADY PLANE TWO-INTERFACE PROBLEM

Plesset [19] first solved the problem of the flow of vapor between liquid surfaces using the continuum equations with boundary conditions given by the continuum form of the Hertz-Knudsen formula. In current mathematical terminology, the continuum equations give the outer solution and the kinetic theory gives the inner solution. We shall see that Plesset's solution provides a good guideline for the continuum limit of the kinetic theory solutions which will be obtained using the moment method.

An illustration of the problem is given in Figure 1(b). Surface I is kept at a constant temperature T_I, surface II is kept at a constant temperature T_{II} with say $T_I < T_{II}$, and a steady flow of vapor is thus maintained from II to I. We assume for simplicity that liquid is replenished or taken away at each surface so that the surfaces are fixed in space a distance ℓ apart. We further assume that the surfaces are infinite so that a one-dimensional problem can be considered. The implicit assumption follows that whatever energy flux is required in the liquid can be supplied. This appears to be a well-posed steady problem. We note that the entire vapor flow field should be determined from the assumed known boundary conditions at the liquid surfaces. Hence this problem should be a stronger test of the theory than the single interface problems in which an arbitrary condition at infinity is imposed.

4.1 Features of the continuum formulation

For the one-dimensional steady problem posed above, the continuum conservation equations and the equation of state are

(a) Mass conservation: $\rho u = \text{constant} = \rho_{II} u_{II}$

(b) Momentum conservation: $p + \rho u^2 = \text{constant} = p_{II} + \rho_{II} u_{II}^2$

(c) Energy conservation: $\rho u c_p \frac{dT}{dx} = k \frac{d^2T}{dx^2}$

(d) Perfect gas law: $p = \rho RT$. (4.1)

Viscous effects, including dissipation, can be shown to be negligible. We first note that, since $\rho u = $ constant, the energy equation can be solved for the form of the temperature profile.

$$\frac{dT}{dx} = \frac{k}{\rho u c_p} \frac{d^2T}{dx^2} = \delta \frac{d^2T}{dx^2} , \tag{4.2}$$

$$T = C_1 e^{x/\delta} + C_2 , \tag{4.3}$$

where $\delta = \frac{k}{\rho u c_p}$ is a length parameter and has the sign of u, which is negative for the problem posed. This is the form of the temperature profile for the continuum problem, and the endpoints are pinned down by the boundary conditions. Plesset [19] uses the continuum form of the Hertz-Knudsen formula in which the assumption is made that the temperature of the vapor at a boundary is the temperature of the boundary. Plesset notes that under most continuum circumstances $|\delta| \ll \ell$, so the temperature field can be approximated by

$$T \approx T_{II} - (T_{II} - T_I) e^{\frac{-x}{|\delta|}} . \tag{4.4}$$

The temperature remains almost constant at the value of the hot side up to a region with length of order $|\delta|$ where a transition occurs to the cold temperature.

If the further assumption is made that the flow Mach number is small, $M = \left|\frac{u}{\sqrt{\gamma R T}}\right| \ll 1$, then from the momentum equation $p = \text{constant} + O(M^2)$. The equation of state and mass conservation then give to first order

$$\rho T = \rho_{II} T_{II} , \qquad \frac{u}{u_{II}} = \frac{T}{T_{II}} . \tag{4.5}$$

To close the problem, the continuum form of the Hertz-Knudsen formula (2.7) is used.

$$\begin{aligned} &\text{At } x = 0: \quad \rho_I u_I = \sqrt{\frac{RT_I}{2\pi}}\,[\rho_I^e - \rho(0)] , \\ &\text{At } x = \ell: \quad \rho_{II} u_{II} = \sqrt{\frac{RT_{II}}{2\pi}}\,[\rho(\ell) - \rho_{II}^e] . \end{aligned} \tag{4.6}$$

Plesset's solution for mass flux,

$$\rho u = -\rho_{II}^e \sqrt{\frac{RT_{II}}{2\pi}}\, \frac{1 - (\rho_I^e/\rho_{II}^e)(T_I/T_{II})}{1 + (\frac{T_I}{T_{II}})^{1/2}} , \tag{4.7}$$

is of interest for comparison with the values obtained from the kinetic theory treatment.

Since analytical results using the moment method can only be obtained for the linearized case, it is instructive to consider linearization of the continuum equations. In treating the single interface problem, Shankar [24] showed that the plane problem is a singular perturbation problem. By considering the perturbation solution to the continuum equations, he determined the proper scalings for the inner and outer solutions. We can arrive at the same results by simple considerations which clarify the nature of the solutions. We consider a small perturbation from equilibrium. The temperature of one wall is given a small perturbation and we expect the resulting flow Mach number to be similarly small. Hence we take

$$\begin{aligned} T &= T_o(1 + \epsilon T^{(1)} + \dots) \ , \\ \rho &= \rho_o(1 + \epsilon \rho^{(1)} + \dots) \ , \\ u &= \sqrt{RT_o}\,(\epsilon u^{(1)} + \dots) \ . \end{aligned} \tag{4.8}$$

The only differential equation to consider is the energy equation (4.2). The choice of distance scale determines the form of the linearized solution. We have already seen that the natural scaling for the continuum problem is $\frac{x}{\delta}$. Consider the length δ from a kinetic theory viewpoint. For spherical molecules with a Maxwellian distribution [4],

$$k \sim \mu c_v \sim \rho\sqrt{RT}\ \lambda c_v \ . \tag{4.9}$$

Then

$$\delta \sim \frac{\rho\sqrt{RT}\ \lambda c_v}{\rho u c_p} \sim \frac{\lambda}{M} \ . \tag{4.10}$$

If the energy equation is scaled with some length a, then the Knudsen number $Kn = \frac{\lambda}{a}$ appears in combination with the Mach number.

$$\frac{d\bar{T}}{d\bar{x}} = O\left(\frac{Kn}{M}\right) \frac{d^2\bar{T}}{d\bar{x}^2} \tag{4.11}$$

where $$\bar{x} = \frac{x}{a} , \quad \bar{T} = \frac{T}{T_o} \quad .$$

Using the linearized form of T, we have

$$\epsilon \frac{dT^{(1)}}{d\bar{x}} + \dots = O\left(\frac{Kn}{M}\right) \left[\epsilon \frac{d^2T^{(1)}}{d\bar{x}^2} + \dots\right] \quad . \tag{4.12}$$

If $a = \ell$, then we expect $Kn \ll M$ or $\frac{Kn}{M} = O(\epsilon)$. In this case, $T^{(1)}$ = constant and we recover the behavior that most of the continuum temperature field is a constant. If $a = \delta$, then $\frac{Kn}{M} = 1$ and we recover the exponential behavior over the length δ at the cold wall. Note that this behavior matches with the previous constant solution to give the exact solution found earlier. If $a = \lambda$, then $\frac{Kn}{M} = \frac{1}{M} = O(\frac{1}{\epsilon})$. Then $T^{(1)}$ is linear in $\frac{x}{\lambda}$. We have seen that the kinetic theory equations are naturally scaled by λ. Hence we should expect a linearized solution of the kinetic theory equations to give linear temperature profiles. In order to match with the continuum solution, we must rescale the equations as above so that x is scaled by $\frac{\lambda}{\epsilon}$ from the cold wall. Thus the kinetic theory equations on the scale of λ should give inner solutions near the walls with linear temperature profiles. The outer continuum solutions can be obtained by rescaling x with $\frac{\lambda}{\epsilon}$ from the cold wall.

One other observation can be made regarding the linearized continuum solution. In Shankar's work [24, 25], the heat flux is found to be zero at first order. This at first seems curious since we might expect a significant heat flux when the continuum temperature changes in a thin layer. However from Plesset's approximate solution (4.4) we have

$$q \sim \rho u c_p (T_{II} - T_I) \quad , \tag{4.13}$$

and u and any temperature difference are both $O(\epsilon)$. Hence $q = O(\epsilon^2)$ and the result of zero heat flux at first order appears to be consistent.

4.2 Linearized solution using six moments

Linearized solutions for the steady plane two-interface problem have been obtained by Sloat [26] and Labuntsov [8] using a six moment method. As mentioned previously, in the continuum limit these solutions give a nonphysical temperature behavior which will be clarified subsequently. We have endeavored to determine if the solutions obtained are consistent. Apparently both investigators failed to recognize the singular behavior discussed in the last section. However, as we shall see, matching with the continuum flow field does not correct the difficulty. Shankar [24] gives the linearized equations for both the inner Knudsen layer region and the outer continuum region, so we follow his notation.

Using the same linearization scheme as in the last section, we take the parametric weighting functions as

$$\begin{aligned} n_i &= n_o(1 + \epsilon N_i + \ldots) \quad , \\ T_i &= T_o(1 + \epsilon t_i + \ldots) \quad , \qquad (i = 1, 2) \\ u_i &= \sqrt{2\pi R T_o}\,(\epsilon v_i + \ldots) \quad . \end{aligned} \tag{4.14}$$

The moment equations given in Appendix C can then be linearized. For simplicity in the resulting linearized equations, the following definitions are convenient:

$$\begin{aligned} N_+ &= N_1 + N_2 , & N_- &= N_1 - N_2 , \\ t_+ &= t_1 + t_2 , & t_- &= t_1 - t_2 , \\ v_+ &= v_1 + v_2 , & v_- &= v_1 - v_2 . \end{aligned} \tag{4.15}$$

The linearized inner equations using the scaling $\bar{x} = \frac{2}{\pi} \frac{x}{\lambda}$ are to first order:

$$\begin{aligned} &(a) \quad 2N_- + t_- + 2\pi v_+ = C_1 , \\ &(b) \quad N_+ + t_+ + 4v_- = C_2 , \\ &(c) \quad 7t_- - 2N_- = 2C_3 , \\ &(d) \quad \frac{d}{d\bar{x}} [2N_- + 3t_- + 2\pi v_+] = \frac{\pi^2}{3} v_- , \\ &(e) \quad \frac{d}{d\bar{x}} [5N_+ + 10t_+ + 24v_-] = \frac{\pi}{6} [2N_- - 7t_-] , \\ &(f) \quad \frac{d}{d\bar{x}} [3N_+ + 6t_+ + 16v_-] = \frac{\pi}{4} [2N_- - t_-] . \end{aligned} \tag{4.16}$$

These can be integrated to give:

$$\begin{aligned} &(a) \quad t_- = \frac{1}{5} C_3 + C_4 \exp\left(- \frac{\pi}{4} \sqrt{\frac{5\pi}{2}} \bar{x}\right) + C_5 \exp\left(\frac{\pi}{4} \sqrt{\frac{5\pi}{2}} \bar{x}\right) , \\ &(b) \quad v_- = \frac{3}{2\pi} \sqrt{\frac{5\pi}{2}} \left[-C_4 \exp\left(- \frac{\pi}{4} \sqrt{\frac{5\pi}{2}} \bar{x}\right) + C_5 \exp\left(\frac{\pi}{4} \sqrt{\frac{5\pi}{2}} \bar{x}\right)\right] , \\ &(c) \quad N_- = \frac{7}{2} t_- - C_3 , \\ &(d) \quad t_+ = - C_2 + \frac{1}{5} \left[- \frac{\pi}{3} C_3 \bar{x} + C_6\right] - \frac{4}{5} v_- , \\ &(e) \quad N_+ = C_2 - t_+ - 4v_- , \\ &(f) \quad v_+ = \frac{1}{2\pi} [C_1 - t_- - 2N_-] . \end{aligned} \tag{4.17}$$

The linearized outer continuum equations are obtained with the scaling $\eta = \frac{x}{\lambda/\epsilon} = \epsilon\bar{x}$ from the cold wall:

$$\begin{aligned}
&(a) \quad 2N_-(\eta) + t_-(\eta) + 2\pi v_+(\eta) = A_1 \;, \\
&(b) \quad N_+(\eta) + t_+(\eta) + 4v_-(\eta) = A_2 \;, \\
&(c) \quad 7t_-(\eta) - 2N_-(\eta) = 2A_3 \;, \\
&(d) \quad v_-(\eta) = 0 \;, \\
&(e) \quad \frac{d}{d\eta}[5N_+(\eta) + 10t_+(\eta) + 24v_-(\eta)] = \frac{2\pi^2}{3} u_c[\tfrac{3}{2}t_+(\eta) - N_+(\eta) - v_-(\eta)] \\
&\qquad\qquad + \text{constant} \;, \\
&(f) \quad 2N_-(\eta) - t_-(\eta) = 0 \;,
\end{aligned} \tag{4.18}$$

where u_c is the first order velocity and is negative since $\eta = 0$ is at the cold wall. Equation (4.18(e)) can be integrated to give the alternative equation:

$$(e) \quad t_+(\eta) = A_5 + A_4 \exp(\frac{\pi^2}{3} u_c \eta) \;. \tag{4.18'}$$

The physical variables in linearized form are

$$\begin{aligned}
\rho &= \rho_o[1 + \epsilon(\tfrac{1}{2}N_+ + v_-) + \dots] \;, \\
\rho u &= \rho_o\sqrt{\frac{RT_o}{2\pi}}\,[\epsilon(N_- + \tfrac{1}{2}t_- + \pi v_+) + \dots] \;, \\
P_{xx} &= -p_o[1 + \epsilon(\tfrac{1}{2}N_+ + \tfrac{1}{2}t_+ + v_-) + \dots] \;, \\
P_{yy} &= -p_o[1 + \epsilon(\tfrac{1}{2}N_+ + \tfrac{1}{2}t_+ + 2v_-) + \dots] \;, \\
p &= p_o[1 + \epsilon(\tfrac{1}{2}N_+ + \tfrac{1}{2}t_+ + \tfrac{4}{3}v_-) + \dots] \;, \\
T &= T_o[1 + \epsilon(\tfrac{1}{2}t_+ + \tfrac{1}{3}v_-) + \dots] \;, \\
q_x &= \frac{p_o}{4}\sqrt{\frac{RT_o}{2\pi}}\,[\epsilon(7t_- - 2N_-) + \dots] \;.
\end{aligned} \tag{4.19}$$

We take an inner solution near each interface and an outer solution in between and try to match.

Inner solution at cold wall at $x = 0$:

use (4.17) with constants C_i.

Inner solution at hot wall at $x = \ell$:

use (4.17) with constants D_i and replace x by $(x - \ell)$.

Outer solution:

use (4.18) with constants A_i $(i = 1, \ldots 6)$.

We use the matching principle

$$\lim_{\bar{x} \to \infty} (\text{inner}) = \lim_{\eta \to 0} (\text{outer}) \quad \text{at } x = 0$$

and similarly at $x = \ell$. Requiring finite values, we obtain the matching conditions

(a) $A_1 = C_1 = D_1$ (mass flux constant) ,

(b) $A_2 = C_2 = D_2$ (momentum flux constant) ,

(c) $A_3 = C_3 = D_3 = 0$ (heat flux zero for finite inner value in $\lim x \to \infty$; energy flux constant) ,

(d) $C_5 = D_4 = 0$ (for finite inner values in $\lim x \to \infty$) ,

(e) $-C_2 + \frac{1}{5} C_6 = A_5 + A_4$ (match temperature at $x = 0$) ,

(f) $-D_2 + \frac{1}{5} D_6 = A_5$ (match temperature at $x = \ell$) .

(4.20)

With these matching conditions, the character of the outer continuum solution can be established as follows:

Combination of (4.20(c)) and (4.18(c)) gives $7t_- - 2N = 0$;

this result combined with (4.18(e)) gives $t_- = N_- = 0$;

from (4.18(d)) $v_- = 0$;

then from (4.18(a)) $v_+ = 2v_1 = 2v_2 = \frac{A_1}{2\pi}$.

(4.21)

Hence the outer solution to first order is a Maxwellian translating with the mean velocity, which is what we would expect from kinetic theory. Note that the temperature and density can change on the continuum scale due to second order deviations from a Maxwellian. To complete the solution, the boundary conditions must be applied. If the hot boundary is taken as the reference

$$n_o = n_{II}^e \quad , \qquad T_o = T_{II} \quad , \tag{4.22}$$

then the boundary conditions for the linearized problem become

$$\begin{aligned} &\text{At } x = 0: \; N_1 = \frac{n_I^e - n_{II}^e}{\epsilon n_{II}^e} \equiv \Delta \nu \quad , && \text{At } x = \ell : \; N_2 = 0, \\ &t_1 = \frac{T_I - T_{II}}{\epsilon T_{II}} \equiv \Delta \theta \quad , && t_2 = 0 \quad , \\ &v_1 = 0 \quad , && v_2 = 0 \, . \end{aligned} \tag{4.23}$$

Application of these boundary conditions results in the equations:

At $x = 0$

$$\text{(a)}\quad 2N_1 = 2C_2 - \frac{1}{5}C_6 + \frac{24}{\sqrt{10\pi}}\, C_4 + \frac{7}{2}C_4 = 2\Delta\nu \quad ,$$

$$\text{(b)}\quad 2t_1 = -C_2 + \frac{1}{5}C_6 + \frac{6}{\sqrt{10\pi}}\, C_4 + C_4 = 2\Delta\theta \quad ,$$

$$\text{(c)}\quad 2v_1 = \frac{1}{2\pi}\left[C_1 - 8C_4 - 3\sqrt{\frac{5\pi}{2}}\, C_4\right] = 0 \quad ,$$

At $x = \ell$ (4.24)

$$\text{(d)}\quad 2N_2 = 2D_2 - \frac{1}{5}D_6 - \frac{24}{\sqrt{10\pi}}\, D_5 - \frac{7}{2}D_5 = 0 \quad ,$$

$$\text{(e)}\quad 2t_2 = -D_2 + \frac{1}{5}D_6 - \frac{6}{\sqrt{10\pi}}\, D_5 - D_5 = 0 \quad ,$$

$$\text{(f)}\quad 2v_2 = \frac{1}{2\pi}\left[D_1 - 8D_5 - 3\sqrt{\frac{5\pi}{2}}\, D_5\right] = 0.$$

The equations (4.24) and the matching conditions (4.20) determine the constants:

$$C_1 = \frac{8 + 3\sqrt{\frac{5\pi}{2}}}{\frac{6}{\pi}\sqrt{\frac{5\pi}{2}} + \frac{9}{2}}\,(\Delta\nu + \Delta\theta) = 1.665\,(\Delta\nu + \Delta\theta) \quad ,$$

$$C_2 = \Delta\nu + \Delta\theta \quad ,$$

$$C_4 = D_5 = \frac{C_1}{8 + 3\sqrt{\frac{5\pi}{2}}} \quad , \qquad (4.25)$$

$$A_5 = \frac{1 + \frac{6}{\sqrt{10\pi}}}{\frac{9}{2} + \frac{6}{\sqrt{10\pi}}}\,(\Delta\nu + \Delta\theta) = 0.21015\,(\Delta\nu + \Delta\theta) \quad ,$$

$$A_4 = 2\Delta\theta - 2A_5 = 1.5797\,\Delta\theta - 0.4203\,\Delta\nu \quad .$$

The physical variables of interest are mass flux and temperature:

$$\frac{\rho u}{\rho_{II}^{e}\sqrt{\frac{RT_{II}}{2\pi}}} = \epsilon\,\frac{C_1}{2} = \frac{1.665}{2}\,\epsilon\,(\Delta\nu + \Delta\theta) \ , \qquad (4.26)$$

$$\frac{T}{T_{II}} = 1 + \epsilon\,\frac{1}{2}\left[0.21015\,(\Delta\nu + \Delta\theta) + (1.5797\,\Delta\theta - 0.4203\,\Delta\nu)\exp\left(\frac{\pi^2}{3}u_c\eta\right)\right] \ ,$$

$$\text{where} \quad u_c = \frac{C_1}{4\pi} < 0 \ . \qquad (4.27)$$

For reference we give the free molecular mass flux

$$\frac{(\rho u)_{fm}}{\rho_{II}^{e}\sqrt{\frac{RT_{II}}{2\pi}}} = \epsilon\,(\Delta\nu + \frac{1}{2}\Delta\theta) \ . \qquad (4.28)$$

It is interesting that the mass flux and end values of temperature are the same as in Sloat's solution in which matching is not done. Apparently, matching of the conserved constants of mass flux, momentum flux and energy flux determines the end values.

A comparison of the mass flux with Plesset's solution can now be made. If Plesset's result for mass flux (4.7) is linearized, the result is

$$\frac{\rho u}{\rho_{II}^{e}\sqrt{\frac{RT_{II}}{2\pi}}} = \frac{1}{2}\,\epsilon\,(\Delta\nu + \Delta\theta) \ . \qquad (4.29)$$

Both expressions are proportional to the vapor pressure difference $(\Delta\nu + \Delta\theta)$. However the result above is larger than Plesset's by a factor 1.665. If Schrage's correction to the Hertz-Knudsen formula (2.11) had been used in Plesset's theory, the result would be

$$\frac{\rho u}{\rho_{II}^{e}\sqrt{\frac{RT_{II}}{2\pi}}} = \epsilon(\Delta\nu + \Delta\theta) . \tag{4.30}$$

The factor of 2 in Schrage's correction just carries through. Hence the present result (4.26) agrees qualitatively with Schrage's correction. Accounting for the effect of collisions reduces the magnitude of the correction from 2 to 1.665.

As mentioned previously, two physically unreasonable solutions are possible from (4.26, 4.27) depending on the magnitudes of $\Delta\nu$ and $\Delta\theta$. First, it is possible that the continuum mass flux exceeds the free molecular mass flux if

$$\Delta\nu < 1.98\,\Delta\theta \;.$$

Secondly, the temperature at the hot wall can be below that at the cold wall if

$$\Delta\nu > 3.76\,\Delta\theta \;.$$

In the literature, the ratio of $\Delta\nu$ and $\Delta\theta$ has been called β:

$$\beta = \frac{\Delta\nu}{\Delta\theta} \;. \tag{4.31}$$

The equilibrium vapor density is a function of the temperature, and $\Delta\nu$ and $\Delta\theta$ are related for real liquids by the Clausius-Clapeyron equation:

$$\frac{dp^{e}}{dT} = \frac{L}{T(\mathcal{v}_{v} - \mathcal{v}_{L})} \approx \frac{L\rho^{e}}{T} \;, \tag{4.32}$$

where L is the latent heat of vaporization. In nondimensional form,

$$\frac{dp^{e}/p^{e}}{dT/T} = \frac{L\rho^{e}}{p^{e}} = \frac{L}{RT} \;. \tag{4.33}$$

For small but finite temperature changes, we have the approximate relation

$$\beta + 1 = \frac{\Delta p^e / p^e}{\Delta T / T} \approx \frac{L}{RT} \quad . \tag{4.34}$$

Some representative values of this latent heat parameter are given in Table I. It is apparent from Table I that the condition $\beta > 3.76$ is usually satisfied. Hence the solution obtained indicates that the temperature profile is always inverted. We believe this is physically unreasonable. It would not seem possible for a relatively large temperature jump to occur over a few mean free paths. Further, a large temperature change over a few mean free paths is in contradiction of the basic concept of temperature.

An example is illustrative. Consider water at the boiling point at the hot surface and the cold surface lower by 1°K. Then $\epsilon \Delta \theta = \frac{1}{373} = 0.00268$. From Table I, $\beta \approx 12.1$ so $\epsilon \Delta \nu = 0.0324$. Then from (4.27), the temperature in the vapor at the cold surface is 0.38°K above 373°K, and the temperature in the vapor at the hot surface is 1.38°K below 373°K. This clearly does not make sense. This inverted temperature profile or "negative temperature gradient" has been reported in the literature for solutions by other methods [1, 12, 16]. However, rather than questioning the physical solution, those investigators reported the solution as a new physical phenomena. We believe that the inverted temperature profiles constitute a reason to strongly doubt the theory.

We have examined the linearized solution and, with the matching, the mathematical method of solution appears to be consistent. However, the physics indicates that there is a serious error in the solution. In order to further check whether the linearization is the difficulty, a numerical solution of the full nonlinear equations was attempted.

4.3 Numerical solution of the nonlinear moment equations

The one-dimensional steady plane two-interface problem is a two-point boundary value problem. Using the six moment method, the governing equations are six, coupled, nonlinear first order ordinary differential equations. Three boundary conditions are specified at each end. To solve this system numerically, an initial value problem shooting technique is used with integration by a Runge-Kutta and predictor-corrector scheme. The two-point boundary value conditions are satisfied by correcting an initial guess to the function values at the end from which the shooting originates. Sloat [26] attempted the same type of numerical solution but only treated the case $\beta = 1$. We have improved upon his technique and have treated more relevant values of β with the intention of answering the questions posed in the last section.

The moment equations given in Appendix C can be written in the matrix form

$$\underset{\sim}{A}\underset{\sim}{y}' = \underset{\sim}{G}, \quad \text{or} \quad A_{ij}y_j' = G_i \qquad (i, j = 1, \ldots, 6) , \qquad (4.35)$$

where prime denotes differentiation with respect to x and the y_j are the unknown parametric functions. Sloat [26] has already written the nonlinear equations in this form and we use the same equations. The equations in this form are given in Appendix D. By matrix inversion, the system of equations can be written as

$$\underset{\sim}{y}' = \underset{\sim}{A}^{-1}\underset{\sim}{G} = \underset{\sim}{f} . \tag{4.36}$$

In this form, the equations can be integrated by any standard technique for ordinary differential equations such as a Runge-Kutta method. Note that the matrix inversion must be carried out numerically at each step of the integration. As an integration technique, we have used the Adams-Moulton predictor-corrector method combined with the standard fourth order Runge-Kutta method [2]. The advantages of the predictor-corrector method over the Runge-Kutta method are that less function evaluations are required and the accuracy versus step size is better (so that large step sizes may be used). Both advantages save computing time which is important here because a large number of iterations may be required for convergence. The Runge-Kutta method is necessary to generate the starting values for the predictor-corrector.

A variable step size is incorporated to allow control of the error at each step. In this way, we have some assurance that the integration maintains some consistent overall accuracy. The procedure for variable step size with error control is as follows:

1. Some error bounds, ERRMAX and ERRMIN, are specified by the user as well as an initial stepsize h. For example, ERRMAX= 10^{-5}, ERRMIN= 10^{-8}, and h=0.01.

2. The integration begins with the Runge-Kutta method. Consider just the first step.

   a) The Runge-Kutta integrates from 0 to h.
   b) The step size is halved and the Runge-Kutta integrates from 0 to h/2 and then from h/2 to h.

c) The values at $x = h$ from (a) and (b) are compared to compute a relative error, ERR.

d) If ERR > ERRMAX, then sufficient agreement has not been obtained. The step size is halved and the procedure started again at $x = 0$.

e) If ERR < ERRMIN, then computing time is wasted because the step size is too small. The step size is doubled and the procedure started again.

f) If ERRMIN < ERR < ERRMAX, then continue.

3. A similar procedure as in (2) is continued at succeeding steps until three steps are generated with the same step size h.

4. With three previous steps determined, the predictor can integrate to the next step. The corrector then computes a correction at this step. The values from the predictor and corrector are then compared to compute a relative error, ERR.

a) If ERR > ERRMAX, then the step size is halved and the Runge-Kutta routine is called to generate three more steps. The predictor-corrector then starts over with these three new values.

b) If ERR < ERRMIN, then the predictor-corrector is continued until a sufficient number of points are obtained to switch over to double step sizes. The step size is then doubled and the predictor-corrector continued.

c) If ERRMIN < ERR < ERRMAX, then the predictor-corrector continues.

5. Some arrangement must be made to hit the terminating end exactly.

This procedure has been found to be very efficient for this problem. However, the user must be careful to choose ERRMAX and ERRMIN of sufficiently different magnitude to avoid getting stuck in a loop which halves and doubles step sizes over and over.

The integration procedure outlined above is appropriate for an initial value problem in which the boundary conditions at $x = 0$ are known. For a two-point boundary value problem, an initial guess must be made to the solution at $x = 0$. The results of the subsequent integration at $x = \ell$ can then be compared to the given boundary conditions. Iterations on the guess at $x = 0$ must then follow until convergence to a solution is achieved. In general, the boundary conditions can be written as

$$\text{At } x = 0: \ \underset{\sim}{g}_{I}(\underset{\sim}{y}(0)) = 0 \ , \qquad \text{At } x = \ell: \ \underset{\sim}{g}_{II}(\underset{\sim}{y}(\ell)) = 0 \ , \tag{4.37}$$

where $\underset{\sim}{g}_{I}$ and $\underset{\sim}{g}_{II}$ represent three equations each for a total of six boundary conditions. For the given boundary conditions, however, the parametric functions y_j are uncoupled in the boundary conditions, so the conditions at $x = 0$ can be exactly satisfied by the guess $\underset{\sim}{s}$. The satisfaction of the boundary conditions at $x = \ell$ is then equivalent to finding the root $\underset{\sim}{s}$ of three coupled nonlinear "algebraic" equations

$$\underset{\sim}{g}_{II}(\underset{\sim}{y}(\ell);\underset{\sim}{s}) = 0 \ . \tag{4.38}$$

The functional character is obviously very complicated because a numerical integration is required to define the functions. Nevertheless, the numerical technique of solution is the same as if there was a system of three coupled nonlinear algebraic equations.

The classical method for solving a system of nonlinear algebraic equations,

$$f_i(\underset{\sim}{x}) = f_i(x_1, \ldots, x_n) = 0 \qquad (i = 1, \ldots, n) \ , \qquad (4.39)$$

is the Newton-Raphson iteration. Given an approximate solution $\underset{\sim}{x}^{(k)}$, we seek the corrected solution $\underset{\sim}{x}^{(k+1)} = \underset{\sim}{x}^{(k)} + \delta \underset{\sim}{x}^{(k)}$. Taking a Taylor's series expansion about $\underset{\sim}{x}^{(k)}$, we seek

$$f_i(\underset{\sim}{x}^{(k+1)}) = f_i(\underset{\sim}{x}^{(k)}) + \frac{\partial f_i}{\partial x_j}(\underset{\sim}{x}^{(k)}) \, \delta x_j^{(k)} + \ldots = 0 \ . \qquad (4.40)$$

Neglecting the higher order terms, we obtain the correction $\delta \underset{\sim}{x}^{(k)}$ by solving the linear system

$$f_i(\underset{\sim}{x}^{(k)}) + J_{ij}^{(k)} \, \delta x_j^{(k)} = 0 \ , \qquad (4.41)$$

where

$$J_{ij}^{(k)} = \frac{\partial f_i}{\partial x_j}(\underset{\sim}{x}^{(k)})$$

is the matrix of first derivatives evaluated at $\underset{\sim}{x}^{(k)}$. For a complicated functional behavior, the first derivatives can be approximated numerically by considering "sufficiently small" increments in each variable. For example,

$$J_{21} \approx \frac{f_2(x_1^{(k)} + \Delta x_1, x_2^{(k)}, \ldots, x_n^{(k)}) - f_2(\underset{\sim}{x}^{(k)})}{\Delta x_1} \ . \qquad (4.42)$$

This iteration does not always succeed and a common modification is to scale the correction as

$$\underset{\sim}{x}^{(k+1)} = \underset{\sim}{x}^{(k)} + \lambda^{*} \delta \underset{\sim}{x}^{(k)} \tag{4.43}$$

where the number λ^{*} is generated by some scheme which optimizes the correction. We used both of these methods but still had difficulty in obtaining convergence. Satisfied that these schemes were insufficient alone, we resorted to a hybrid method due to Powell [20]. This method combines the previous methods with a method of steepest descent. For further details, the reader is referred to Powell [20].

The final consideration is how to generate the initial guess. The free molecular solution provides a known solution from which to start. Alternatively, we have found that the linearized solution of Sloat [26] provides a good enough guess for $Kn = 1$. The procedure then is to decrease the parameter Kn, using the solution to the previous Kn as the next initial guess. In this way, a reasonable first guess is obtained. Note here that $Kn = \frac{\lambda}{\ell}$ so that if distance is scaled by mean free path, $\bar{x} = x/\lambda$ then the integration is over a distance $\bar{x} = \bar{\ell} = \frac{1}{Kn}$.

4.4 Results of the numerical solution

The numerical study was initiated with the intention of checking the full nonlinear theory in the continuum limit. In principle, the numerical solution can be obtained for the six nonlinear first order ordinary differential equations with the six boundary conditions. However, we have found that in practice there are some difficulties which could not be overcome with a straightforward approach.

The difficulty with convergence was briefly mentioned in the last section. The criteria for convergence is a requirement that the sums of the squares of the errors (SUMSQ) for the three boundary conditions be less than some specified value ACC. All calculations were done in double precision. Usually, the modest requirement $ACC = 10^{-8}$ was used, which roughly means that we accept 10^{-4} to be "zero". The difficulty with convergence increased as the Knudsen number was lowered in attempting to approach the continuum regime. The example in Table II is representative of the difficulty. We see that, when the solution converges, it usually does so with the quadratic convergence characteristic of Newton's method. The very slow improvement in the solution is apparently the method of steepest decent portion. Clearly, this difficulty with convergence prevents obtaining any conclusive results regarding the continuum limit.

Another numerical difficulty is that the solutions have an exponential character. Relatively small changes in the initial conditions result in large changes in the solution. By using Kn as a parameter as mentioned in the last section, we were always able to stay close to a solution as Kn was decreased. The limiting factor is always convergence. The exponential character presents another difficulty. To approach the continuum limit, the integration must proceed over many mean free paths. To test the numerical stability of the equations over many mean free paths, the conditions for a uniform gas were specified as the initial conditions. There should be no changes in this case. However, it was found that small numerical errors grew to significant errors in less than 20 mean free paths. This behavior occurs regardless of the direction of integration with respect to the mean flow. Therefore, the calculation of the continuum flow field is not possible using this approach. This instability could be a factor in the difficulty with convergence described earlier.

While conclusive results could not be obtained for the continuum regime, the solutions obtained indicate support of the linearized theory. The linearized theory of Sloat should be valid for $Kn = O(1)$. The numerical results verify this. Departures from the linearized theory occur as Kn approaches 0.1. The numerical results also indicate that the objectionable results in the linearized theory are not just a result of linearization. For $\beta = 1$, the mass flux exceeds the free molecular value for $Kn = 1/6$. For $\beta = 12$, inverse temperature profiles result for all Kn for which solutions could be obtained. While temperature changes do not have physical meaning over a few mean free paths, the trend of the solutions shown in Figures 2 and 3 indicates that as Kn is decreased, the solutions approach the end values given by the continuum limit of the linearized theory of Section 4.2. For comparison with Figures 2 and 3, the end values for temperature from (4.27) are

$$\begin{aligned} &\text{At } x = 0 \qquad T = +0.0073 \ , \\ &\text{At } x = \ell \qquad T = -0.0137 \ . \end{aligned} \tag{4.44}$$

The conclusions from the numerical study are as follows:

1. For suitably small changes in temperature, the nonlinear solution agrees with the linearized solution for $Kn = O(1)$.

2. Numerical solution of the continuum problem is not possible

using a straightforward approach. Therefore, definite conclusions cannot be stated regarding the continuum limit.

3. The trend of the numerical results indicates that the inverted temperature profile is not merely a result of linearization.

Finally, we note that a possible approach to the continuum problem is to use the numerical solution indicated in this section as an inner solution near the interface and numerically match to an outer continuum flow field.

4.5 Conclusions from the moment method solution of the steady plane two-interface problem

A result of the continuum limit of the linearized solution is that inverted temperature profiles occur if the latent heat parameter β satisfies the condition $\beta > 3.76$. For real liquids under most conditions, the condition $\beta > 3.76$ is satisfied and usually $\beta \sim 10$. We believe the result of inverted temperature profiles is unphysical and therefore we question the theory.

The Maxwell moment method as developed by Lees appears to be able to describe the transition from the free molecular regime to the continuum regime. The linearized six moment solution appears to be consistent. The numerical study lends some support to the linearized solution, although nothing conclusive can be stated with regard to the continuum limit. Therefore, the difficulty appears to be in the fundamental theory and not in the method of solution.

Assuming that the formulation and solution are mathematically consistent but physically incorrect, we can question two fundamental physical assumptions. First, is it possible that the steady problem with a fixed temperature difference between the two walls is not well posed? We do not have an argument which would indicate that this is the difficulty. However, further study of unsteady problems may be justified in order to answer this question more convincingly. Secondly, is it possible that the usual boundary conditions are incorrect? We believe that this assumption is not well justified and is probably the source of the difficulty. Before questioning the theory further, it is useful to consider the results of other investigators in light of the objections raised. In the next chapter, a brief review of related work is presented.

V. THE CONSIDERATION OF RELATED PROBLEMS AND SOLUTIONS BY OTHER METHODS

Physical objections were presented in Chapter IV to the solutions obtained to the steady plane two-interface problem by a six moment method. In this chapter, solutions in the literature to both this problem and related problems are discussed with respect to the aforementioned objections. No attempt is made here to examine the details of these solutions. Rather, the results are compared to the results of the six moment method which we have examined in detail.

5.1 Solutions for the steady plane two-interface problem

Sloat [26] and Labuntsov [8] have treated this problem with the six moment method as mentioned previously. Sloat obtained the same results at the boundaries as found in Chapter 4. Labuntsov apparently finds the same solution although he does not give the temperature profile explicitly. Neither author notes the unusual temperature profiles, apparently due to their primary concern with the mass flux.

Pao [16] solves the problem using the linearized Boltzmann (BGKW) equation. He notes the inverted temperature profile, calling it a "negative temperature gradient". According to his solution, this effect occurs for $\beta > 3.5$ which agrees favorably with the result from the moment method of $\beta > 3.76$. Pao notes that usually $\beta > 3.5$ is satisfied except near the critical point where the theory breaks down anyway. He does not question the theory although he finds the physical result surprising. Matsushita [12] solves the linearized BGK equation numerically. He finds the critical value of β to be 3.75 and reports the unpublished result of Sone and Onishi to be 3.77. He notes that the mass flux exceeds the free molecular mass flux for $\beta < 2$, which is in agreement with the result from the moment method. Cippola et. al [1] obtain similar results using a variational formulation of the BGK equation. Neither Cippola nor Matsushita questions the physical result. It appears that the inverted temperature profile is a consequence of the theory and not of the mathematical method of solution.

5.2 The steady plane single interface problem

A refined treatment of the steady plane single interface problem was first attempted by Schrage [23]. He used the three conservation equations in a method similar to the moment method. The choice of distribution function is now critical since only one degree of freedom is allowed. Apparently Schrage's choice of distribution function was poor because the solution differs greatly from more recent treatments. Ytrehus [28] revived Schrage's simple approach but chose a "better" form of the distribution function. His results agree well with those from other more elaborate techniques. He clarified the concept which Schrage had used that only one parameter at infinity (say pressure) determines the solution, given the liquid conditions. This apparently is a result of requiring a uniform gas at infinity. Ytrehus concludes that the solution is "of a one-parameter nature, independent of the collisional dynamics" (i.e. depends only on the conservation equations). Temperatures at the interface are not given.

It appears to the present investigator that the consideration of a single interface with a uniform gas at infinity just obscures the difficulty encountered in the two-interface problem. In the two-interface problem, the state of the gas outside the interface is determined by the conditions at the two interfaces and is not of a one-parameter nature. Thus if the single interface solution is taken as the inner solution at each boundary, the problem would appear to be over-specified. To clarify this point, we consider the Ytrehus model as the inner solution at each boundary. At the first boundary we specify the temperature and vapor density. The choice of one parameter "at infinity", say the pressure, then determines the solution. Because only conservation equations are used and the conserved quantities are constants for a steady problem, we can cross over the continuum flow field to the other boundary. With the vapor conditions already determined, we can only specify one parameter in the liquid, say the temperature. The equilibrium vapor density is then determined. The solution obtained in this manner has a flat (constant) temperature profile in the continuum field and thus corresponds to the critical condition between inverted and non-inverted temperature profiles. For low Mach number, the result of the calculation described above is that the flat profile can only exist for $\beta \simeq 3.78$. This is the same result obtained previously for the critical value of β.

Muratova and Labuntsov [15] have extensively treated the steady single interface problem. They have used 6 and 8 moment methods as well as the linearized Boltzmann equation. The vapor conditions at infinity were assumed known rather than of a one-parameter nature. The solutions obtained by the different methods are all similar and exhibit inverted temperature profiles for $\beta > 3.7$. This behavior is explicitly shown in a figure. However, they report this behavior as "a new physical effect, accompanying processes of vaporization and condensation" in which the vapor at a boundary may be "superheated and supersaturated".

Ytrehus also performed some effusion experiments through a porous wall to simulate the usually assumed boundary conditions for evaporation. The experimental results agree well with his one-parameter solution. Thus there is some experimental verification that the kinetic theory solutions do correspond physically to the usual boundary conditions. However, evaporation from a liquid need not be identical to effusion.

5.3 The unsteady plane single interface problem

The unsteady single interface problem has been treated by Shankar [24] using a linearized six moment method. The time dependence was treated using the Laplace transform technique. For large time (continuum), the mass flux was found to agree approximately with the Hertz-Knudsen formula, being somewhat lower in magnitude. This agreement with the Hertz-Knudsen formula rather than with Schrage's correction is apparently due to the lack of a mean flow at infinity. Unfortunately, the temperature at the interface is not given. However, in his quasi-steady analysis, the same mass flux is found and the temperature is available from his solution. The profile is not inverted but can have a very large jump at the surface. The unsteady problem has also been solved numerically by Murakami and Oshima [14] using a Monte-Carlo technique. They note that inverted temperature profiles occur for $\beta > 3.5$.

5.4 The steady spherical droplet in infinite vapor

The present interest in the spherical droplet problem is concern with the singular nature of the plane geometry. The spherical droplet has been treated by Shankar [24] and Sampson and Springer [22]. However, a discrepancy between the two exists as to the basic equations. No attempt has been made here to resolve the discrepancy. We only point out here that both solutions are physically objectionable. Sampson and Springer find a continuum mass flux at the surface of the droplet which is always double the free molecular mass flux. This would appear to be physically unrealistic and is an indication that they have probably made an error. Shankar finds that the continuum mass flux at the surface of the droplet is the same as the result for the plane case. However, if we use his equations and consider flow of vapor between an inner droplet and an outer sphere of liquid, then once again inverted temperature profiles are obtained. It appears that the difficulties with the plane case are not merely due to geometry. However, due to the unresolved discrepancy between the equations of Shankar and those of Sampson and Springer, nothing conclusive can be stated.

VI. DISCUSSION

In the course of this study on the kinetic theory of evaporation and condensation at an interface, objections to the theory have been raised questioning the physical validity of the solutions. The following two premises have been assumed in this study:

i) The free molecular mass flux is a maximum for given boundary conditions.

ii) Inverted temperature profiles, in which the temperature of the vapor at the hot interface is lower than the temperature of the vapor at the cold interface, are physically unreasonable.

We have found that the first premise is satisfied for real liquids, although some investigators have found otherwise. However, inverted temperature profiles have been found to result from the current theory for all real liquids. Because other investigators have not questioned these results on physical grounds, a defense of the above premises appears necessary.

The free molecular mass flux between two liquid surfaces is a result of the net exchange of molecules without any collisions. When collisions occur, what would be the effect on the net mass flux? The answer must be that the net mass flux is reduced, not increased. To imagine the situation, consider the liquid surfaces originally less than one mean free path apart. Now move the surfaces apart until they are separated by thousands of mean free paths. The effect of thousands of collisions must be to reduce the net transport.

The idea of the inverted temperature profile must appear ridiculous to one familiar with the concepts of continuum fluid mechanics because continuity of temperature is usually assumed at a liquid-vapor interface in continuum mechanics. However, the concept of "temperature slip" or a temperature jump at a boundary is well known in rarefied gas dynamics. In kinetic theory, "continuum" means that locally the distribution function is Maxwellian. If strong disturbing influences are present so that the distribution function deviates from a Maxwellian, then the assumptions of continuum mechanics break down. This may be the case at a liquid-vapor interface under highly nonequilibrium conditions. A transition to continuum flow occurs in a layer near the interface a few mean free paths in thickness (the Knudsen layer). The temperature at the edge of the Knudsen layer may then not be the same as the temperature of the liquid. Thus on the continuum scale there appears to be a temperature jump (surface shock [6]). We do not object here to the concept of a continuum temperature jump at the interface. We only question the possible magnitude of such a jump. How can it be possible that the temperature jump at an interface is larger than the temperature difference between the two interfaces (see the example on p. 30)? We do not believe that such relatively large changes in temperature over just a few mean free paths are physical. We stress that such changes are in contradiction of the basic physical concept of temperature.

Because of the resulting inverted temperature profiles obtained for all liquids, we have questioned the current theory. The conclusion of this study is that the various methods of solution appear to be consistent so that the difficulty is of a fundamental nature in the statement of the problem. The problems considered seem to be physically well posed. Hence the only questionable assumption remaining is the assumed boundary condition for particles emitted from a liquid surface. In the present study, no attempt has been made to review the literature extensively for evidence of experimental support of the usually assumed boundary conditions. We are not aware of any strong support for these boundary conditions under continuum conditions. The majority of experiments have sought to measure the evaporation or condensation coefficients using the Hertz-Knudsen formula [5, 13]. These experiments do support the form of the Hertz-Knudsen formula. Note that the existence of non-unity evaporation and condensation coefficients for some liquids does not change our conclusion since we need only consider a liquid for which these coefficients are unity.

The conclusion that the usual boundary conditions are probably wrong has not been reached casually, as evidenced by the present efforts to find a flaw in the method of solution. This conclusion appears to be the only logical choice. It would be helpful to understand the nature of the difficulty imposed by these boundary conditions. One simple explanation which must play a role is the following. The equilibrium vapor density increases exponentially with temperature, but the perfect gas law prescribes that density is the inverse of temperature with constant pressure. For the two-interface problem, the pressure is constant to second order in Mach number. It thus appears that the high equilibrium vapor density from the hot liquid causes the vapor density at the interface to be relatively high, and thus the temperature must be relatively low. The density appears to be the controlling factor.

The basis for questioning the boundary conditions has been established. The next step is to examine alternative boundary conditions. The fundamental assumptions underlying the usual boundary conditions are that what is emitted from the liquid is a function of the state of the liquid and not of the state of the vapor or of the net transport of mass, momentum and energy. Alternative boundary conditions must be formulated by relaxing some of these assumptions but must remain plausible. Fiszdon [3] has also questioned the usual boundary conditions and has suggested an alternative formulation which accounts for the energy transport in the liquid. Another plausible alternative has been suggested by Prosperetti [21]. He suggests that in the continuum case the mean flow may affect the emission from the liquid in such a way that the Maxwellian is shifted. In this case, it is possible that the correction of the Hertz-Knudsen formula for mean velocity is of first order in Mach number rather than the factor of 2 found by Schrage using the usual boundary conditions. Other plausible formulations are possible.

As to future work toward solving the problem of evaporation and condensation at a liquid-vapor interface, the following investigations are suggested:

1. The only possible difficulty with the kinetic theory methods is with the approach to the continuum limit. Further thought should be given as to the validity of the current methods in this regard.

2. Experimental results in the literature should be reviewed to determine whether the usual boundary conditions are supported or not. Assuming lack of support will be found, known experimental results should be established to serve as guidelines for any new plausible boundary conditions.

3. Plausible boundary conditions should be tested using the current methods to check whether reasonable results are obtained for real liquids.

4. Critical experiments must be designed and performed to establish the proper boundary conditions and to serve as the ultimate test for the theory.

REFERENCES

1. Cippola, J. W., Lang, H., and Loyalka, S. K., "Kinetic Theory of Condensation and Evaporation. II", J. Chem. Phys., 61, 69-77 (1973).
2. Conte, S. D., Elementary Numerical Analysis, McGraw-Hill, New York (1965).
3. Fiszdon, W., Personal communication. Also, "Remarks on the Boundary Conditions at the Liquid-Vapor Interface for the Continuum Vapor Region", unpublished, submitted to Annals of Nuclear Engineering (1979).
4. Kennard, E. H., Kinetic Theory of Gases, McGraw-Hill, New York (1938).
5. Knacke, A. and Stranski, I. N., "The Mechanism of Evaporation", Progr. Metal Phys., 6, 181-235 (1956).
6. Kogan, M. N., "Molecular Gas Dynamics", Annual Review of Fluid Mechanics, 5, 383-404 (1973).
7. Kogan, M. N. and Makashev, N. K., "Role of the Knudsen Layer in the Theory of Heterogeneous Reactions and in Flows with Surface Reactions", Fluid Dynamics (transl. of Mekh. Zhidk. Gaza), 6, 913-920 (1971).
8. Labuntsov, D. A., "An Analysis of Evaporation and Condensation Processes", High Temperature (transl. of Teplofiz. Vys. Temp.), 5, 579-585 (1967).
9. Lees, L., "A Kinetic Theory Description of Rarefied Gas Flows", Hypersonic Research Project Memo. No. 51, GALCIT, Pasadena (1959).

10. Lees, L., "Kinetic Theory Description of Rarefied Gas Flow", J. Soc. Indust. Appl. Math, 13, 278-311 (1965).

11. Liu, C. and Lees, L., "Kinetic Theory Description of Plane Compressible Couette Flow", Rarefied Gas Dynamics, 391-428 (1961).

12. Matsushita, T., "Kinetic Analysis of the Problem of Evaporation and Condensation", Physics of Fluids, 19, 1712-1715 (1976).

13. Mills, A. F. and Seban, R. A., "The Condensation Coefficient of Water", International J. of Heat and Mass Transfer, 10, 1815-1827 (1967).

14. Murakami, M. and Oshima, K., "Kinetic Approach to the Transient Evaporation and Condensation Problem", Rarefied Gas Dynamics, F. 6-1 - F. 6-9 (1974).

15. Muratova, T. M. and Labuntsov, D. A., "Kinetic Analysis of Vaporization and Condensation Processes", High Temperature (transl. of Teplofiz. Vys. Temp.), 7, 888-896 (1969).

16. Pao, Y., "Application of Kinetic Theory to the Problem of Evaporation and Condensation", Physics of Fluids, 14, 306-312 (1971).

17. Patton, A. J. and Springer, G. S., "A Kinetic Theory Description of Liquid Vapor Phase Change", Rarefied Gas Dynamics, 1497-1501 (1968).

18. Paul, B., "Compilation of Evaporation Coefficients", American Rocket Soc. J., 32, 1321-1328 (1962).

19. Plesset, M. S., "Note on the Flow of Vapor Between Liquid Surfaces", J. Chem. Phys., 20, 790-793 (1952).

20. Powell, M. J. D., "A Hybrid Method for Nonlinear Equations", in Numerical Methods for Nonlinear Algebraic Equations, Ed. by P. Rabinowitz, Gordon and Breach Science Publ., New York (1970).

21. Prosperetti, A., Personal communication.

22. Sampson, R. E. and Springer, G. S., "Condensation on and Evaporation from Droplets by a Moment Method", J. Fluid Mechanics, 36, 577-584 (1969).

23. Schrage, R. W., A Theoretical Study of Interphase Mass Transfer, Columbia Univ. Press, New York (1953).

24. Shankar, P. N., "A Kinetic Theory Investigation of Some Condensation-Evaporation Phenomena by a Moment Method", Ph. D. thesis, Part II, California Institute of Technology (1968).

25. Shankar, P. N. and Marble, F. E., "Kinetic Theory of Transient Condensation and Evaporation at a Plane Surface", Physics of Fluids, 14, 510-516 (1971).

26. Sloat, T. N., "Investigation of Mass Transfer Between Two Parallel Walls at Different Temperatures by a Moment Method", Ph. D. Dissertation, University of Southern California (1971).

27. Tolman, R. C., Statistical Mechanics with Applications to Physics and Chemistry, Chemical Catalog Co., New York (1927).

28. Ytrehus, T., "Theory and Experiments on Gas Kinetics in Evaporation", (Rarefied Gas Dynamics) Progress in Astronautics and Aeronautics, 51, II, 1197-1212 (1976).

APPENDIX A

Kinetic Theory Definitions

In the following, the integrals are over all of velocity space, the particles are of identical mass m, and cartesian tensor notation is used.

1. The density is given directly from the definition of the velocity distribution function $f(\underset{\sim}{r}, \underset{\sim}{\xi}, t)$ as

$$\rho(\underset{\sim}{r}, t) = m \int f d\underset{\sim}{\xi} \quad .$$

2. Mean velocity:

$$\underset{\sim}{u}(\underset{\sim}{r}, t) = \frac{m \int \underset{\sim}{\xi} f d\underset{\sim}{\xi}}{\rho(\underset{\sim}{r}, t)} \quad .$$

3. The particle velocity relative to the mean velocity, or intrinsic velocity:

$$\underset{\sim}{c} = \underset{\sim}{\xi} - \underset{\sim}{u} \quad .$$

4. The stress tensor is defined in terms of local momentum exchange:

$$P_{ij} = -m \int c_i c_j f d\underset{\sim}{\xi} \quad .$$

5. Pressure:

$$p(\underset{\sim}{r}, t) = -\frac{1}{3} P_{ii} = m \int \frac{1}{3} \underset{\sim}{c}^2 f d\underset{\sim}{\xi} \quad .$$

6. Temperature is defined in terms of local kinetic energies:

$$T(\underset{\sim}{r}, t) = \frac{m \int \frac{1}{2} \underset{\sim}{c}^2 f d\underset{\sim}{\xi}}{\frac{3}{2} R \rho(\underset{\sim}{r}, t)} \quad ,$$

where R is the gas constant.

7. Heat flux vector:

$$\underset{\sim}{q}(\underset{\sim}{r}, t) = m \int \underset{\sim}{c} \frac{c^2}{2} f d\underset{\sim}{\xi} \quad .$$

8. With the above definitions, the perfect gas law holds:

$$p = \rho R T \quad .$$

APPENDIX B

Common Integrals in Kinetic Theory

Maxwellians

Integrals of the following general form occur:

$$I_n(a) = \int_0^\infty x^n e^{-ax^2} dx \quad , \qquad a > 0 \quad ,$$

$$I_o = \int_0^\infty e^{-ax^2} dx = \frac{1}{2}\left(\frac{\pi}{a}\right)^{1/2} \quad ,$$

$$I_1 = \int_0^\infty x e^{-ax^2} dx = \frac{1}{2a} \quad .$$

Further integrals can be obtained by differentiating with respect to 'a' under the integral:

$$I_2 = -\frac{dI_o}{da} = \frac{1}{4a}\left(\frac{\pi}{a}\right)^{1/2} \quad ,$$

$$I_3 = -\frac{dI_1}{da} = \frac{1}{2a^2} \quad ,$$

etc.

Maxwellians translating with a mean velocity u

With the change of variable, $\eta = \xi - u$,

$$\int_0^\infty e^{\frac{-(\xi-u)^2}{2RT}} d\xi = \int_{-u}^\infty e^{\frac{-\eta^2}{2RT}} d\eta \quad .$$

Integrals of the following general form occur:

$$J_m(\beta) = \int_{-u}^{\infty} \eta^m e^{\frac{-\eta^2}{\beta}} d\eta \quad ,$$

$$J_o = \int_{-u}^{\infty} e^{\frac{-\eta^2}{\beta}} d\eta = \frac{\sqrt{\pi\beta}}{2}[1 + \operatorname{erf}(\frac{u}{\sqrt{\beta}})] \quad ,$$

$$J_1 = \int_{-u}^{\infty} \eta e^{\frac{-\eta^2}{\beta}} d\eta = \frac{\beta}{2} e^{\frac{-u^2}{\beta}} \quad .$$

Further integrals can be obtained in a similar manner as above.

Note the recurrence of the two groups

$$E = 1 + \operatorname{erf}(\frac{u}{\sqrt{\beta}}) \quad ,$$

$$X = e^{\frac{-u^2}{\beta}} \quad .$$

APPENDIX C

The Six Moment Equations for Steady Plane One-Dimensional Flow and the Physical Variables

The distribution function assumed is given by (3.4). The following definitions are convenient due to the recurrence of certain functional forms (see Appendix B).

$$\beta_1 = 2RT_1 \quad , \qquad \beta_2 = 2RT_2 \quad ,$$

$$E_1 = 1 + \operatorname{erf}\left(\frac{u_1}{\sqrt{\beta_1}}\right) \quad , \qquad E_2 = 1 - \operatorname{erf}\left(\frac{u_2}{\sqrt{\beta_2}}\right) \quad ,$$

$$X_1 = e^{\frac{-u_1^2}{\beta_1}} \quad , \qquad X_2 = e^{\frac{-u_2^2}{\beta_2}} \quad .$$

For the steady plane one-dimensional case of Figure 1(b), the Maxwell integral equations of transfer take the form

$$\frac{d}{dx} \int f \xi_x Q d\underset{\sim}{\xi} = \Delta Q \quad .$$

The conservation equations with $\Delta Q = 0$ are as follows:

<u>$Q = m$</u> (Mass conservation)

$$\frac{d}{dx}\left[n_1\left(u_1 E_1 + \sqrt{\frac{\beta_1}{\pi}}\, X_1\right) + n_2\left(u_2 E_2 - \sqrt{\frac{\beta_2}{\pi}}\, X_2\right)\right] = 0 \quad ,$$

<u>$Q = m\xi_x$</u> (Momentum conservation)

$$\frac{d}{dx}\left[n_1\left\{\left(\frac{\beta_1}{2} + u_1^2\right)E_1 + u_1 \sqrt{\frac{\beta_1}{\pi}}\, X_1\right\} + n_2\left\{\left(\frac{\beta_2}{2} + u_2^2\right)E_2 - u_2\sqrt{\frac{\beta_2}{\pi}}\, X_2\right\}\right] = 0 \, ,$$

$Q = \frac{1}{2} m\xi^2$ (Energy conservation)

$$\frac{d}{dx}\Big[n_1 \Big\{\big(\tfrac{5}{2} u_1\beta_1 + u_1^3\big)E_1 + (2\beta_1 + u_1^2)\sqrt{\frac{\beta_1}{\pi}} \quad X_1\Big\}$$

$$+ \; n_2 \Big\{\big(\tfrac{5}{2} u_2\beta_2 + u_2^3\big)E_2 - (2\beta_2 + u_2^2)\sqrt{\frac{\beta_2}{\pi}}\, X_2\Big\}\Big] \; = \; 0 \quad .$$

The conserved quantities in brackets are thus constants, and it is convenient to designate the bracketed terms as such

$$\frac{d}{dx}[2B_1] = 0 \;, \qquad B_1 = \text{mass flux} \;,$$

$$\frac{d}{dx}[2B_2] = 0 \;, \qquad B_2 = \text{momentum flux} \;,$$

$$\frac{d}{dx}[4B_3] = 0 \;, \qquad B_3 = \text{energy flux} \;.$$

These definitions simplify the form of the remaining moment equations.

$Q = \frac{1}{2} m\xi_x\xi^2$ (Heat flux equation)

$$\frac{d}{dx}\Big[n_1\big(\tfrac{5}{4}\beta_1^2 + 4u_1^2\,\beta_1 + u_1^4\big)E_1 + n_1\big(u_1^3 + \tfrac{7}{2}u_1\beta_1\big)\sqrt{\frac{\beta_1}{\pi}}\, X_1$$

$$+ \; n_2\big(\tfrac{5}{4}\beta_2^2 + 4u_2^2\beta_2 + u_2^4\big)E_2 - n_2\big(u_2^3 + \tfrac{7}{2}u_2\beta_2\big)\sqrt{\frac{\beta_2}{\pi}}\, X_2\Big]$$

$$= \frac{4}{3}\,\frac{p}{\mu}\big[u(B_2 + n_1\beta_1E_1 + n_2\beta_2E_2) - 2B_3\big] \quad ,$$

$Q = m\xi_x^2$

$$\frac{d}{dx}\Big[n_1(u_1^3 + \tfrac{3}{2}u_1\beta_1)E_1 + n_1(\beta_1 + u_1^2)\sqrt{\frac{\beta_1}{\pi}}\;X_1$$

$$+ n_2(u_2^3 + \tfrac{3}{2}u_2\beta_2)E_2 - n_2(\beta_2 + u_2^2)\sqrt{\frac{\beta_2}{\pi}}\;X_2\Big]$$

$$= \frac{2}{3}\frac{p}{\mu}\left[2nu^2 - 2B_2 + \tfrac{1}{2}(n_1\beta_1E_1 + n_2\beta_2E_2)\right] \quad ,$$

$Q = m\xi_x^3$

$$\frac{d}{dx}\Big[n_1(\tfrac{3}{4}\beta_1^2 + 3\beta_1u_1^2 + u_1^4)E_1 + n_1(u_1^3 + \tfrac{5}{2}u_1\beta_1)\sqrt{\frac{\beta_1}{\pi}}\;X_1$$

$$+ n_2(\tfrac{3}{4}\beta_2^2 + 3\beta_2u_2^2 + u_2^4)E_2 - n_2(u_2^3 + \tfrac{5}{2}u_2\beta_2)\sqrt{\frac{\beta_2}{\pi}}\;X_2\Big]$$

$$= 2\,\frac{p}{\mu}\,\Big\{u[B_2 + \tfrac{1}{4}(n_1\beta_1E_1 + n_2\beta_2E_2)] - 2B_3$$

$$+ \tfrac{3}{4}n_1\beta_1(u_1E_1 + \sqrt{\frac{\beta_1}{\pi}}\;X_1) + \tfrac{3}{4}n_2\beta_2(u_2E_2 - \sqrt{\frac{\beta_2}{\pi}}\;X_2)\Big\} \quad .$$

The physical variables follow from the definitions in Appendix A.

Density

$$n = \tfrac{1}{2}n_1E_1 + \tfrac{1}{2}n_2E_2 \quad ,$$

Mean velocity

$$u = B_1/n \quad ,$$

Normal stresses

$$P_{xx} = -\frac{1}{2} mn_1 \{[\frac{\beta_1}{2} + u_1^2] E_1 + u_1 \sqrt{\frac{\beta_1}{\pi}} X_1\}$$

$$- \frac{1}{2} mn_2 \{[\frac{\beta_2}{2} + u_2^2] E_2 - u_2 \sqrt{\frac{\beta_2}{\pi}} X_2\} + mnu^2 \quad ,$$

$$P_{yy} = P_{zz} = -\frac{1}{4} mn_1 \beta_1 E_1 - \frac{1}{4} mn_2 \beta_2 E_2 \quad ,$$

Pressure

$$p = \frac{1}{6} mn_1 [(u_1^2 + \frac{3}{2}\beta_1) E_1 + u_1 \sqrt{\frac{\beta_1}{\pi}} X_1]$$

$$+ \frac{1}{6} mn_2 [(u_2^2 + \frac{3}{2}\beta_2) E_2 - u_2 \sqrt{\frac{\beta_2}{\pi}} X_2] - \frac{1}{3} mnu^2 \quad ,$$

Temperature

$$T = \frac{p}{mnR} \quad ,$$

Heat flux

$$\dot{q}_x = \frac{1}{4} mn_1 \{ - [\frac{5}{2}(u - u_1)\beta_1 + (u - u_1)^3] E_1 + [2\beta_1 + u_1^2 + 3(u^2 - uu_1)] \sqrt{\frac{\beta_1}{\pi}} X_1\}$$

$$- \frac{1}{4} mn_2 \{[\frac{5}{2}(u - u_2)\beta_2 + (u - u_2)^3] E_2 + [2\beta_2 + u_2^2 + 3(u^2 - uu_2)] \sqrt{\frac{\beta_2}{\pi}} X_2\}.$$

APPENDIX D

Matrix Form of the Moment Equations Used in the Numerical Solution

The same notation is used as in Appendix C.

The matrix form of the moment equations is

$$A_{ij} \frac{d}{dx} (y_j) = G_i \quad ,$$

where

$$y_1 = n_1 \; , \qquad y_4 = n_2 \; ,$$

$$y_2 = u_1 \; , \qquad y_5 = u_2 \; ,$$

$$y_3 = \beta_1 \; , \qquad y_6 = \beta_2 \; .$$

The elements of $\underset{\sim}{A}$ and $\underset{\sim}{G}$ are given below for each moment equation used. The equations have been nondimensionalized with reference values n_o, T_o as follows:

$$\bar{n}_i = n_i / n_o \; ,$$

$$\bar{u}_i = u_i / \sqrt{RT_o} \; , \qquad (i = 1, 2)$$

$$\bar{\beta}_i = \beta_i / \; RT_o \; ,$$

$$\bar{x} = x / \lambda \; .$$

The overbars have been dropped for convenience in the following.

$\underline{Q = m}$

$$A_{11} = u_1E_1 + \sqrt{\frac{\beta_1}{\pi}}\,X_1 \,, \qquad A_{14} = u_2E_2 - \sqrt{\frac{\beta_2}{\pi}}\,X_2 \,,$$

$$A_{12} = n_1E_1 \,, \qquad A_{15} = n_2E_2 \,,$$

$$A_{13} = \frac{1}{2}\,\frac{n_1}{\sqrt{\pi\beta_1}}\,X_1 \,, \qquad A_{16} = -\frac{1}{2}\,\frac{n_2}{\sqrt{\pi\beta_2}}\,X_2 \,,$$

$$G_1 = 0 \,.$$

$\underline{Q = m\xi_x}$

$$A_{21} = \left(\frac{\beta_1}{2} + u_1^2\right)E_1 + u_1\sqrt{\frac{\beta_1}{\pi}}\,X_1 \,, \qquad A_{24} = \left(\frac{\beta_2}{2} + u_2^2\right)E_2 - u_2\sqrt{\frac{\beta_2}{\pi}}\,X_2 \,,$$

$$A_{22} = 2n_1\left(u_1E_1 + \sqrt{\frac{\beta_1}{\pi}}\,X_1\right) \,, \qquad A_{25} = 2n_2\left(u_2E_2 - \sqrt{\frac{\beta_2}{\pi}}\,X_2\right) \,,$$

$$A_{23} = \frac{1}{2}\,n_1\,E_1 \,, \qquad A_{26} = \frac{1}{2}\,n_2\,E_2 \,,$$

$$G_2 = 0 \,.$$

$\underline{Q = m\xi_x^2}$

$$A_{31} = u_1 E_1 (u_1^2 + \tfrac{3}{2}\beta_1) + \sqrt{\frac{\beta_1}{\pi}}\, X_1(\beta_1 + u_1^2) \quad ,$$

$$A_{32} = 3n_1 (u_1^2 E_1 + \tfrac{1}{2}\beta_1 E_1 + u_1 \sqrt{\frac{\beta_1}{\pi}}\, X_1) \quad ,$$

$$A_{33} = \tfrac{3}{2} n_1 (u_1 E_1 + \sqrt{\frac{\beta_1}{\pi}}\, X_1) \quad ,$$

$$A_{34} = u_2 E_2 (u_2^2 + \tfrac{3}{2}\beta_2) - \sqrt{\frac{\beta_2}{\pi}}\, X_2(\beta_2 + u_2^2) \quad ,$$

$$A_{35} = 3n_2 (u_2^2 E_2 + \tfrac{1}{2}\beta_2 E_2 - u_2 \sqrt{\frac{\beta_2}{\pi}}\, X_2) \quad ,$$

$$A_{36} = \tfrac{3}{2} n_2 (u_2 E_2 - \sqrt{\frac{\beta_2}{\pi}}\, X_2) \quad ,$$

$$G_3 = \frac{\sqrt{2\pi}}{3}\, n(2nu^2 - 2B_2 + \tfrac{1}{2}\, n_1\beta_1 E_1 + \tfrac{1}{2}\, n_2\beta_2 E_2) \quad .$$

$\underline{Q = m\xi_y^2}$

$$A_{41} = \beta_1 (u_1 E_1 + \sqrt{\frac{\beta_1}{\pi}}\, X_1) \quad ,$$

$$A_{42} = n_1 \beta_1 E_1 \quad ,$$

$$A_{43} = n_1 (u_1 E_1 + \tfrac{3}{2} \sqrt{\frac{\beta_1}{\pi}}\, X_1) \quad ,$$

$$A_{44} = \beta_2 (u_2 E_2 - \sqrt{\frac{\beta_2}{\pi}}\, X_2) \quad ,$$

$$A_{45} = n_2 \beta_2 E_2 \quad ,$$

$$A_{46} = n_2 (u_2 E_2 - \tfrac{3}{2} \sqrt{\frac{\beta_2}{\pi}}\, X_2) \, ,$$

$$G_4 = - G_3 \quad .$$

$\underline{Q = \frac{1}{2} m\xi_x \xi^2}$

$$A_{51} = (\tfrac{5}{4}\beta_1^2 + 4u_1^2\,\beta_1 + u_1^4)E_1 + (u_1^3 + \tfrac{7}{2}u_1\beta_1)\sqrt{\frac{\beta_1}{\pi}}\;X_1 \quad ,$$

$$A_{52} = n_1[4(2u_1\beta_1 + u_1^3)E_1 + (6\beta_1 + 4u_1^2)\sqrt{\frac{\beta_1}{\pi}}\;X_1] \quad ,$$

$$A_{53} = n_1[(\tfrac{5}{2}\beta_1 + 4u_1^2)E_1 + 4u_1\sqrt{\frac{\beta_1}{\pi}}\;X_1] \quad ,$$

$$A_{54} = (\tfrac{5}{4}\beta_2^2 + 4u_2^2\,\beta_2 + u_2^4)E_2 - (u_2^3 + \tfrac{7}{2}u_2\beta_2)\sqrt{\frac{\beta_2}{\pi}}\;X_2 \quad ,$$

$$A_{55} = n_2[4(2u_2\beta_2 + u_2^3)E_2 - (6\beta_2 + 4u_2^2)\sqrt{\frac{\beta_2}{\pi}}\;X_2] \quad ,$$

$$A_{56} = n_2[(\tfrac{5}{2}\beta_2 + 4u_2^2)E_2 - 4u_2\sqrt{\frac{\beta_2}{\pi}}\;X_2] \quad ,$$

$$G_5 = \frac{-\sqrt{8\pi}}{3}\,n[2B_3 - u(B_2 + n_1\beta_1E_1 + n_2\beta_2E_2)] \quad .$$

$\underline{Q = m\xi_x^3}$

$$A_{61} = (\tfrac{3}{4}\beta_1^2 + 3u_1^2\,\beta_1 + u_1^4)E_1 + (u_1^3 + \tfrac{5}{2}u_1\beta_1)\sqrt{\frac{\beta_1}{\pi}}\;X_1 \quad ,$$

$$A_{62} = n_1[(4u_1^2 + 6\beta_1)u_1E_1 + 4(u_1^2 + \beta_1)\sqrt{\frac{\beta_1}{\pi}}\;X_1] \quad ,$$

$$A_{63} = 3n_1[(\frac{\beta_1}{2} + u_1^2)E_1 + u_1\sqrt{\frac{\beta_1}{\pi}}\;X_1] \quad ,$$

$$A_{64} = (\tfrac{3}{4}\beta_2^2 + 3u_2^2\,\beta_2 + u_2^4)E_2 - (u_2^3 + \tfrac{5}{2}u_2\beta_2)\sqrt{\frac{\beta_2}{\pi}}\;X_2 \quad ,$$

$$A_{65} = n_2[(4u_2^2 + 6\beta_2)u_2E_2 - 4(u_2^2 + \beta_2)\sqrt{\frac{\beta_2}{\pi}}\;X_2] \quad ,$$

$$A_{66} = 3n_2[(\frac{\beta_2}{2} + u_1^2)E_2 - u_2\sqrt{\frac{\beta_2}{\pi}}\;X_2] \quad ,$$

$$G_6 = -\sqrt{2\pi}\,n[2B_3 - u(B_2 + \tfrac{1}{4}n_1\beta_1E_1 + \tfrac{1}{4}n_2\beta_2E_2)$$
$$- \tfrac{3}{4}n_1\beta_1(u_1E_1 + \sqrt{\frac{\beta_1}{\pi}}\;X_1) - \tfrac{3}{4}n_2\beta_2(u_2E_2 - \sqrt{\frac{\beta_2}{\pi}}\;X_2)].$$

TABLE I

Substance	$T(^oK)$	$L(m^2/sec^2) \times 10^{-6}$	$\beta + 1 \approx \frac{L}{RT}$
Water	273	2.50	19.8
(M=18)	300	2.436	17.6
	366.6	2.274	13.4
	373	2.26	13.1
Ethanol	273	.920	18.7
(M=46)	351.5	.855	13.5
Hydrogen	14.44	.454	7.6
(M=2)			
Oxygen	55.56	.246	17.0
(M=32)	100	.203	7.8
Sodium	400	4.49	31.1
(M=23)	1000	4.02	11.1
Argon	87.4	.35	19.3
(M=40)			
CCl_4	349.8	.194	5.3
(M=80)			

Note $R = \frac{8310}{M} \frac{m^2}{sec^2 \, ^oK}$

TABLE II

Example of convergence behavior for $\epsilon\,\Delta\theta = 0.01$, $\epsilon\,\Delta\nu = 0.12$. The initial guess for each succeeding Kn is the previous solution.

Kn	Iteration	SUMSQ
1	6	$.29 \times 10^{-6}$
	7	$.54 \times 10^{-13}$
1/2	6	$.19 \times 10^{-4}$
	7	$.16 \times 10^{-8}$
1/4	15	$.76 \times 10^{-4}$
	32	$.48 \times 10^{-4}$
	35	$.16 \times 10^{-7}$
	36	$.30 \times 10^{-11}$
1/6	12	$.70 \times 10^{-3}$
	30	$.11 \times 10^{-3}$
	33	$.10 \times 10^{-5}$
	34	$.19 \times 10^{-8}$
1/8	10	$.34 \times 10^{-2}$
	20	$.56 \times 10^{-4}$
	40	$.42 \times 10^{-4}$
	60	$.36 \times 10^{-4}$
	100	$.15 \times 10^{-4}$
	118 terminated	$.10 \times 10^{-4}$

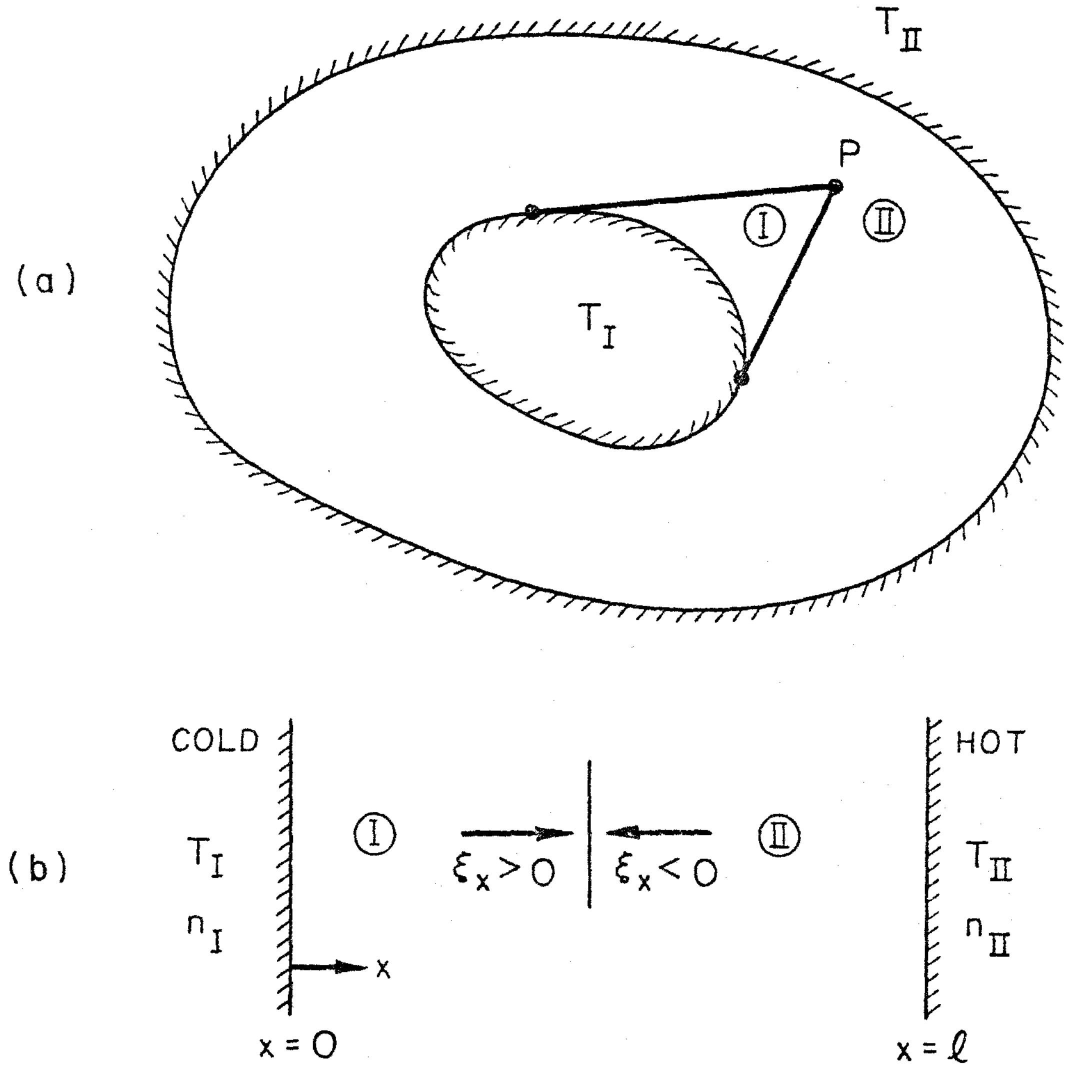

Figure 1. (a) Diagram showing regions I and II determined by the "line of sight" from an arbitrary point P.
(b) Diagram for the plane two-interface problem showing regions I and II.

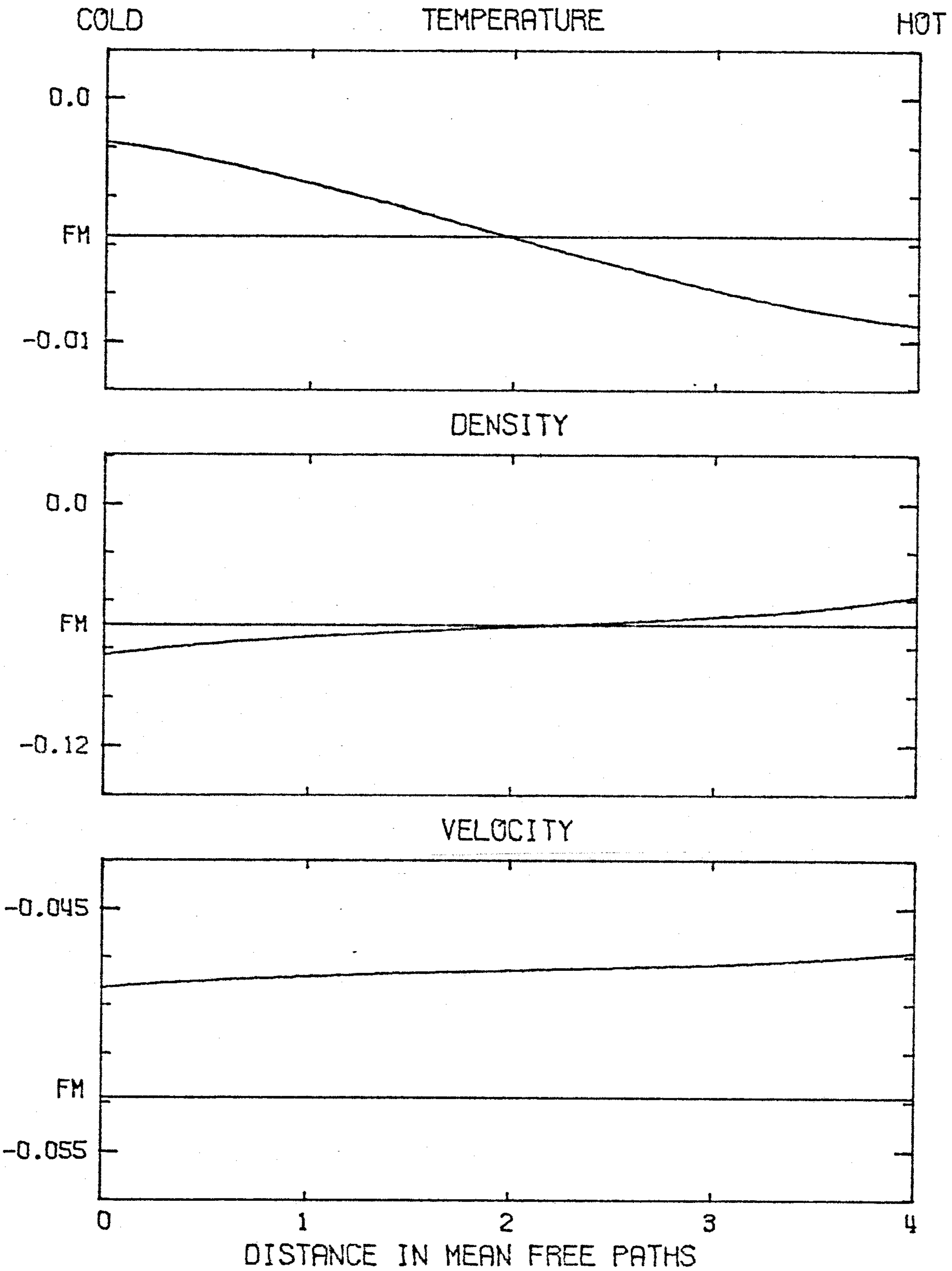

Figure 2. Results of the numerical solution of the nonlinear moment equations for Kn = 1/4 showing normalized deviations of the physical variables from the values at the hot side. Cold side: $(T_C - T_H)/T_H = -0.01$, $\beta = 12$.

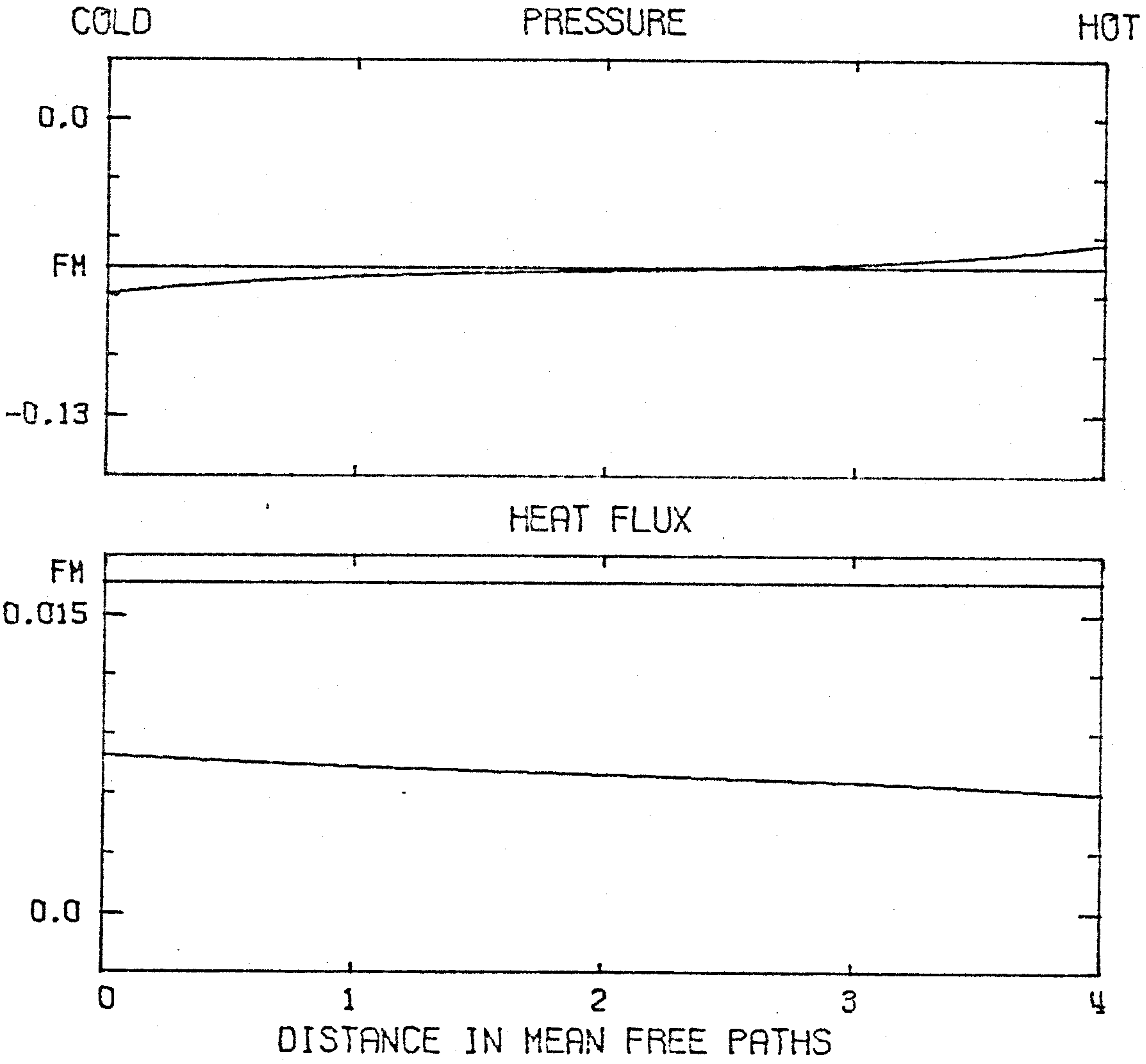

Figure 2. (Continued)

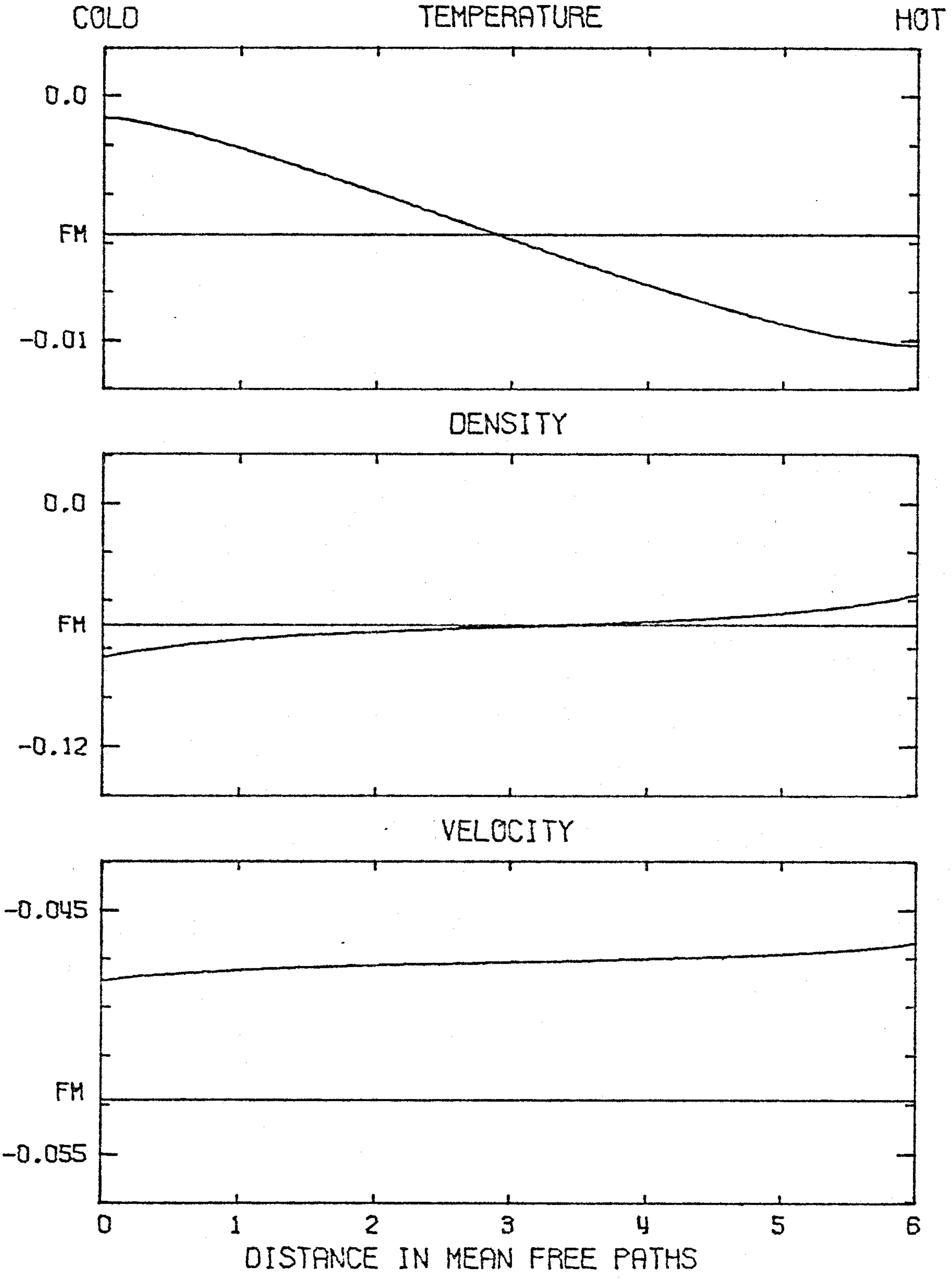

Figure 3. Results of the numerical solution of the nonlinear moment equations for Kn = 1/6 showing normalized deviations of the physical variables from the values at the hot side. Cold side: $(T_C - T_H)/T_H = -0.01$, $\beta = 12$.

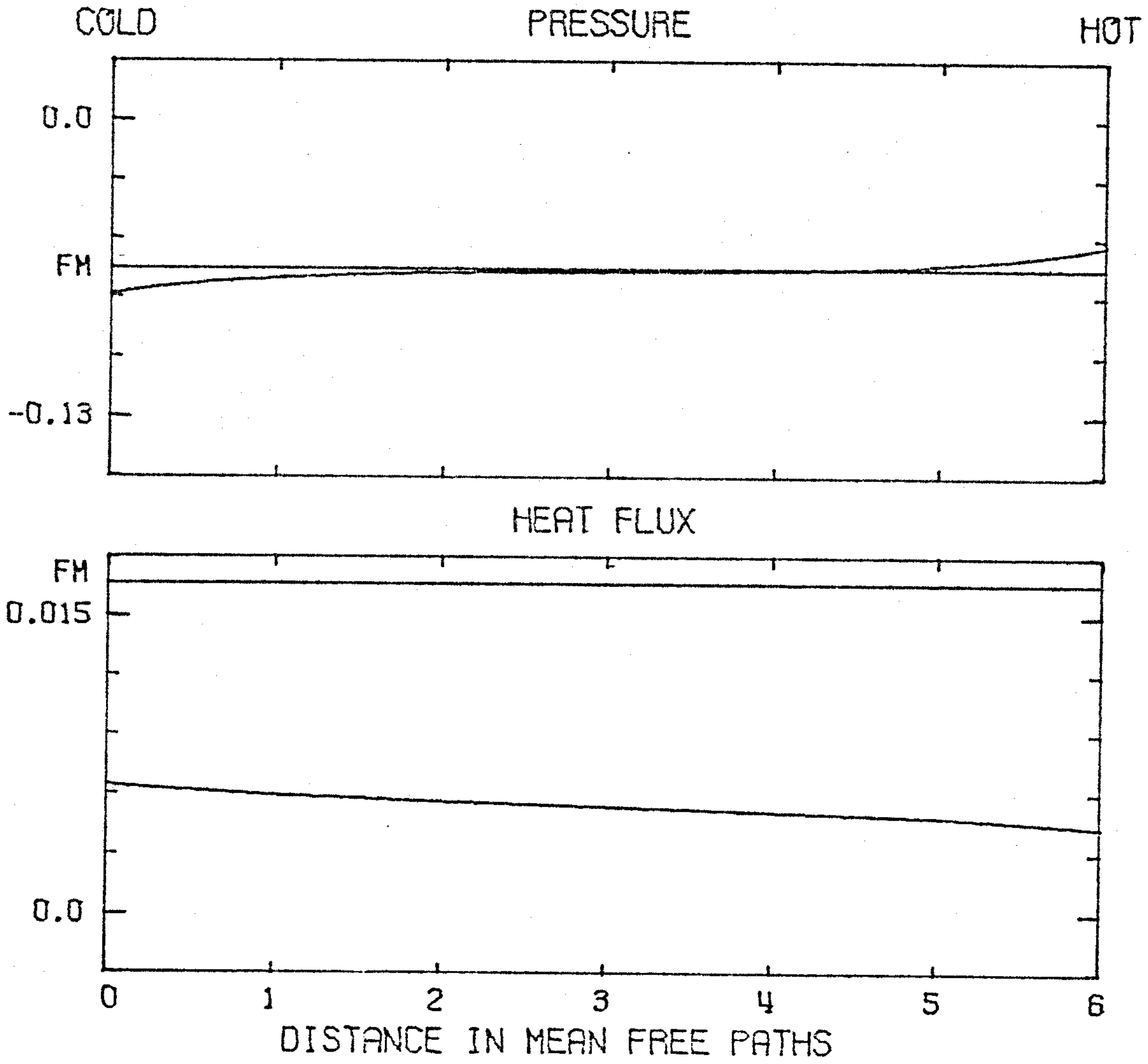

Figure 3. (Continued)